



Defence Research and
Development Canada

Recherche et développement
pour la défense Canada



A novel approach for the detection of maneuvering air targets in sea-clutter using High-Frequency Surface-Wave radar

T. Thayaparan, L.J. Stankovic and M. Dakovic

Defence R&D Canada – Ottawa

TECHNICAL REPORT

DRDC Ottawa TR 2005-251

December 2005

Canada

A novel approach for the detection of maneuvering air targets in sea-clutter using High-Frequency Surface-Wave radar

T. Thayaparan
Defence R&D Canada – Ottawa

L. J. Stanković and M. Daković
University of Montenegro

Defence R&D Canada – Ottawa

Technical Report

DRDC Ottawa TR 2005-251

December 2005

© Her Majesty the Queen as represented by the Minister of National Defence, 2005

© Sa majesté la reine, représentée par le ministre de la Défense nationale, 2005

Abstract

A novel time-frequency signal decomposition approach is evaluated for the detection of maneuvering air targets in sea-clutter using High-Frequency Surface-Wave Radar (HFSWR). This approach is based upon time-frequency analysis and its eigenvalue decomposition. Results demonstrate that the new approach provides an effective way for detecting and analyzing maneuvering air targets in heavily cluttered regions. In addition, the proposed approach successfully detects the maneuvering target in all cases of the experiment. In contrast, the traditional Fourier transform method fails to detect air targets when a certain degree of acceleration is present. This is because of the phenomenon known as Doppler smearing. It is statistically shown that the new approach produces satisfactory results even with very low signal-to-noise ratios. The results obtained are robust with respect to the algorithm parameters. The basis of the method, theoretical derivations, and comparisons with traditional procedures are outlined here-in.

Résumé

Une nouvelle approche de la décomposition des signaux temps/fréquence est évaluée en vue de la détection de cibles aériennes en manŒuvre dans un clutter de mer au moyen d'un radar haute fréquence à ondes de surface (HFSWR). Cette approche est fondée sur l'analyse temps/fréquence et la décomposition de sa valeur propre. Les résultats montrent que la nouvelle approche fournit un moyen efficace de détecter et d'analyser les cibles aériennes en manŒuvre dans des zones présentant un clutter élevé. En outre, l'approche proposée permet de détecter la cible en manŒuvre dans tous les cas de l'expérience. Par contre, la méthode classique des transformations de Fourier ne permet pas de détecter les cibles aériennes lorsqu'un certain degré d'accélération est présent. Cela s'explique par le phénomène qu'on appelle traînage Doppler. On montre statistiquement que la nouvelle approche donne des résultats satisfaisants, même en présence de rapports signal/bruit très faibles. Les résultats obtenus sont solides en ce qui concerne les paramètres des algorithmes. Le fondement de la méthode, les dérivations théoriques et les comparaisons avec les procédures classiques sont décrits aux présentes.

Executive summary

A High-Frequency Surface-Wave Radar (HFSWR) is an effective and relatively low-cost means of providing over-the-horizon surveillance of surface vessels and low-flying aircraft in coastal regions. These radar systems have demonstrated the ability to detect and track surface vessels beyond 400 km range and small low-flying aircraft out to 120 km range. Thus, these systems can be used to monitor activity within the full range of the Exclusive Economic Zone (EEZ). The technology offers highly autonomous 24-hour-per-day, 7-day-per-week operation with one of the lowest operating cost per unit area of all radar types.

The Canadian Department of National Defence (DND) has engaged in research and development of HFSWR technology more than twenty years. One of the objectives of this program is to demonstrate the potential of employing HFSWR technology as a means of providing wide-area coastal surveillance of surface vessels and low-flying air targets in mid-latitude and arctic regions. An operational HFSWR must be able to operate in a congested signal spectrum using limited signal bandwidth, and in the presence of sea clutter, ionospheric interference and man-made noise. Before an operational HFSWR system can be implemented, it must demonstrate the capability in a wide range of signal and physical environments.

One of the dominant sources of clutter that degrades the detection capability of surface and low-flying targets using HFSWR is sea-clutter. Conventionally, targets are detected by the Fourier transform or Doppler processing method. However, the performance of the Fourier method degrades if the target has high acceleration. For an accelerating target the Doppler spectrum smears. The degree of smearing becomes higher with increasing coherent processing interval (CPI) for a given acceleration or when the acceleration is increased for given number of pulses. If the smearing is too much, then the Fourier method will fail to detect the target.

This report introduces a new approach for the detection of maneuvering air targets in sea-clutter using the time-frequency analysis and its eigenvalue decomposition. Results demonstrate that the new approach provides an effective way for detecting and analyzing accelerating and decelerating air targets in heavily cluttered regions. In addition, the proposed approach successfully detects the maneuvering target in all cases of the presented experiment. In contrast, the traditional Fourier transform method fails to detect air targets whenever the acceleration is increased for a given number of pulses. This is because of the phenomenon known as Doppler smearing. It is statistically shown that the new approach produces satisfactory results even with very low signal-to-noise ratios. The results obtained are robust with respect to the algorithm parameters. The basis of the method and comparisons with traditional procedures are outlined here-in. The method presented here is not restricted to this particular application, but it can also be applied in various other settings of

nonstationary signal analysis and filtering.

Although this new approach demonstrates the improved detection performance of an accelerated air target using HFSWR in sea-clutter environment, a more detailed analysis will be performed in a future study in relation to other clutter environments such as ionosphere, meteors, and lighting environments. Furthermore, the s-method based detectors will be developed for real-time operational scenarios and will then be compared with existing Fourier Transform based detectors. Once the new approach outperforms the currently available detector methods, numerically efficient algorithms will be developed for real-time operations.

T. Thayaparan, L. J. Stanković and M. Daković ; 2005; A novel approach for the detection of maneuvering air targets in sea-clutter using High-Frequency Surface-Wave radar; DRDC Ottawa TR 2005-251; Defence R&D Canada – Ottawa.

Sommaire

Le radar haute fréquence à ondes de surface (HFSWR) est un moyen efficace et relativement peu coûteux d'assurer une surveillance au-delà de l'horizon de navires de surface et d'avions volant à basse altitude dans les régions côtières. Ces systèmes de radar ont démontré la capacité de détection et de poursuite de navires de surface au-delà de 400 km et d'avions volant à basse altitude jusqu'à environ 120 km. Ces systèmes peuvent donc servir à la surveillance d'activité dans la zone économique exclusive (ZEE) au complet. La technologie offre un fonctionnement hautement autonome 24 heures sur 24, 7 jours sur 7, les frais de fonctionnement par unité de surface étant parmi les plus faibles pour tous les types de radar.

Le ministère de la Défense nationale (MDN) du Canada est engagé dans des travaux de recherche et développement sur la technique HFSWR depuis quinze ans. L'un des objectifs de ce programme est de démontrer la possibilité d'employer la technique du radar HFSWR comme moyen d'assurer une surveillance côtière étendue des navires de surface et des cibles aériennes volant à altitude moyenne et dans les régions arctiques. Un radar HFSWR opérationnel doit pouvoir fonctionner à des fréquences encombrées en utilisant une largeur de bande limitée de signal et en présence de clutter de mer, de brouillage ionosphérique et de bruit d'origine artificielle. Avant qu'un système de radar HFSWR opérationnel puisse être mis en place, il doit démontrer sa capacité dans toute une gamme de milieux de signalisation et de fonctionnement.

L'une des sources dominantes de clutter qui dégrade la capacité de détection, au moyen d'un radar HFSWR, des cibles de surface et des cibles volant à basse altitude est le clutter de mer. Normalement, les cibles sont détectées par la méthode des transformations de Fourier ou de traitement Doppler. Le rendement de la méthode des transformations de Fourier a cependant un effet de dégradation si la cible a une forte accélération. Pour une cible en accélération, les fréquences Doppler présentent une traînée. Le degré de traînage s'accroît avec l'augmentation de l'intervalle de traitement cohérent (ITC) pour une accélération donnée ou lorsque l'accélération est accrue pour un nombre donné d'impulsions. Si le traînage est trop élevé, la méthode des transformations de Fourier ne permet pas de détecter la cible.

Le présent rapport présente une nouvelle approche pour la détection des cibles aériennes en manœuvrant dans un clutter de mer au moyen de l'analyse temps/fréquence et la décomposition de sa valeur propre. Les résultats montrent que la nouvelle approche assure un moyen efficace de détecter et d'analyser des cibles aériennes en accélération et en freinage dans des régions présentant un clutter élevé. En outre, l'approche proposée permet de détecter la cible en manœuvrant dans tous les cas de l'expérience présentée. Par contraste, la méthode classique des transformations de Fourier ne permet pas de détecter les cibles aériennes dès que l'accélération est

accrue pour un nombre donné d'impulsions. Cela s'explique par le phénomène qu'on appelle traînage Doppler. On montre statistiquement que la nouvelle approche donne des résultats satisfaisants, même en présence de rapports signal/bruit très faibles. Les résultats obtenus sont solides en ce qui concerne les paramètres des algorithmes. Le fondement de la méthode et les comparaisons avec les procédures classiques sont donnés aux présentes. La méthode décrite aux présentes n'est pas limitée à cette application particulière, elle peut également être appliquée à diverses autres méthodes d'analyse et de filtrage de signaux non stationnaires.

Même si la nouvelle approche démontre un meilleur rendement en ce qui concerne la détection d'une cible aérienne en accélération au moyen d'un radar HFSWR dans un milieu présentant du clutter de mer, une analyse plus détaillée sera effectuée dans une étude ultérieure par rapport à d'autres milieux présentant du clutter, comme l'ionosphère, les météores et les milieux lumineux. En outre, les détecteurs fondés sur la s-méthode seront mis au point pour des scénarios opérationnels en temps réel, avant d'être comparés aux détecteurs fondés sur la méthode des transformations de Fourier. Une fois que la nouvelle approche offrira un meilleur rendement que les méthodes actuelles de détection, des algorithmes efficaces sur le plan numérique seront formulés pour les opérations en temps réel.

T. Thayaparan, L. J. Stanković and M. Daković ; 2005; A novel approach for the detection of maneuvering air targets in sea-clutter using High-Frequency Surface-Wave radar; DRDC Ottawa TR 2005-251; R&D pour la défense Canada – Ottawa.

This page intentionally left blank.

Table of contents

Abstract	i
Résumé	i
Executive summary	ii
Sommaire	iv
Table of contents	vii
1 Introduction	1
2 S-method: Theory	3
2.1 Short-Time Fourier Transform (STFT)	5
2.1.1 Example 1.	6
2.1.2 Example 2.	8
2.2 Wigner Distribution (WD)	10
2.2.1 Example 3.	13
2.2.2 Example 4.	14
2.3 S-Method	17
2.3.1 Example 5.	23
2.3.2 Example 6.	23
2.3.3 Example 7.	28
3 Wigner distribution based inversion and decomposition	38
4 S-method definition and basic property	40
5 Decomposition of multicomponent signals	42
5.1 Illustrative example	43

6	Decomposing radar time-varying signals in a strong sea-clutter	48
6.1	Criterion for identifying target components	48
6.2	Numerical realization	50
7	Data analysis and Results	51
7.1	Calculation procedure:	51
8	Noise Analysis in the Algorithm for Signal Decomposition	62
8.1	Noise analysis	62
9	Conclusion	67
	References	69
10	Appendix 1: High-resolution S-method with relation to the Capon's method	72
11	Appendix 2: Plots for the whole trial	74

1 Introduction

One of the dominant sources of clutter that degrades the detection capability of surface and low-flying targets using High-Frequency Surface Wave Radar (HFSWR) is sea-clutter. In a coherent HFSWR radar, the dominant form of sea-clutter is due to scattering from sea waves with wavelengths which are half of the wavelength of the radar carrier frequency and which are travelling radially towards and away from the radar [1]. This form of scattering is called Bragg scattering and it corresponds to the wave velocity $v = \sqrt{\frac{g\lambda}{4\pi}}$, where λ is the radar carrier wavelength and g is the acceleration due to gravity. Thus when the received signal of a pulse Doppler radar, taken at a particular range, is viewed in the Fourier transformed or Doppler domain, we can see two sharp peaks at frequencies $f_{Bragg} = \pm 2v/\lambda = \pm \sqrt{\frac{g}{\pi\lambda}}$. The Bragg components of the clutter are called 1st order clutter. In addition to the Bragg components, the Doppler spectrum contains a continuum called the 2nd order clutter.

Signals are commonly analyzed in either the time or frequency domain. However, some signals exhibit significant time variations of the frequency content. For these cases time-frequency representations can be used, since they combine time and frequency domain analyses to yield a more revealing picture of the temporal localization of signals spectral components [5, 14, 23, 24]. The oldest and the most widely used time-frequency representation is the short-time Fourier transform (STFT). In order to improve its concentration, various quadratic representations have been introduced [3, 6, 12]. The most prominent member of this class of representations is the Wigner distribution (WD). Inversion properties of the Wigner distribution and synthesis of a signal from a given time-frequency representation have been studied [4, 8, 9, 11, 13].

The time-frequency representation referred to as the S-method has a property that, under certain assumptions, its value for multicomponent signals is equal (or close) to the sum of the Wigner distributions of individual signal components [17]. It has been also used as a model in the implementation of time-scale representations, time-varying spectra estimation, detection and realization of higher order representations [2, 10, 15, 16, 18]. In this report, the S-method is used to introduce a new method for the decomposition of multicomponent signals by using eigenvalues and eigenvectors of an appropriately formed matrix.

The proposed decomposition method is applied in the analysis of HFSWR radar signals. Conventionally, targets are detected by the Fourier transform or Doppler processing method. However, the performance of the Fourier method degrades if the target has high acceleration. For an accelerating target the Doppler spectrum smears. The degree of smearing becomes higher when the number of pulses is

increased for a given acceleration or when the acceleration is increased for given number of pulses [25]. If the smearing is too great, then the Fourier method will fail to detect the target. The case of highly accelerating targets corresponds to the analysis of signals with fast time variations of the frequency content. Therefore, these kind of signals should be analyzed by the time-frequency representations rather than by the Fourier transform. The time-frequency based decomposition can also provide the extraction of individual signal components. This approach will be efficient in separating the target signal from an undesirable sea-clutter. This property is of a particular significance in the HFSWR signals where, besides the target signal, there is a clutter that is primarily due to scattering from the surface waves.

The results obtained by applying the time-frequency analysis based decomposition method show that one can improve the detection performance of the HFSWR, as well as add new insights into the interpretation and processing of radar signals, with respect to the traditional Fourier transform methods currently used by HFSWRs.

The paper is organized as follows. After an introduction, the theoretical development of the S-method from basic principles is given in Section 2. The inversion of the Wigner distribution is presented in Section 3. A review of the S-method definition and its basic properties is given in Section 4. This representation is used for defining a new decomposition method of multicomponent signals in Section 5. Next, the signal decomposition is discussed in Section 6 from the point of view of a target signal in a strong sea clutter. Experimental data analysis and results are presented in Section 7, proves the efficiency of the proposed method, and illustrates improvements in readability and detection of the target signal. The noise analysis in the algorithm for signal decomposition is given in Section 8. Conclusions are given in Section 9, Finally the Appendix provides a high resolution form of the S-method.

2 S-method: Theory

The Fourier Transformation (FT) of the signal $x(t)$ is defined by:

$$X(\omega) = \int_{-\infty}^{\infty} x(t)e^{-j\omega t} dt \quad (1)$$

If we have the FT of the signal $x(t)$, we can calculate the signal in time by:

$$x(t) = \frac{1}{2\pi} \int_{-\infty}^{\infty} X(\omega)e^{j\omega t} d\omega \quad (2)$$

For a signal $x(t)$ of the form:

$$x(t) = e^{-j\omega_T t} \quad (3)$$

its FT is $X(\omega) = 2\pi\delta(\omega - \omega_T)$. Both representations of the signal $x(t)$, in the time and frequency domains, are depicted in Figure 1. The reason as to why FT is not always good tool for representing signals is illustrated in Figure 2 where two different signals in time are shown in the frequency domain.

Although the phase characteristic of FT contains the information about the time instants when the spectral components occur it is very difficult to use this information. As a result we can see in Figure 2 two signals that are different in time, but have the same amplitude spectral representations. Hence, new representations have been developed whose main goal is to provide the time distribution of the spectral content. The research area that deals with these representations and their properties is the time-frequency signal analysis.

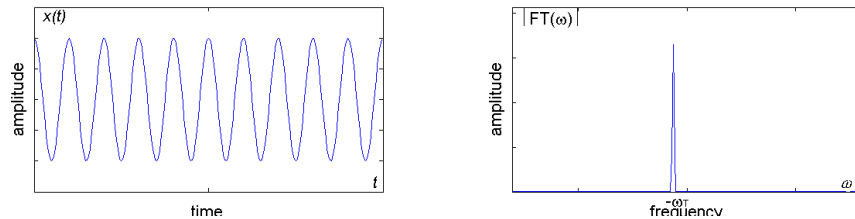


Figure 1: Representations of the signal $x(t)$ in the time and frequency domains

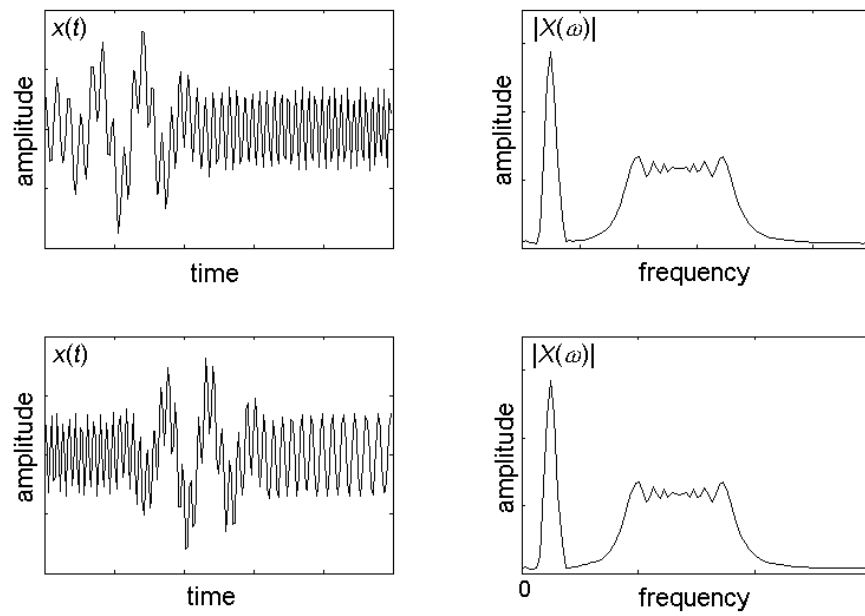


Figure 2: Representations of two different signals in the time (left hand side) frequency domains (right hand side)

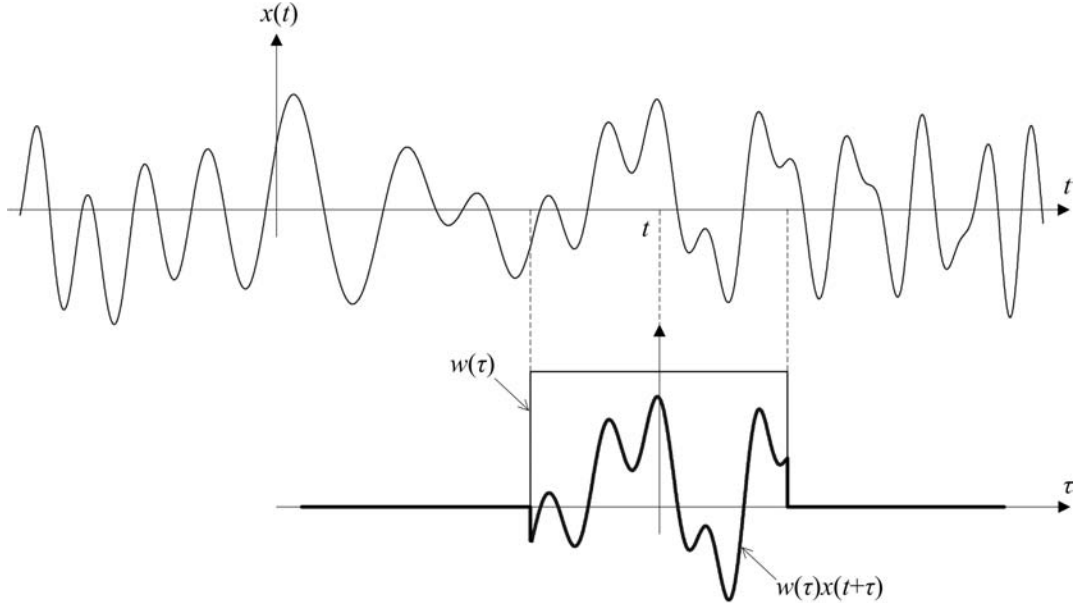


Figure 3: The illustration of the signal localization for the STFT calculation

2.1 Short-Time Fourier Transform (STFT)

The most frequently used time-frequency representation is the Short-Time Fourier Transform (STFT). The idea behind the STFT is to introduce a window function $w(t)$ that truncates the analyzed signal $x(t)$ and then calculates the FT of the truncated signal. The STFT is obtained by sliding the window along the signal. The mathematical formulation of the STFT in the analog form is:

$$STFT(t, \omega) = \int_{-\infty}^{\infty} x(t + \tau)w(\tau)e^{-j\omega\tau} d\tau \quad (4)$$

where $x(t + \tau)$ is the signal shifted in time and $w(\tau)$ is a window function. The illustration of the signal localization for the STFT calculation is given in Figure 3.

The discrete form of the STFT is given:

$$STFT(n, k) = \sum_{m=-\infty}^{\infty} w(m)x(n + m)e^{-j\frac{2\pi}{N}mk} = \sum_{m=-\infty}^{\infty} w(m)x_n(m)e^{-j\frac{2\pi}{N}mk} \quad (5)$$

An energetic version of the STFT is called *spectrogram*. It is defined by:

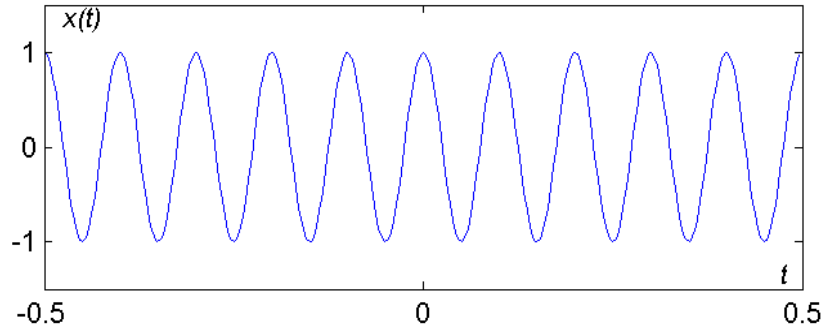


Figure 4: The representation of the signal $x(t)$ in the time domain

$$SPEC(t, \omega) = |STFT(t, \omega)|^2 \quad (6)$$

The following gives examples of the STFT for different signals with different window widths.

2.1.1 Example 1.

Consider a complex sinusoidal signal $x(t)$ with constant frequency:

$$x(t) = e^{-j20\pi t} \quad (7)$$

The representation of the signal $x(t)$ in the time domain is given in Figure 4. The STFT of this signal, at the time instant $t = 0$, for various window widths (denoted by T) is given in Figure 5.

The spectrogram is centered at the signal frequency $\omega = -20\pi = -62.8$. The spectrogram width is determined by the width of the FT of the window. Since the Hanning window is used, if we assume that the width of its FT is equal to the width of the main lobe, we get:

$$W_{window} = 4\pi/T \quad (8)$$

For wide windows, when $T \rightarrow \infty$, the spectrogram tends to a delta function at $\omega = -62.8$, as shown in Figure 5.

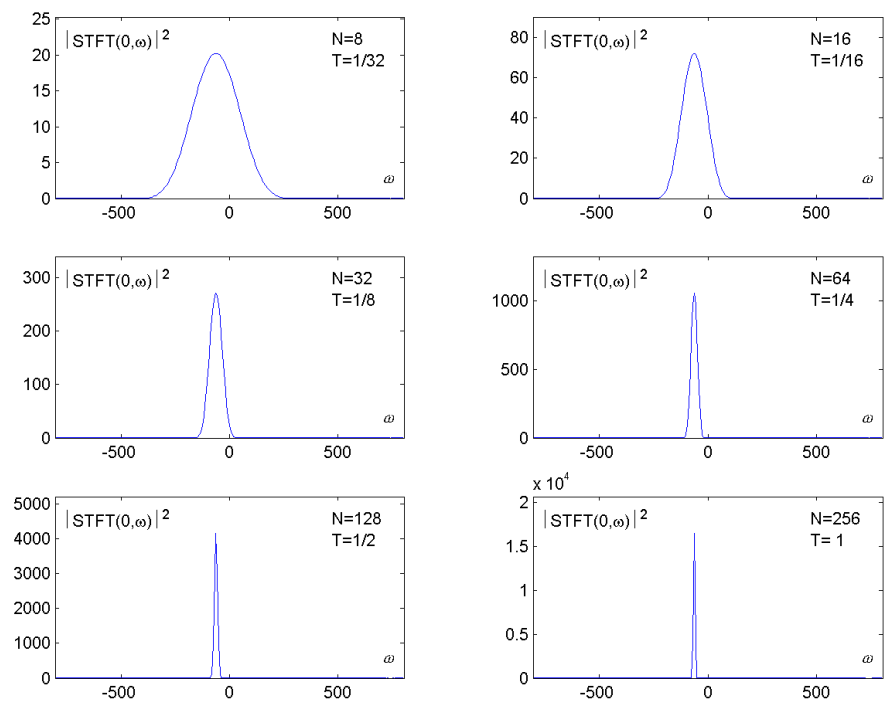


Figure 5: The spectrogram of the signal $x(t)$, at the time instant $t = 0$ and for various window widths T . Note that N is the number of samples within window.

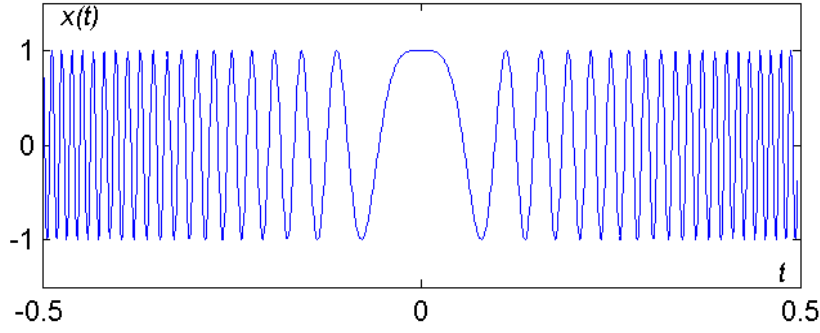


Figure 6: The representation of a LFM signal $x(t)$ in the time domain

2.1.2 Example 2.

Consider a Linear Frequency Modulated (LFM) signal $x(t)$:

$$x(t) = e^{-j160\pi t^2} \quad (9)$$

The representation of the signal $x(t)$ in the time domain is given in Figure 6. The STFT, at the time instant $t = 0$, for different window widths T , is given in Figure 7. The window function $w(t)$ used in this example and all other examples is a Hanning window function.

Unlike the previous example where the STFT is dependent only on the window width, in this example the STFT is dependent on the window width and non-stationary feature of the signal. To explain the above mentioned, we will introduce the concept of *instantaneous frequency*. The first derivative of the phase is referred to as the instantaneous frequency:

$$\omega_i(t) = \phi'(t) \quad (10)$$

The instantaneous frequency of the considered signal $x(t)$ is:

$$\omega_i(t) = -320\pi t \quad (11)$$

If t is within the range $-\frac{T}{2} \leq t \leq \frac{T}{2}$, it follows that $\omega_i(t)$ will be in the range:

$$-\frac{320\pi T}{2} \leq \omega_i(t) \leq \frac{320\pi T}{2} \quad (12)$$

The width of the STFT of the signal $x(t)$ is dependent on the width of the window and the width of the signal:

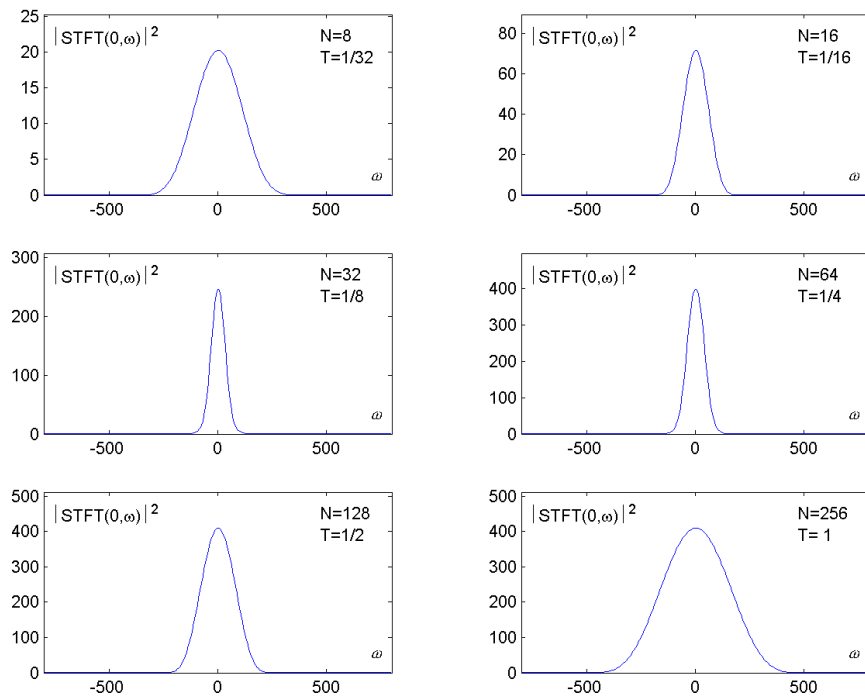


Figure 7: The spectrogram of the Linear Frequency Modulated Signal $x(t)$ in the time instant $t = 0$ and for various window widths T . N is the number of samples.

$$W_{tot} = W_{window} + W_{signal} \quad (13)$$

Since we are using the Hanning widow as a window function $w(t)$, it follows that $W_{window} = \frac{4\pi}{T}$, and from that $W_{signal} = 320\pi T$, resulting:

$$W_{tot} = \frac{4\pi}{T} + 320\pi T \quad (14)$$

It indicates that the optimal window width could be obtained from $\partial W_{tot}/\partial T = 0$ as $T_{optimal} = 1/8.94$. The spectrogram calculated using this widow width is close to the one depicted in Figure 7 with $T = 1/8$. Note that the optimal window width is highly signal dependent. When the analyzed signal is unknown, the optimal window width also unknown. This is always the case in practice.

The spectrogram width for a small T , for example $T = 1/32$, is determined by the first term $W_{window} = 4\pi/T = 128\pi = 402$ (see Figure 7). For a wide window, for example $T = 1$, the spectrogram width is determined by the second term $W_{signal} = 320\pi T = 320\pi = 1005$ (see Figure 7).

In order to show that the same conclusions hold for any considered time instant, in Figure 8 we have presented the spectrogram at the time instant $t = -0.2$. The two-dimensional spectrogram for all considered time instants $-0.5 \leq t \leq 0.5$ is shown in Figure 9.

2.2 Wigner Distribution (WD)

In order to efficiently process the linear frequency modulated signal, the Wigner Distribution (WD) is used. The mathematical formulation of the Wigner distribution in the analog form is:

$$WD(t, \omega) = \int_{-\infty}^{\infty} w\left(\frac{\tau}{2}\right)w\left(-\frac{\tau}{2}\right)x\left(t + \frac{\tau}{2}\right)x^*\left(t - \frac{\tau}{2}\right)e^{-j\omega\tau}d\tau \quad (15)$$

In the discrete domain the WD reads:

$$WD(n, k) = \sum_{m=-\infty}^{\infty} w(m)w(-m)x(n+m)x^*(n-m)e^{-j\frac{4\pi}{N}mk} \quad (16)$$

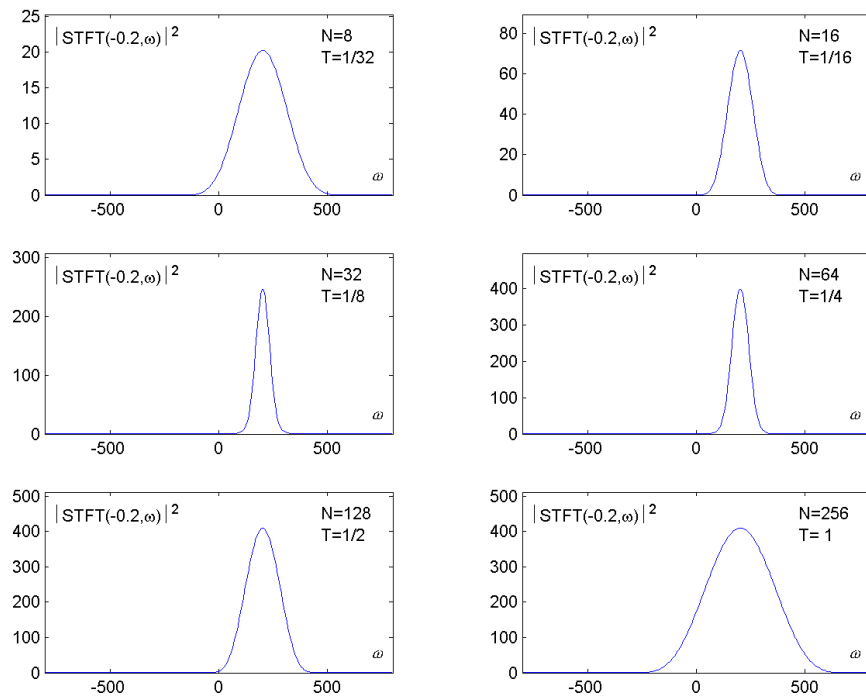


Figure 8: Spectrogram of Linear Frequency Modulated Signal $x(t)$ at time instant $t = -0.2$ and for various window widths T , N is the number of samples.

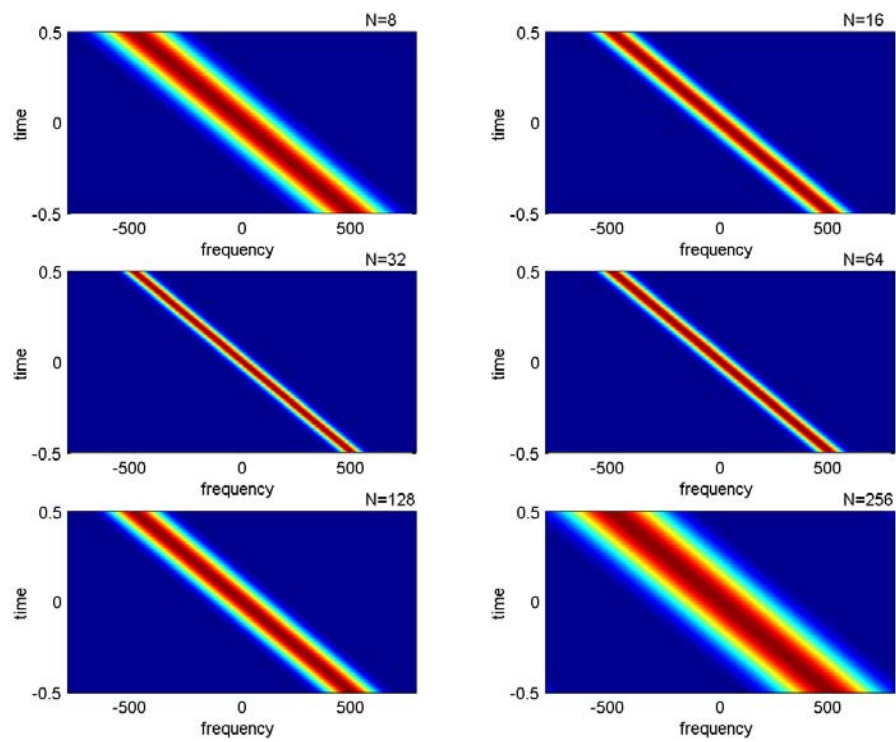


Figure 9: The spectrogram of the Linear Frequency Modulated Signal for various window widths N (number of samples)

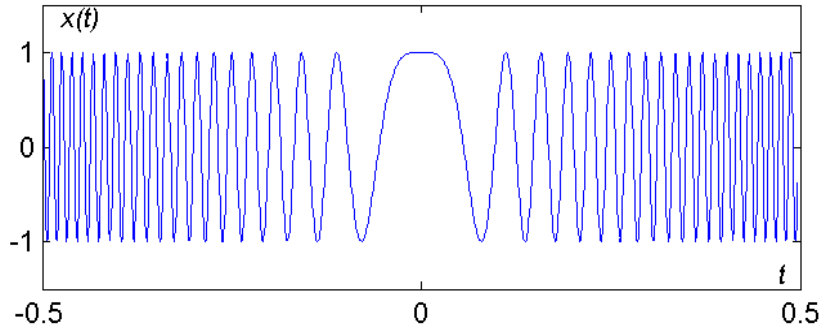


Figure 10: The representation of a LFM signal $x(t)$ in the time domain

2.2.1 Example 3.

Consider the same LFM signal $x(t)$ as the one denoted by formula (9).

$$x(t) = e^{-j160\pi t^2}$$

The representation of the signal $x(t)$ in the time domain is given in Figure 10. The Wigner distribution of this signal is calculated in the subsequent manner:

$$\begin{aligned} WD(t, \omega) &= \int_{-\infty}^{\infty} w_e(\tau) e^{-j160\pi(t+\frac{\tau}{2})^2} e^{j160\pi(t-\frac{\tau}{2})^2} e^{-j\omega\tau} d\tau = \\ &= \int_{-\infty}^{\infty} w_e(\tau) e^{-j320\pi t\tau} e^{-j\omega\tau} d\tau = \int_{-\infty}^{\infty} w_e(\tau) e^{-j(\omega+320\pi t)\tau} d\tau = \\ &= W_e(\omega + 320\pi t) \end{aligned} \quad (17)$$

where $w_e(\tau) = w(\frac{\tau}{2})w(-\frac{\tau}{2})$ and $W_e(\omega) = FT\{w_e(\tau)\}$.

Thus we can conclude that the Wigner distribution of the linear frequency modulated signal behaves in the same way as the spectrogram of a signal with constant frequency. The position of the Wigner distribution is determined by the instantaneous frequency, while its width is equal to the width of the FT of the window. It tends to a delta function for very wide windows. In order to illustrate this conclusion we presented the Wigner distribution at the instant $t = 0$ for various window widths in Figure 11. Comparing Figure 7 and Figure 11, the advantage of the Wigner distribution over the spectrogram for LFM is obvious.

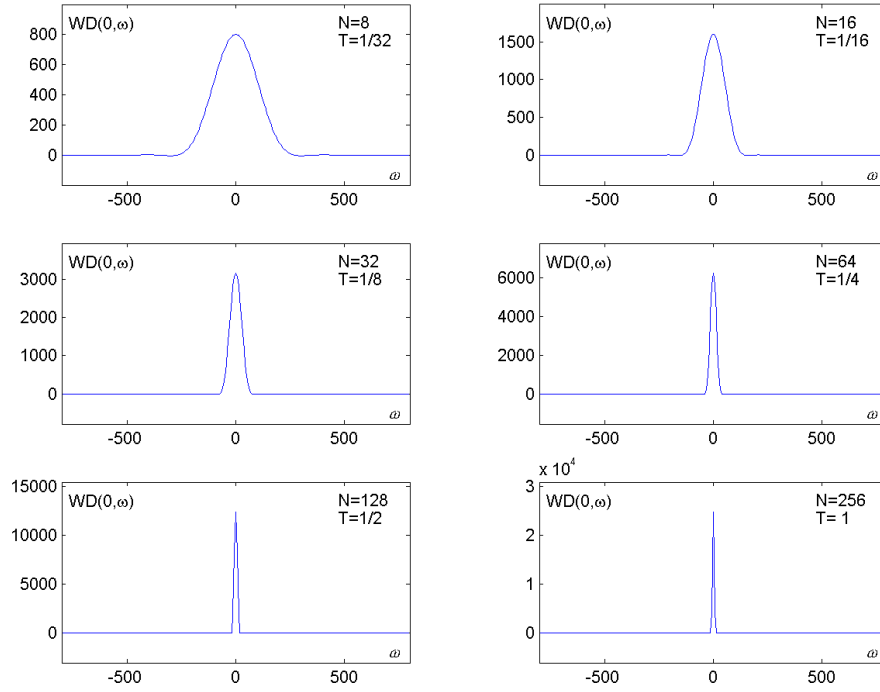


Figure 11: The Wigner Distribution of the Linear Frequency modulated Signal at the instant $t = 0$, for various window widths T and the number of samples N within the window

We have presented the same results at another instant $t = -0.2$ in Figure 12. For all instants the Wigner distribution in the time-frequency domain is presented in Figure 13.

2.2.2 Example 4.

Consider two LFM signal components $x(t)$:

$$x(t) = x_1(t) + x_2(t) = e^{-j12\pi ft^2 - j10\pi ft} + e^{-j12\pi ft^2 + j10\pi ft} \quad (18)$$

The representation of the signal $x(t)$ in the time domain is given in Figure 14.

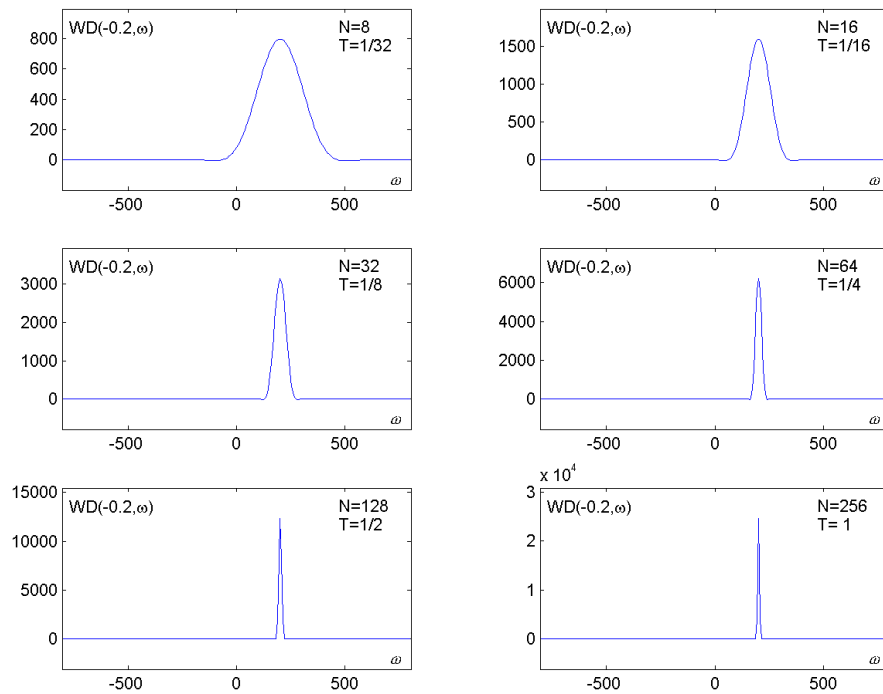


Figure 12: The Wigner Distribution of the Linear Frequency modulated Signal at the instant $t = -0.2$, for various window widths T and the number of samples N within the window

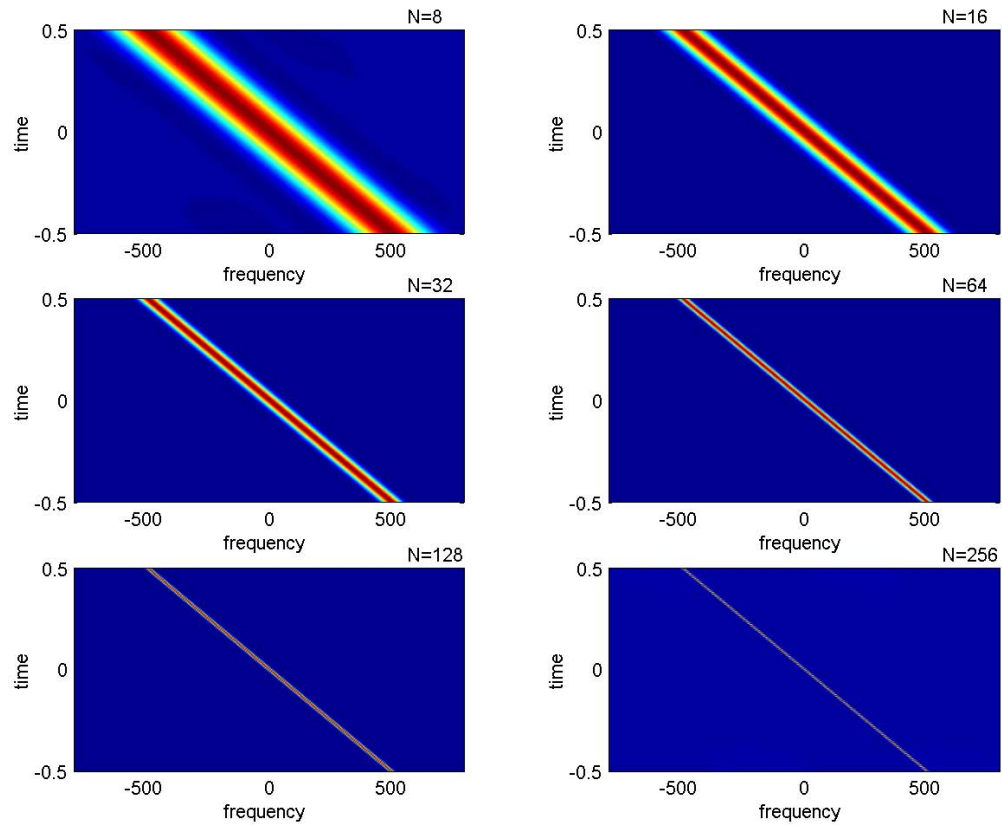


Figure 13: The Wigner Distribution of the Linear Frequency Modulated Signal for various window widths N (number of samples)

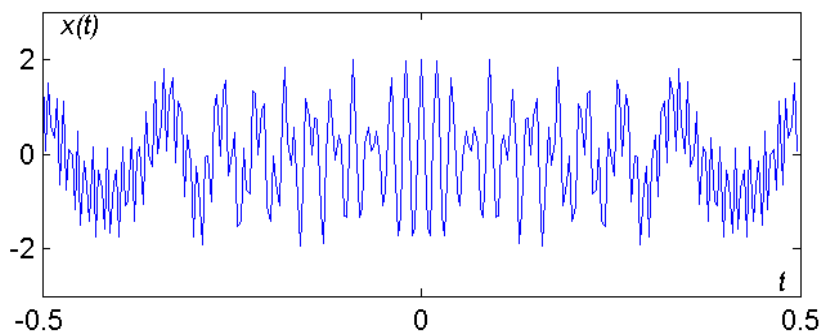


Figure 14: The representation of two LFM signal components $x(t)$ in the time domain

The Wigner distribution of this signal is calculated in the subsequent manner:

$$\begin{aligned}
WD(t, \omega) &= \int_{-\infty}^{\infty} w_e(\tau) \left[x_1(t + \frac{\tau}{2}) + x_2(t + \frac{\tau}{2}) \right] \left[x_1(t - \frac{\tau}{2}) + x_2(t - \frac{\tau}{2}) \right]^* e^{-j\omega\tau} d\tau \\
&= \int_{-\infty}^{\infty} w_e(\tau) x_1(t + \frac{\tau}{2}) x_1(t - \frac{\tau}{2})^* e^{-j\omega\tau} d\tau + \\
&\quad + \int_{-\infty}^{\infty} w_e(\tau) x_2(t + \frac{\tau}{2}) x_2(t - \frac{\tau}{2})^* e^{-j\omega\tau} d\tau + \\
&\quad + 2\text{Re}\{ \int_{-\infty}^{\infty} w_e(\tau) x_1(t + \frac{\tau}{2}) x_2(t - \frac{\tau}{2})^* e^{-j\omega\tau} d\tau \}
\end{aligned}$$

where $w_e(\tau) = w(\frac{\tau}{2})w(-\frac{\tau}{2})$ and $W_e(\omega) = FT\{w_e(\tau)\}$.

From the last formula we see that besides the Wigner distribution of auto-terms:

$$\int_{-\infty}^{\infty} w_e(\tau) x_1(t + \frac{\tau}{2}) x_1(t - \frac{\tau}{2})^* e^{-j\omega\tau} d\tau \quad \text{and} \quad \int_{-\infty}^{\infty} w_e(\tau) x_2(t + \frac{\tau}{2}) x_2(t - \frac{\tau}{2})^* e^{-j\omega\tau} d\tau,$$

there exists a cross-term: $2\text{Re}\{ \int_{-\infty}^{\infty} w_e(\tau) x_1(t + \frac{\tau}{2}) x_2(t - \frac{\tau}{2})^* e^{-j\omega\tau} d\tau \}$.

We calculated the Wigner distribution of two signal components for various window widths at the time instant $t = 0$. It is shown in Figure 15. We see that besides two auto- terms there exists a strong cross-term.

The same results, at another instant $t = 0.035$, are given in Figure 16. The value of the cross-term changes over time due to its oscillatory nature can be seen from Figures 15 and 16. For all instants the Wigner distribution in the time-frequency domain is presented in Figure 17.

2.3 S-Method

In order to eliminate the cross-terms a class of so-called reduced interference distributions is proposed. All of them are based on the Cohen definition of the quadratic time-frequency distributions, with a kernel function being a low pass two-dimensional function. These distributions are in fact forms of two-dimensional smoothed Wigner distribution. By smoothing the Wigner distribution, oscillatory cross-terms are reduced. In reduced interference distributions, two important problems arise and should be stressed:

First: By smoothing the Wigner distribution the auto-terms are also smoothed [22],

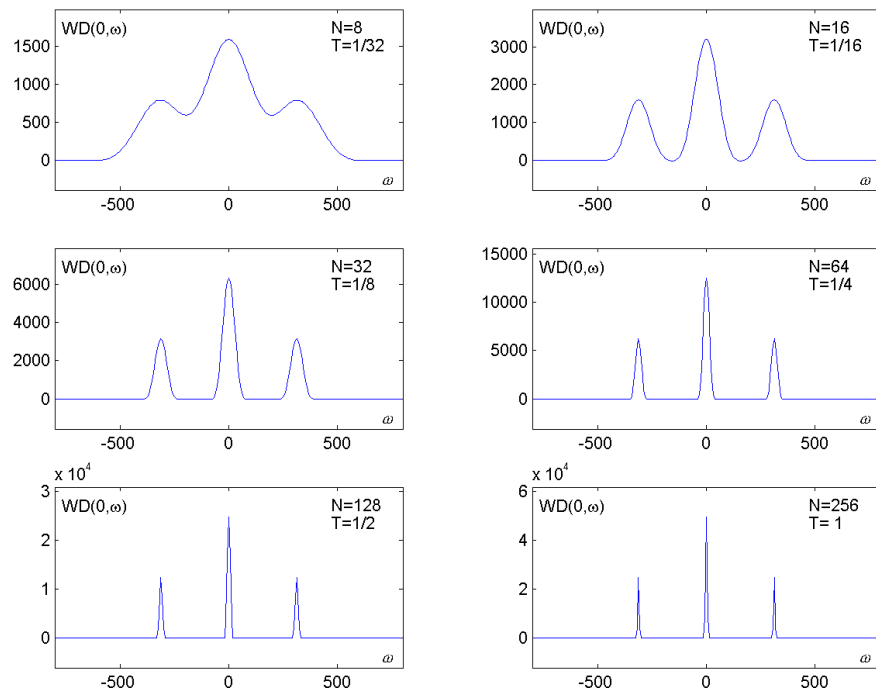


Figure 15: The Wigner Distribution of two LFM signal components $x(t)$ at the instant $t = 0$, for various window widths T and the number of samples N within the window

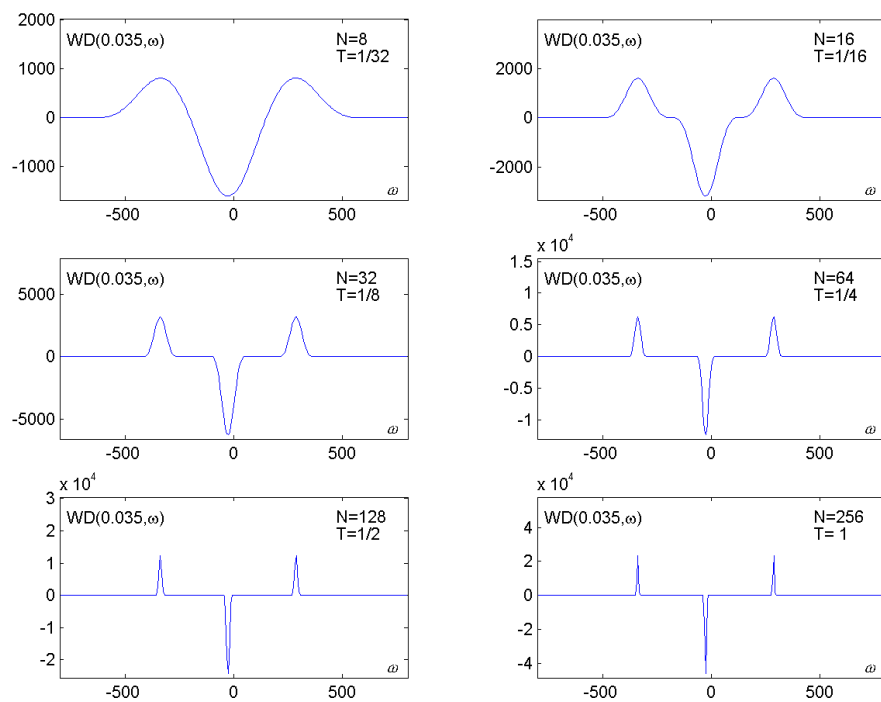


Figure 16: The Wigner Distribution of two LFM signal components $x(t)$ at the instant $t = 0.035$, for various window widths T and the number of samples N within the window

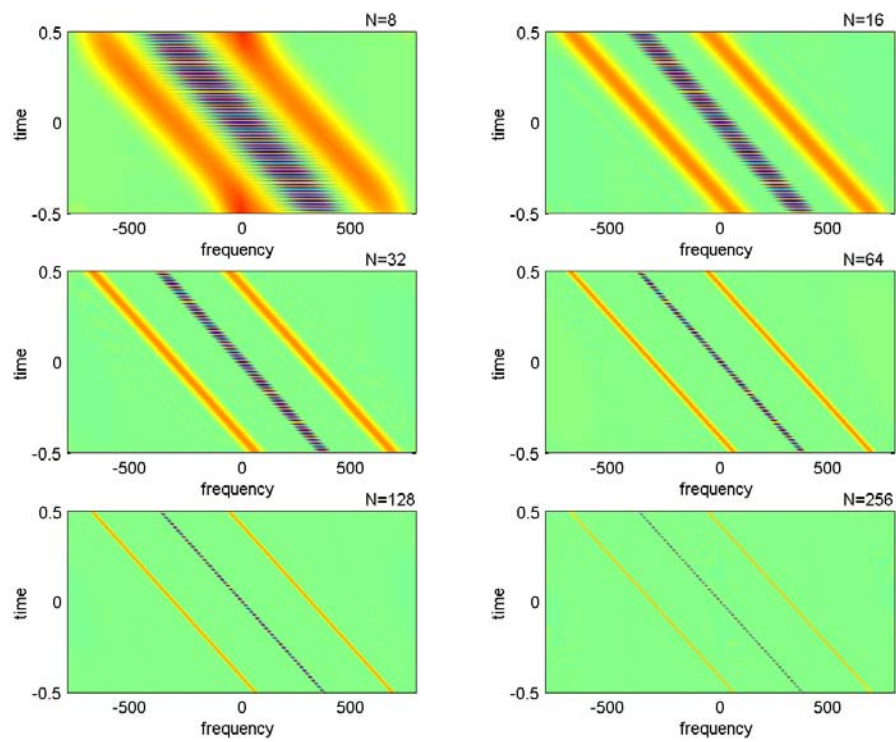


Figure 17: The Wigner Distribution of two Linear Frequency Modulated Signal components for various window widths N (number of samples)

Second: The calculation complexity is very high, including need for oversampling in most of the cases.

Here, we will present a computationally very simple method, that can produce the same auto-terms as in the Wigner distribution, but without cross-terms. It will be referred to as the S-method.

The S-method is derived from the relationship between the STFT and the Wigner distribution, which reads:

$$WD(t, \omega) = \frac{1}{\pi} \int_{-\infty}^{\infty} STFT(t, \omega + \theta) STFT^*(t, \omega - \theta) d\theta \quad (19)$$

Proof: The Wigner distribution definition reads:

$$WD(t, \omega) = \int_{-\infty}^{\infty} w\left(\frac{\tau}{2}\right) w\left(-\frac{\tau}{2}\right) x\left(t + \frac{\tau}{2}\right) x^*\left(t - \frac{\tau}{2}\right) e^{-j\omega\tau} d\tau$$

From the STFT definition

$$STFT(t, \omega) = \int_{-\infty}^{\infty} x(t + \tau) w(\tau) e^{-j\omega\tau} d\tau$$

we get

$$x(t + \tau) w(\tau) = \frac{1}{2\pi} \int_{-\infty}^{\infty} STFT(t, \theta) e^{j\theta\tau} d\theta$$

Replacing this into the Wigner distribution definition we get:

$$\begin{aligned} WD(t, \omega) &= \int_{-\infty}^{\infty} w\left(-\frac{\tau}{2}\right) x^*\left(t - \frac{\tau}{2}\right) \left[\frac{1}{2\pi} \int_{-\infty}^{\infty} STFT(t, \theta) e^{j\theta\tau/2} d\theta \right] e^{-j\omega\tau} d\tau \\ &= \frac{1}{2\pi} \int_{-\infty}^{\infty} STFT(t, \theta) \left[\int_{-\infty}^{\infty} w\left(-\frac{\tau}{2}\right) x^*\left(t - \frac{\tau}{2}\right) e^{-j(\omega - \theta/2)\tau} d\tau \right] d\theta \\ &\text{with } -\frac{\tau}{2} = \lambda \text{ we get} \\ &= \frac{1}{2\pi} \int_{-\infty}^{\infty} STFT(t, \theta) \left[\int_{-\infty}^{\infty} w(\lambda) x(t + \lambda) e^{-j(\omega - \theta/2)2\lambda} d\lambda \right]^* d\theta \\ &= \frac{1}{\pi} \int_{-\infty}^{\infty} STFT(t, \theta) STFT^*(t, 2\omega - \theta) d\theta \\ &\text{with } \theta = \omega + \theta \text{ follows :} \\ &= \frac{1}{\pi} \int_{-\infty}^{\infty} STFT(t, \omega + \theta) STFT^*(t, \omega - \theta) d\theta \end{aligned}$$

This ends the proof.

A discrete version of the previous relation reads:

$$WD(n, k) = \sum_{i=-N/2}^{N/2} STFT(n, k+i)STFT^*(n, k-i) = \quad (20)$$

$$|STFT(n, k)|^2 + 2\text{Re} \left\{ \sum_{i=1}^{N/2} STFT(n, k+i)STFT^*(n, k-i) \right\}$$

The mathematical formulation of the S-Method (SM) in the discrete form is:

$$SM(n, k) = \sum_{i=-L}^L STFT(n, k+i)STFT^*(n, k-i) =$$

$$= |STFT(n, k)|^2 + 2\text{Re}\{STFT(n, k+1)STFT^*(n, k-1)\} +$$

$$+ 2\text{Re}\{STFT(n, k+2)STFT^*(n, k-2)\} + \dots$$

$$+ 2\text{Re}\{STFT(n, k+L)STFT^*(n, k-L)\}$$

where L determines the number of terms used in the calculation.

It can also be written in the form:

$$SM(n, k) = \sum_{i=-N/2}^{N/2} P(i)STFT(n, k+i)STFT^*(n, k-i)$$

where $P(i) = 1$ for $|i| \leq L$ and $P(i) = 0$ for other values of i .

The S-method with L terms can be written in the form:

$$SM_L(n, k) = \sum_{i=-L}^L STFT(n, k+i)STFT^*(n, k-i)$$

In particular, for given values of L we have:

For $L = 0$, the S-method is identical to the spectrogram

$$SM_0(n, k) = |STFT(n, k)|^2 = STFT(n, k)STFT^*(n, k)$$

For $L = 1$

$$SM_1(n, k) = |STFT(n, k)|^2 + 2\text{Re}\{STFT(n, k+1)STFT^*(n, k-1)\}$$

$$= SM_0(n, k) + 2\text{Re}\{STFT(n, k+1)STFT^*(n, k-1)\}$$

For $L = 2$

$$\begin{aligned} SM_2(n, k) &= |STFT(n, k)|^2 + 2\text{Re}\{STFT(n, k+1)STFT^*(n, k-1)\} + \\ &+ 2\text{Re}\{STFT(n, k+2)STFT^*(n, k+2)\} \\ &= SM_1(n, k) + 2\text{Re}\{STFT(n, k+2)STFT^*(n, k-2)\} \end{aligned}$$

and so on.

The illustration of the S-method vector calculation for $L = 2$ is given in Figure 18.

Note that SM with L terms is obtained by adding one more term to the S-method with $L-1$ terms:

$$SM_L(n, k) = SM_{L-1}(n, k) + 2\text{Re}\{STFT(n, k+L)STFT^*(n, k-L)\}$$

Comment on the number of terms L :

The S-method will produce the same auto terms as the Wigner distribution if we take L such that $(2L + 1)$ is equal to the auto terms width in discrete domain (i.e., to the number of samples within the auto term). In practice it means a few terms, for example $L = 3, 4, \dots, 8, 9$, since most of the auto term energy is located around its maximal value. We will see, in the next examples, that the performance of the S-method is insensitive to L values in a wide range of L values. A precise mathematical proof can be given that the S-method can produce the Wigner distribution for each component separately, in those regions of the time-frequency plane where the components do not overlap.

2.3.1 Example 5.

Consider the same LFM signal $x(t)$ denoted by formula (9). The representation of the signal $x(t)$ in the time domain is given in Figure 19.

$$x(t) = e^{-j160\pi t^2}$$

We calculated SM of a LFM $x(t)$ at the instant $t = 0$, fixed window width $N = 128$, and different L values. Results are shown in Figures 20 and 21. For all instants the S-Method in the time-frequency domain is presented in Figure 22.

2.3.2 Example 6.

Consider two LFM signal components $x(t)$ denoted by the formula (18).

$$x(t) = x_1(t) + x_2(t) = e^{-j12\pi ft^2 - j10\pi ft} + e^{-j12\pi ft^2 + j10\pi ft}$$

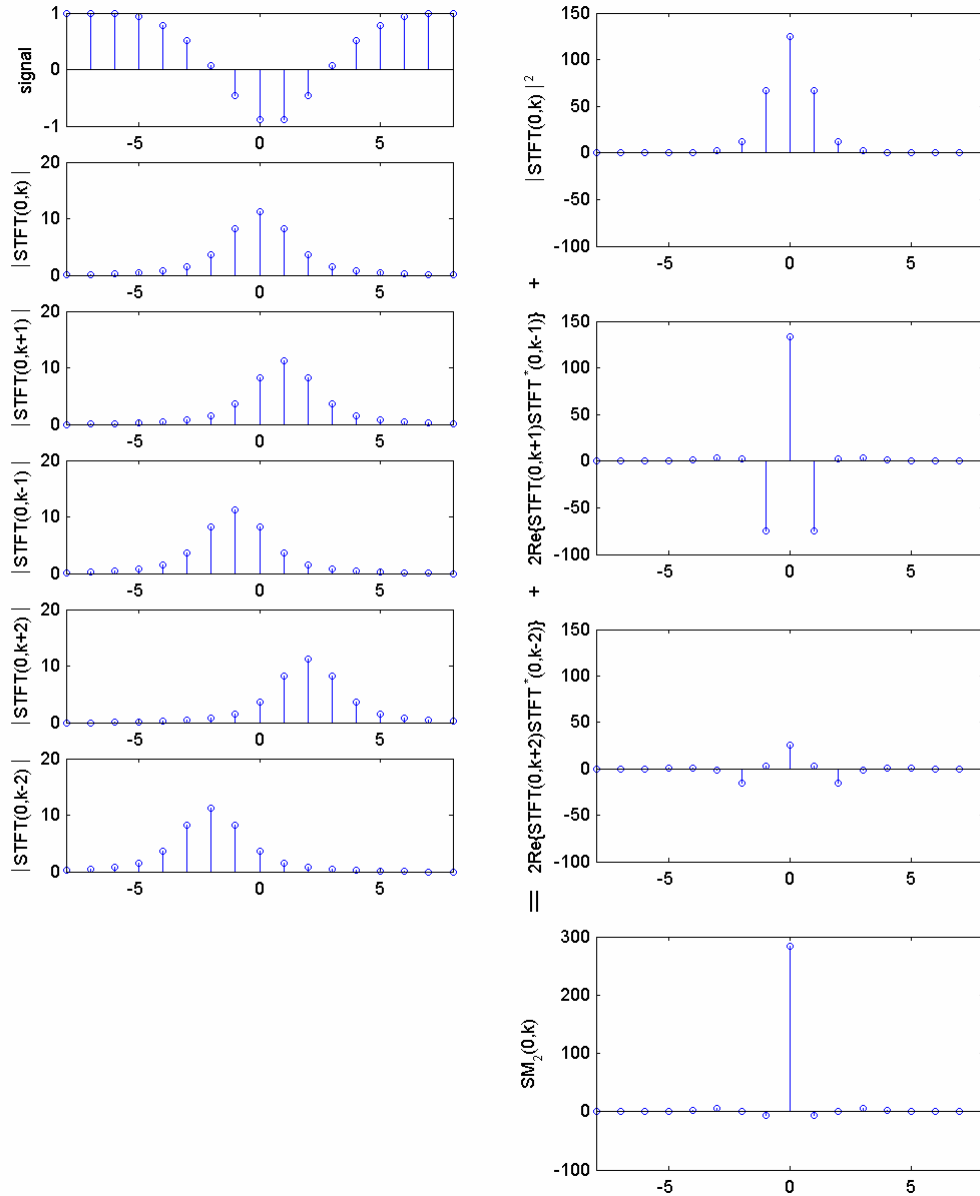


Figure 18: The illustration for the S-method calculation for $L = 2$: Signal (first row), STFT calculated as the signal's fft (second row), STFT shifted for one sample left and right (third and fourth rows), STFT shifted for two samples left and right (fifth and sixth rows). The S-method is equal to the sum of the squared second row + double real part of the product of third and fourth rows + double real part of the product of fifth and sixth rows.

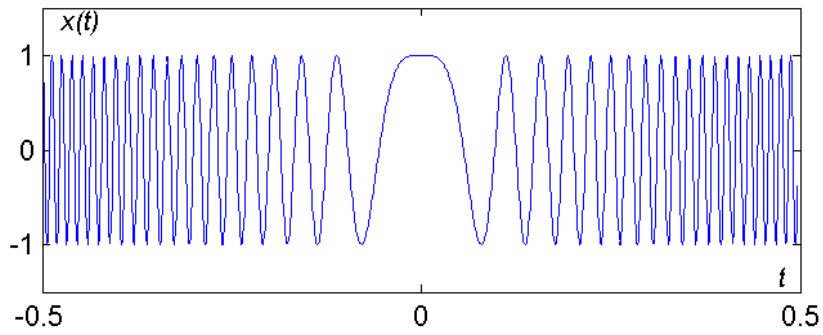


Figure 19: The representation of a Linear Frequency Modulated Signal $x(t)$ in the time domain

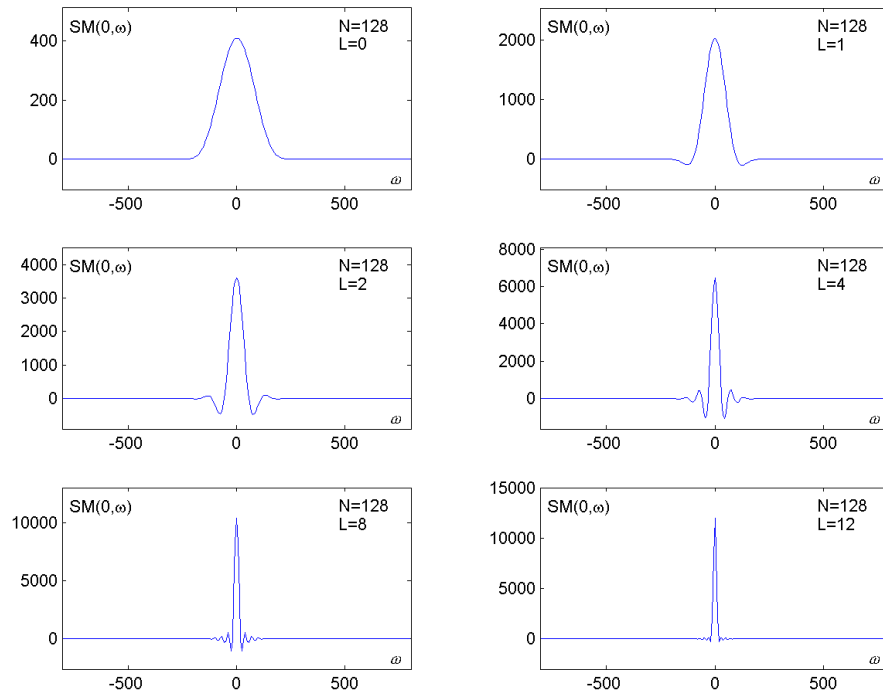


Figure 20: SM of a Linear Frequency Modulated Signal $x(t)$ at the instant $t = 0$, fixed window width $N = 128$, and different L values

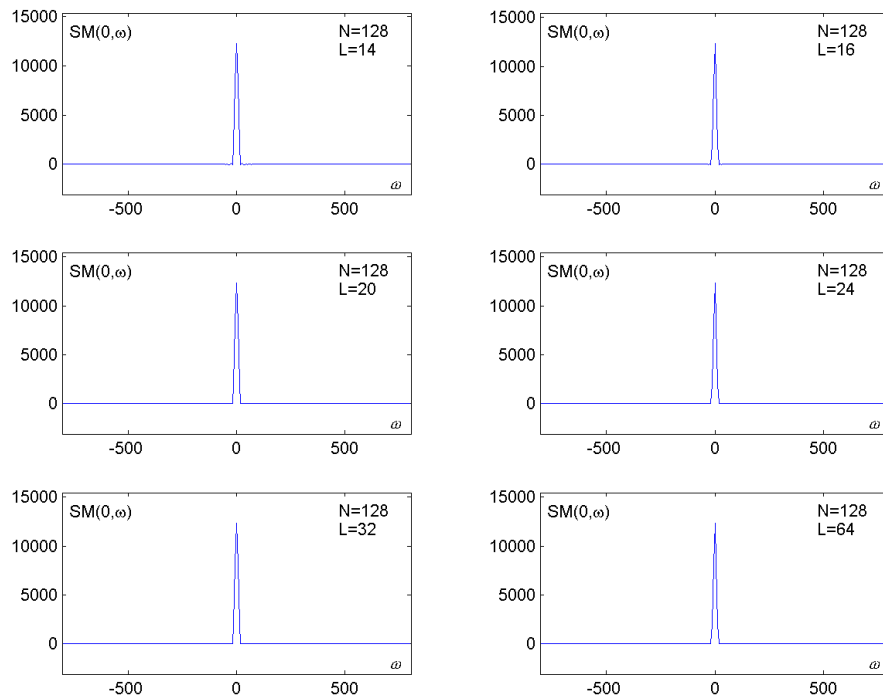


Figure 21: SM of a Linear Frequency Modulated Signal $x(t)$ at the instant $t = 0$, fixed window width $N = 128$, and different L values

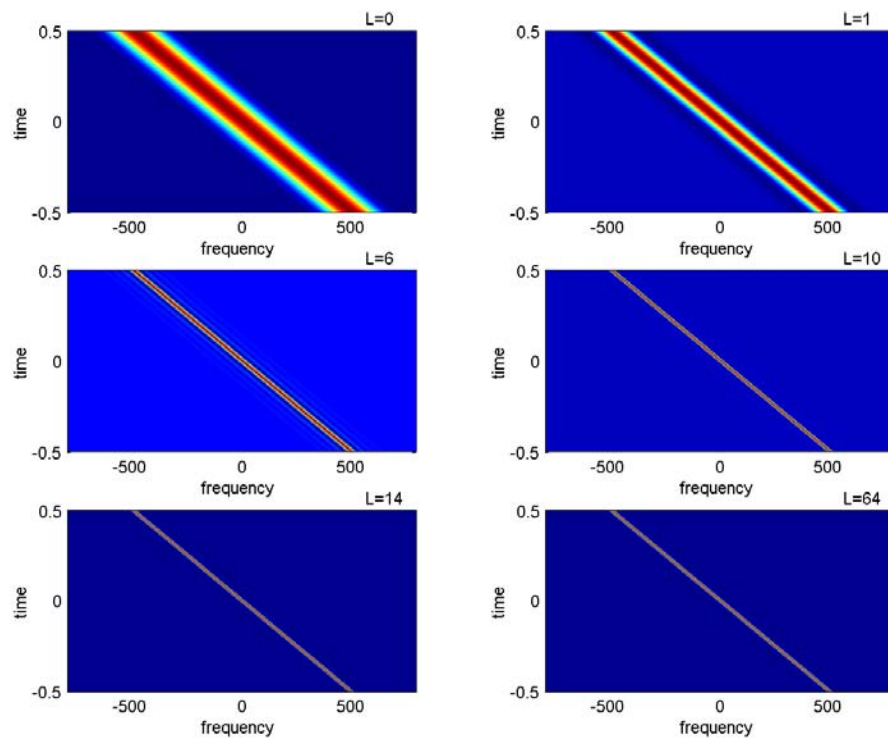


Figure 22: SM of a Linear Frequency Modulated Signal $x(t)$, with fixed window width $N = 128$, and different L values

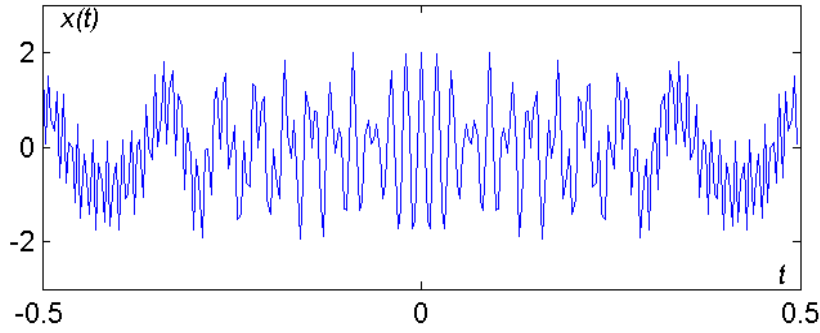


Figure 23: The representation of two LFM signal components $x(t)$ in the time domain

The representation of the signal $x(t)$ in the time domain is given in Figure 23.

We calculated SM of two LFM Signal components $x(t)$ at the instant $t = 0$, fixed window width $N = 128$, and different L values. Results are shown in Figures 24 and 25. In Figure 26 only positive values for SM, for $L=0...12$ values, are shown. The S-Method for all instants in the time-frequency domain is presented in Figure 27.

2.3.3 Example 7.

Consider three LFM signal components $x(t)$ denoted by formula:

$$x(t) = x_1(t) + x_2(t) = e^{-j8\pi ft^2 - j15\pi ft} + e^{-j8\pi ft^2 - j0\pi ft} + e^{-j8\pi ft^2 + j15\pi ft} \quad (21)$$

The representation of the signal $x(t)$ in the time domain is given in Figure 28.

We calculated SM of three LFM signal components $x(t)$ at the instant $t = 0$, fixed window width, $N = 128$, and different L values. The result is shown in Figure 29. In Figure 30 only positive values for SM, for $L=0...12$ values, are shown. The S-Method for all instants in the time-frequency domain is presented in Figure 31.

Figure 32 shows the S method of three Linear Frequency Modulated Signal components $x(t)$ with different signal rates, with fixed window width $N = 128$, and various L values. Figure 33 shows the S method of three nonlinear frequency modulated signal components $x(t)$, with fixed window width $N = 128$, and various L values.

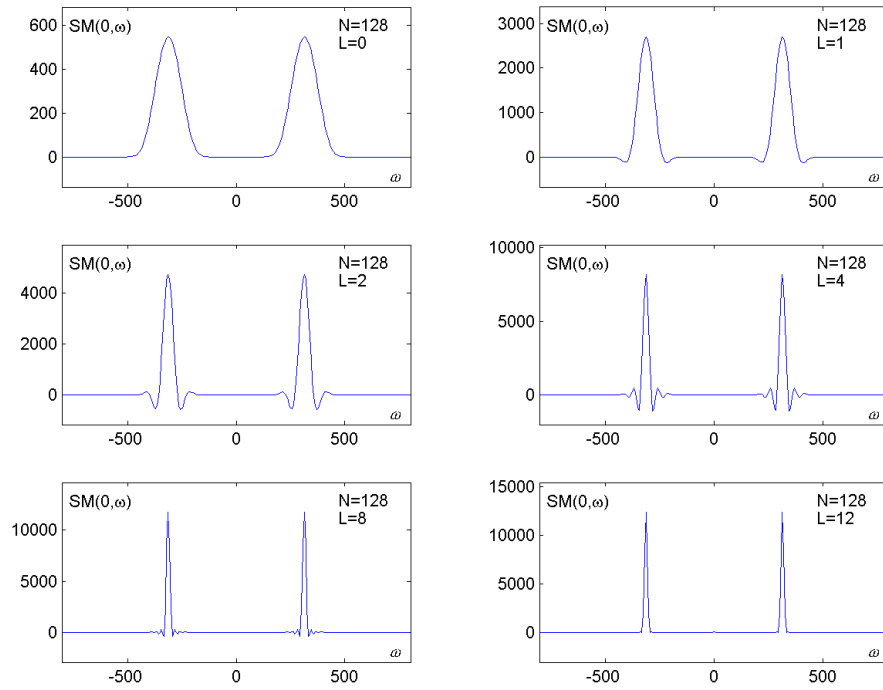


Figure 24: SM of two Linear Frequency Modulated Signal components $x(t)$, with fixed window width $N = 128$, and different L values

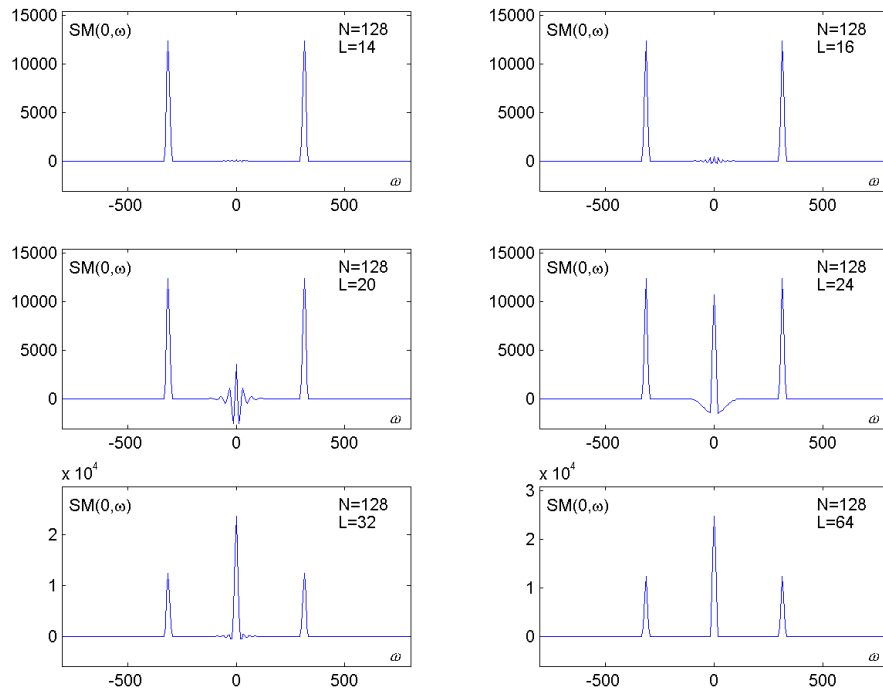


Figure 25: *SM of a two component Linear Frequency Modulated Signal $x(t)$, with fixed window width, $N = 128$, and different L values*

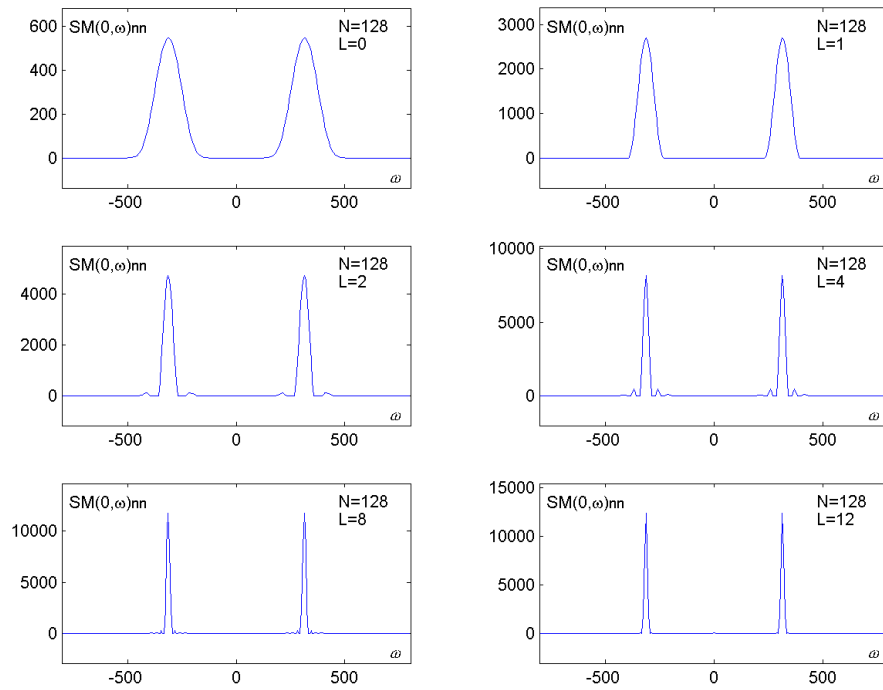


Figure 26: Only non-negative SM of two Linear Frequency Modulated Signal components $x(t)$, with fixed window width $N = 128$, and $L=0...12$ values

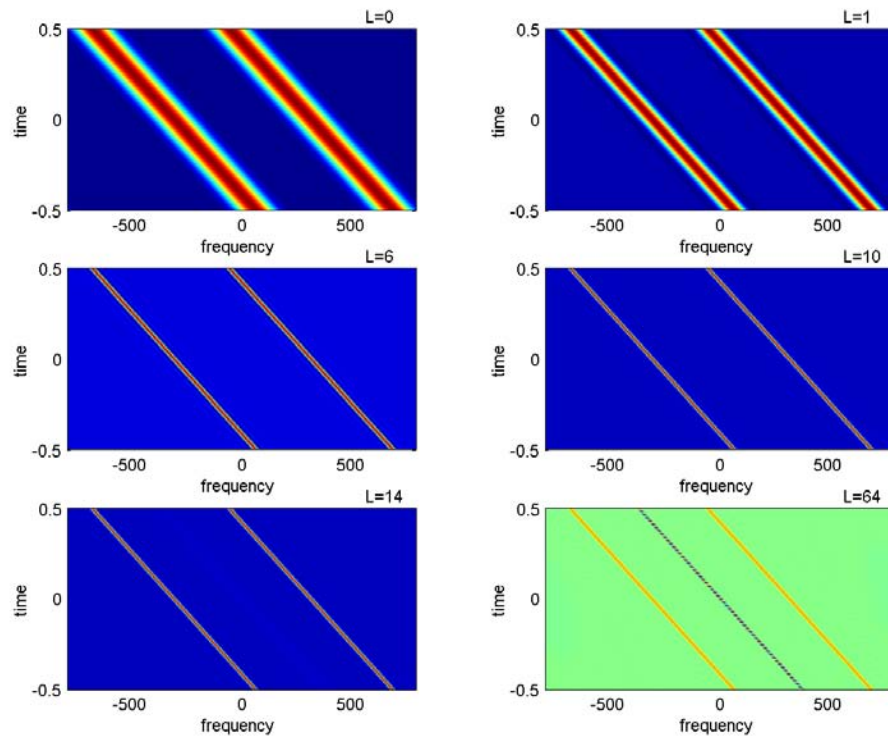


Figure 27: SM of two Linear Frequency Modulated Signal components $x(t)$, with fixed window width $N = 128$, and different L values

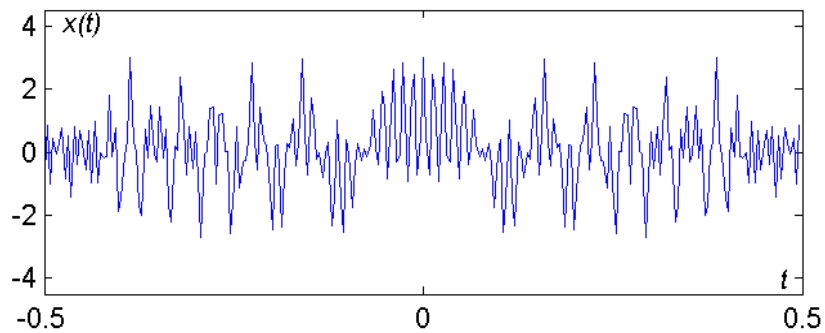


Figure 28: The representation of three LFM signal components $x(t)$ in the time domain

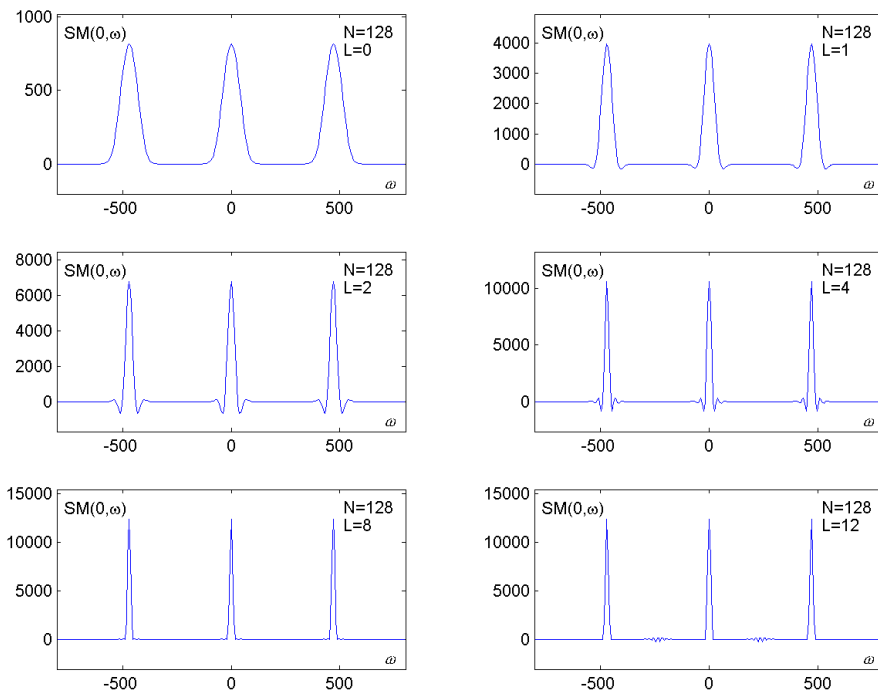


Figure 29: SM of three component Linear Frequency Modulated Signal components $x(t)$, with fixed window width $N = 128$, and different L values

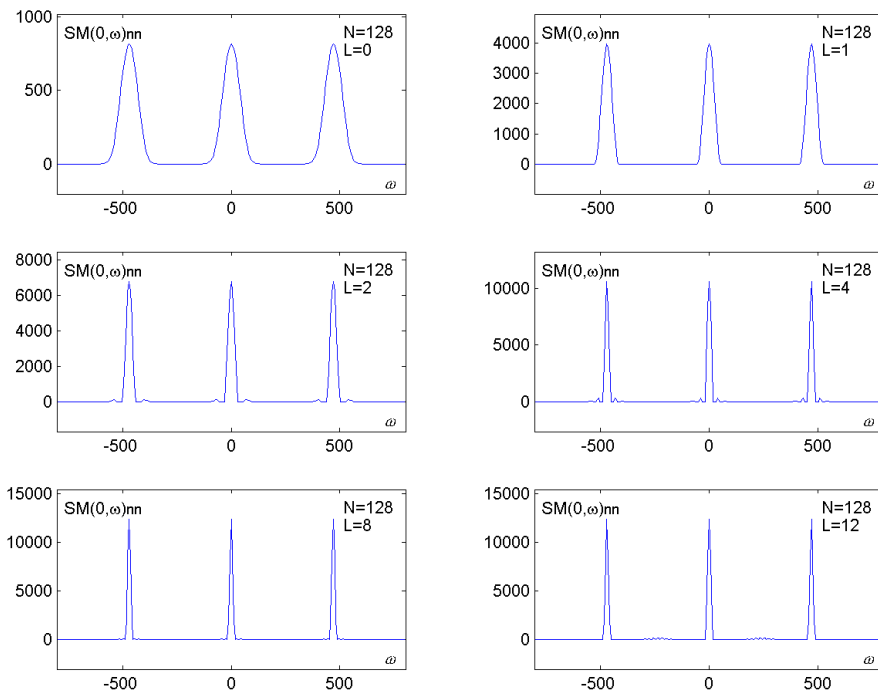


Figure 30: Only non-negative SM of three Linear Frequency Modulated Signal components $x(t)$, with fixed window width $N = 128$, and different L values

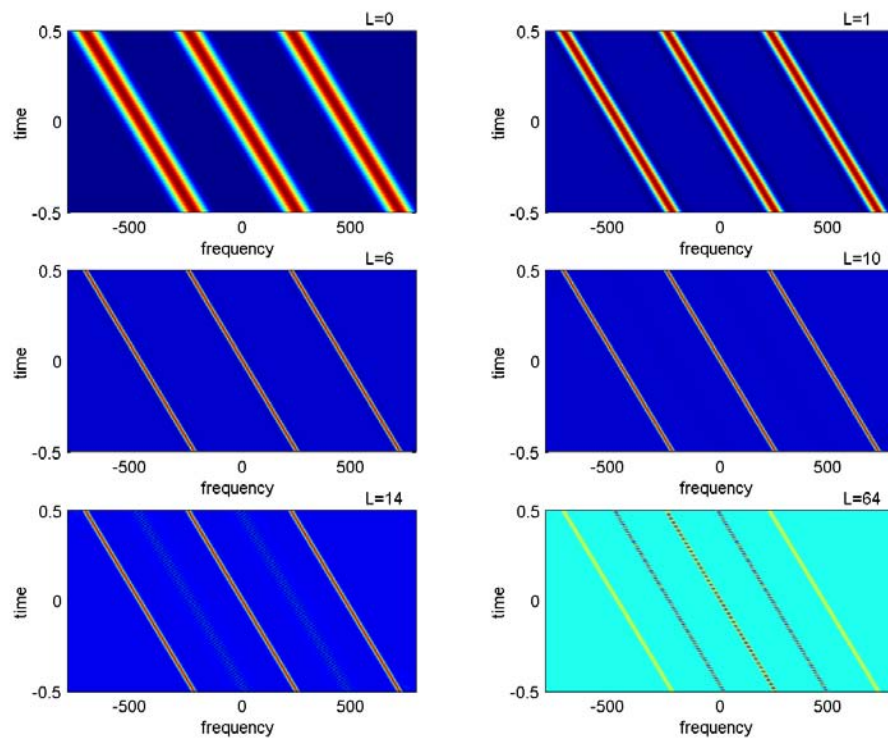


Figure 31: SM of three Linear Frequency Modulated Signal components $x(t)$, with fixed window width $N = 128$, and different L values

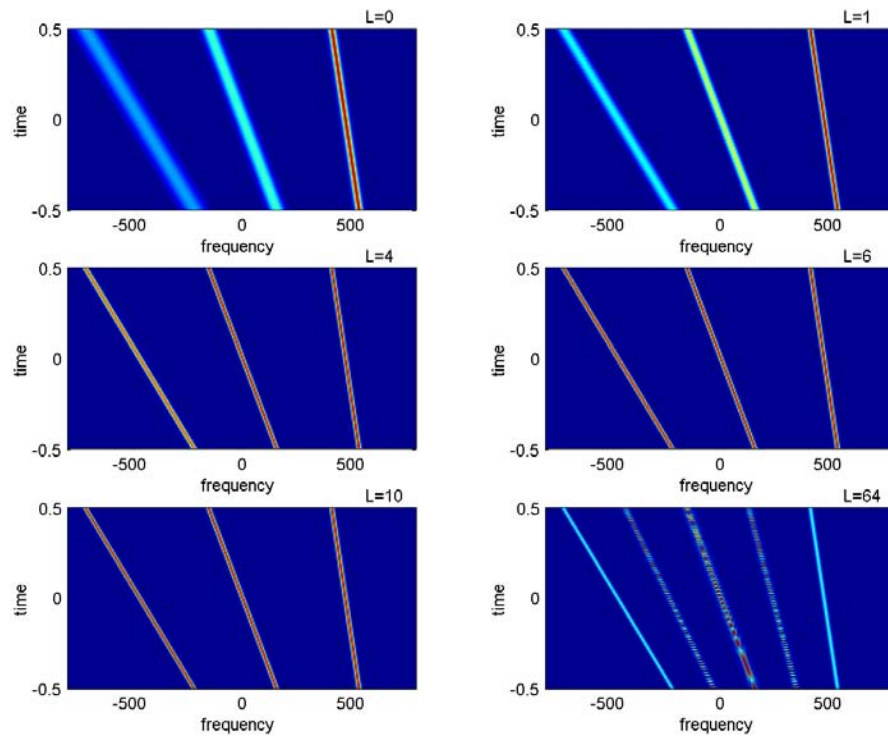


Figure 32: The S method of three Linear Frequency Modulated Signal components $x(t)$ with different signal rates, with fixed window width $N = 128$, and various L values

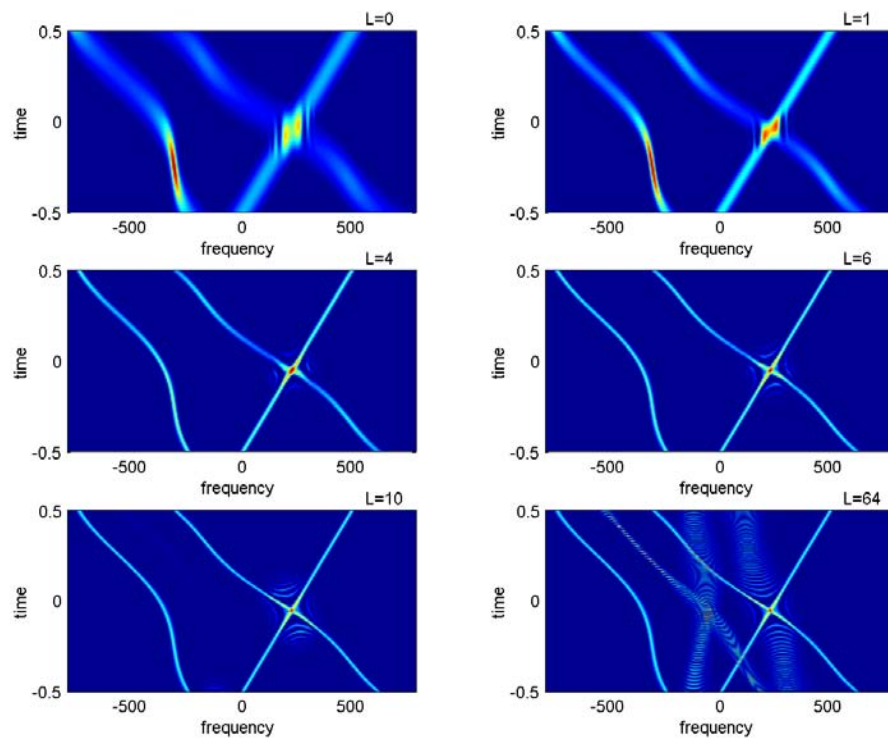


Figure 33: The S method of three nonlinear frequency modulated signal components $x(t)$, with fixed window width $N = 128$, and various L values

3 Wigner distribution based inversion and decomposition

A discrete form of the Wigner distribution is defined by

$$WD(n, k) = \sum_{m=-N/2}^{N/2} f(n+m)f^*(n-m)e^{-j\frac{2\pi}{N+1}2mk}, \quad (22)$$

where we assume that the signal $f(n)$ is time limited within $|n| \leq N/2$ and omit a constant multiplication factor of 2. Inversion relation for the Wigner distribution reads

$$f(n+m)f^*(n-m) = \frac{1}{N+1} \sum_{k=-N/2}^{N/2} WD(n, k)e^{j\frac{2\pi}{N+1}m(2k)}.$$

After substitutions $n_1 = n + m$ and $n_2 = n - m$ we get

$$f(n_1)f^*(n_2) = \frac{1}{N+1} \sum_{k=-N/2}^{N/2} WD\left(\frac{n_1+n_2}{2}, k\right)e^{j\frac{2\pi}{N+1}k(n_1-n_2)}. \quad (23)$$

For cases when $(n_1 + n_2)/2$ is not an integer, an appropriate interpolation is performed in order to calculate $WD((n_1 + n_2)/2, k)$.¹ Introducing the notation,

$$R(n_1, n_2) = \frac{1}{N+1} \sum_{k=-N/2}^{N/2} WD\left(\frac{n_1+n_2}{2}, k\right)e^{j\frac{2\pi}{N+1}k(n_1-n_2)}, \quad (24)$$

we get

$$R(n_1, n_2) = f(n_1)f^*(n_2). \quad (25)$$

Matrix form of (25) reads

$$\mathbf{R} = \mathbf{f}(n)\mathbf{f}^*(n), \quad (26)$$

where: $\mathbf{f}(n)$ is a column vector whose elements are the signal values, $\mathbf{f}^*(n)$ is a row vector (Hermitian transpose of $\mathbf{f}(n)$) and \mathbf{R} is a matrix with the elements $R(n_1, n_2)$, defined by (24).

¹For better understanding of the calculation procedure note that relation (23) is a discrete counterpart of the Wigner distribution inversion in analog domain, that reads:

$$f(t_1)f^*(t_2) = \frac{1}{2\pi} \int_{-\infty}^{\infty} WD((t_1+t_2)/2, \omega)e^{j\omega(t_1-t_2)}d\omega.$$

By discretizing angular frequency $\omega = k\Delta\omega$ and time $t_1 = n_1\Delta t$, $t_2 = n_2\Delta t$, with appropriate definition of discrete values, assuming $\Delta t = 1$, we easily obtain (23).

As for any square matrix, the eigenvalue decomposition of \mathbf{R} reads

$$\mathbf{R} = \mathbf{Q}\mathbf{\Lambda}\mathbf{Q}^T = \sum_{i=1}^{N+1} \lambda_i \mathbf{u}_i(n) \mathbf{u}_i^*(n), \quad (27)$$

where λ_i are eigenvalues and $\mathbf{u}_i(n)$ are eigenvectors of \mathbf{R} . By comparing (26) and (27), it follows that the matrix with elements of form (24) can be decomposed by using only one non-zero eigenvalue. Note that the energy of eigenvectors is equal to 1, by definition $\|\mathbf{u}_1(n)\|^2 = 1$. By comparing (26) and (27), having in mind that there is only one non-zero eigenvalue, we have $\mathbf{f}(n)\mathbf{f}^*(n) = \lambda_1 \mathbf{u}_1(n) \mathbf{u}_1^*(n) = (\sqrt{\lambda_1} \mathbf{u}_1(n))(\sqrt{\lambda_1} \mathbf{u}_1(n))^*$ or

$$\lambda_1 = \left\| \sqrt{\lambda_1} \mathbf{u}_1(n) \right\|^2 = \|\mathbf{f}(n)\|^2 = \sum_{n=-N/2}^{N/2} f^2(n) = E_f,$$

resulting in

$$\lambda_i = E_f \delta(i - 1), \quad (28)$$

where $\delta(i)$ denotes Kronecker symbol. Eigenvector $\mathbf{u}_1(n)$ is equal to the signal vector $\mathbf{f}(n)$ up to the constant amplitude and phase factor. Therefore, an eigenvalue decomposition of the matrix, formed according to (24), can be used to check if an arbitrary 2D function $D(n, k)$ is a valid Wigner distribution.

The same relations can be used in signal synthesis. We start from a given function $D(n, k)$, calculate (24) and perform eigenvalue decomposition (27). The first (largest) eigenvalue and corresponding eigenvector produce a signal such that its Wigner distribution is the closest possible Wigner distribution to the given arbitrary function $D(n, k)$, [11].

Now, this property, along with the S-method, will be used for signal decomposition.

4 S-method definition and basic property

Note that a definition of the STFT is

$$STFT(n, k) = \sum_{m=-N/2}^{N/2} f(n+m) e^{-j \frac{2\pi}{N+1} mk}. \quad (29)$$

Its relationship with (22), as derived in [17], is

$$WD(n, k) = \frac{1}{N+1} \sum_{l=-N/2}^{N/2} STFT(n, k+l) STFT^*(n, k-l).$$

This relation has led to the S-method definition [17, 21]:

$$SM(n, k) = \frac{1}{N+1} \sum_{l=-L}^L STFT(n, k+l) STFT^*(n, k-l) \quad (30)$$

or

$$SM(n, k) = \sum_{l=-N/2}^{N/2} P(l) STFT(n, k+l) STFT^*(n, k-l) \quad (31)$$

with the window function $P(l) = 1/(N+1)$ for $|l| \leq L$ and $P(l) = 0$ elsewhere. The S-method can produce the representation of a multicomponent signal such that the distribution of each component is its Wigner distribution, avoiding cross-terms.

Proposition: Consider a multicomponent signal

$$f(n) = \sum_{i=1}^M f_i(n),$$

where $f_i(n)$ are monocomponent signals. Assume that the STFT of each component lies inside the region $D_i(n, k)$, $i = 1, 2, \dots, M$. Denote the length of i -th region along k , for a given n , by $2B_i(n)$, and its central frequency by $k_{0i}(n)$. The S-method of $f(n)$ is equal to the sum of the individual Wigner distributions, $WD_i(n, k)$, $i = 1, 2, \dots, M$, of each signal's component,

$$SM(n, k) = \sum_{i=1}^M WD_i(n, k), \quad (32)$$

if the regions $D_i(n, k)$, $i = 1, 2, \dots, M$, do not overlap, $D_i(n, k) \cap D_j(n, k) = \emptyset$ for $i \neq j$, and the number of terms L in (30), for a point (n, k) , is defined by:

$$L(n, k) = \begin{cases} B_i(n) - |k - k_{0i}(n)| & \text{for } (n, k) \in D_i(n, k) \\ 0 & \text{elsewhere.} \end{cases} \quad (33)$$

The proof of the proposition is very similar to the one provided for the continuous S-method case and can be found in [19].

Note 1: Real M -component signals may be considered as $2M$ -component complex signals with each region $D_i(n, k)$ being associated with the region $D_{i+M}(n, -k)$. Thus, there is no need for removing negative frequency components in real signals [20].

Note 2: Any window in (30) with a constant number of terms $L \geq \max_{n,k} \{L(n, k)\}$ produces $SM(n, k) = \sum_{i=1}^M W D_i(n, k)$, if the regions $D_i(n, k)$, $i = 1, 2, \dots, M$, are at least $2L$ apart along the frequency axis, i.e., $|k_{0i}(n) - k_{0j}(n)| > B_i(n) + B_j(n) + 2L$, for each i, j and n .

This is the S-method with constant value of L , as it was originally introduced in [17, 18]. The signal dependent method (33) would be more accurate, but also more complex. Constant number of terms L is used here in numerical realization since it is much simpler for implementation, producing satisfactory and robust results.

5 Decomposition of multicomponent signals

For each signal component $f_i(n)$ we can write its inversion formula, corresponding to (23), as

$$\begin{aligned} f_i(n_1)f_i^*(n_2) &= \\ \frac{1}{N+1} \sum_{k=-N/2}^{N/2} W D_i\left(\frac{n_1+n_2}{2}, k\right) e^{j\frac{2\pi}{N+1}k(n_1-n_2)} \\ i &= 1, 2, \dots, M, \end{aligned}$$

if we knew the Wigner distribution $W D_i(n, k)$ of this component. By summing the above relations for $i = 1, 2, \dots, M$ we get

$$\begin{aligned} \sum_{i=1}^M f_i(n_1)f_i^*(n_2) &= \\ \frac{1}{N+1} \sum_{k=-N/2}^{N/2} \sum_{i=1}^M W D_i\left(\frac{n_1+n_2}{2}, k\right) e^{j\frac{2\pi}{N+1}k(n_1-n_2)}. \end{aligned}$$

The equation (32), for the signals that satisfying the presented conditions, this relation reduces to:

$$\begin{aligned} \sum_{i=1}^M f_i(n_1)f_i^*(n_2) &= \\ \frac{1}{N+1} \sum_{k=-N/2}^{N/2} S M\left(\frac{n_1+n_2}{2}, k\right) e^{j\frac{2\pi}{N+1}k(n_1-n_2)}. \end{aligned} \quad (34)$$

By denoting

$$R_{SM}(n_1, n_2) = \frac{1}{N+1} \sum_{k=-N/2}^{N/2} S M\left(\frac{n_1+n_2}{2}, k\right) e^{j\frac{2\pi}{N+1}k(n_1-n_2)} \quad (35)$$

and using the eigenvalue decomposition of matrix \mathbf{R}_{SM} , with the elements $R_{SM}(n_1, n_2)$, we get

$$\mathbf{R}_{SM} = \sum_{i=1}^{N+1} \lambda_i \mathbf{u}_i(n) \mathbf{u}_i^*(n).$$

As in the case of Wigner distribution, we can conclude that $\lambda_i = E_{f_i}$, $i = 1, 2, \dots, M$ and $\lambda_i = 0$ for $i = M + 1, \dots, N$, i.e.,

$$\lambda_i = \sum_{l=1}^M E_{f_l} \delta(i - l). \quad (36)$$

The eigenvectors $\mathbf{u}_i(n)$ will be equal to the signal components $\mathbf{f}_i(n)$, up to the phase and amplitude constants, since the components orthogonality is assumed by the Proposition. Amplitude constants are again contained in the eigenvalues λ_i . Thus, the reconstructed signal can be written as

$$f_{rec}(n) = \sum_{i=1}^M \sqrt{\lambda_i} u_i(n)$$

It is equal to the original signal, up to the phase constants in each component. When we have several components of different energies $\mathbf{f}_1(n)$, $\mathbf{f}_2(n)$, ..., $\mathbf{f}_M(n)$ and when they are all of equal importance in analysis, we can use normalized values of the signal components and calculate the time-frequency representation of

$$\mathbf{f}_{nor}(n) = \sum_{i=1}^M k(\lambda) \mathbf{u}_i(n)$$

by using the weights $k(\lambda) = 1$ in the signal, i.e., by using the eigenvectors as signal components (Capon's way of weighting in the minimal variance high resolution approach, the Appendix).

When there exists a very strong disturbing signal such as sea-clutter in the HFSWR signal we can omit the first, strongest component, and define the reconstructed signal as

$$f_{rec}(n) = \sum_{i=2}^{M_1} \sqrt{\lambda_i} u_i(n)$$

where M_1 is the expected number of components.

5.1 Illustrative example

Consider a signal whose analog form reads:

$$x(t) = e^{j\frac{\pi}{6400}t^2} e^{-\left(\frac{t}{96}\right)^2} + \sum_{k=2}^7 \sqrt{\frac{27-k}{10}} e^{j\omega_k t} e^{-\left(\frac{t-d_k}{16}\right)^2}$$

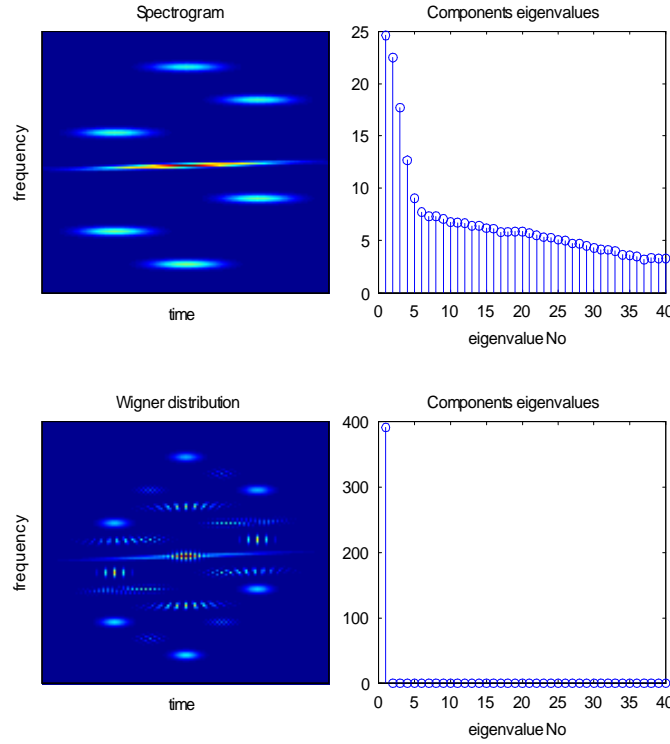


Figure 34: Spectrogram and its eigenvalue decomposition (upper row); Wigner distribution and its eigenvalue decomposition (bottom row).

within the interval $-128 \leq t \leq 127$, where $\omega_2 = -\frac{3\pi}{4}$, $\omega_3 = -\frac{\pi}{2}$, $\omega_4 = -\frac{\pi}{4}$, $\omega_5 = \frac{\pi}{4}$, $\omega_6 = \frac{\pi}{2}$, $\omega_7 = \frac{3\pi}{4}$, $d_2 = d_7 = 0$, $d_3 = d_5 = -64$ and $d_4 = d_6 = 64$. The sampling interval is $\Delta t = 1$. The spectrogram, calculated according to (29), is presented in Fig.34, upper row. The Wigner distribution is presented in Figure 34, bottom row. Based on the Wigner distribution, the elements of matrix \mathbf{R} are calculated by using (24). Eigenvalue decomposition (27) of this matrix produces exactly one non-zero eigenvalue, $\lambda_1 = 390.92$ ($\lambda_2 = 0.00$, $\lambda_3 = 0.00$, ...), being equal to the total signal energy $E_x = 390.14$ (within the numerical calculation error), as expected from (24)-(28).

To illustrate that eigenvalue decomposition of the spectrogram (that is the first step in S-method calculation) does not produce a meaningful result, we have repeated this procedure by using the spectrogram instead of the Wigner distribution in calculation of the elements of \mathbf{R} , according to (24). The eigenvalue decomposition obtained in this way proves that the spectrogram can not be related to a sum of the Wigner distributions of the signal components, Figure 34, upper row (right) .

The S-method of the same signal is calculated by using (29) and (30) with $L =$

12. The obtained results are depicted in Figure 35. The matrix \mathbf{R}_{SM} is formed according to (35). Its eigenvalue decomposition results in the same number of non-zero eigenvalues as the number of signal components. Eigenvalues correspond to the components energies, while the eigenvectors correspond to the normalized signal components, up to the phase constants. The time-frequency representation of the eigenvectors is shown in Figure 36. First seven components correspond to the signal, while the remaining ones are with very small eigenvalues. Energies of discrete signal components are: $E_1 = 119.40$, $E_2 = 50.13$, $E_3 = 48.13$, $E_4 = 46.12$, $E_5 = 44.12$, $E_6 = 42.11$ and $E_7 = 40.11$, while the obtained eigenvalues by using the S-method with $L = 12$ are: $\lambda_1 = 119.40$, $\lambda_2 = 50.18$, $\lambda_3 = 48.19$, $\lambda_4 = 46.19$, $\lambda_5 = 44.18$, $\lambda_6 = 42.17$, $\lambda_7 = 40.15$, $\lambda_8 = 0.68$, ...

The sensitivity of the results with respect to L is quite low within a wide region. We have repeated calculations with values of L from $L = 10$ up to $L = 20$ and obtained almost the same results. The error in components energy, estimated by corresponding eigenvalues, was within $\pm 0.25\%$.

As a decomposition example, we omitted the strongest component and reconstructed the rest of the signal. The obtained time-frequency representation is given in the upper row (right) of Figure 35. The last subplot in Figure 35 presents concentration measure of the components, in logarithmic scale, which will be discussed and used later.

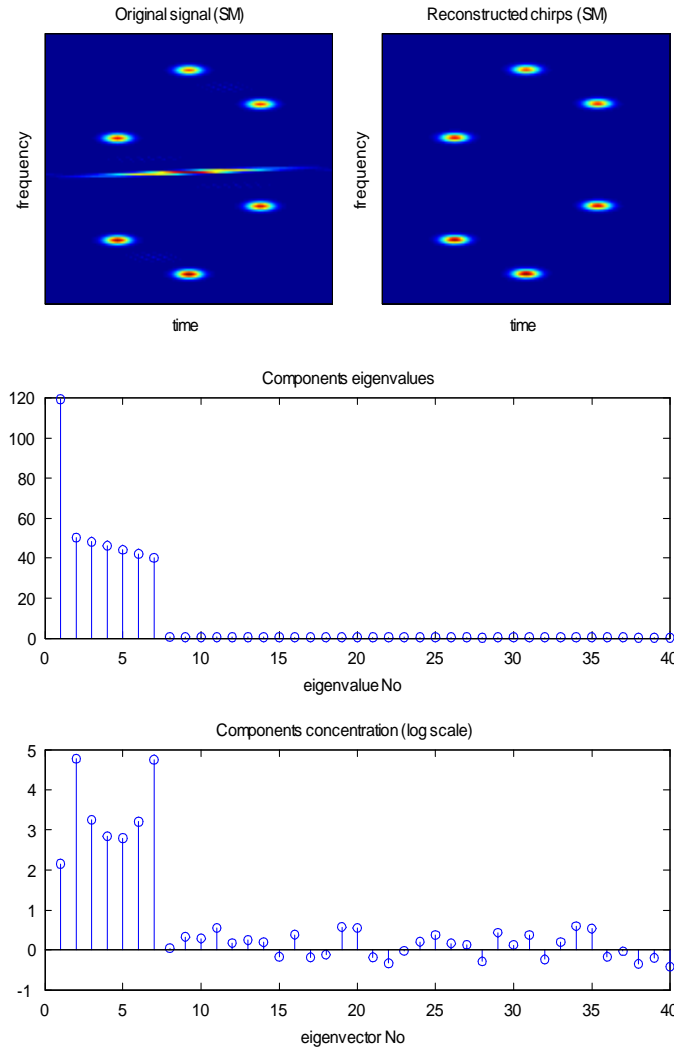


Figure 35: The S-method of original multicomponent signal (first row, left); The S-method of reconstructed signal by using eigenvectors, with omitted first eigenvector-component (first row right); Eigenvalues of the signal's S-method; Measure of concentration of signal components (eigenvectors) in logarithmic scale.

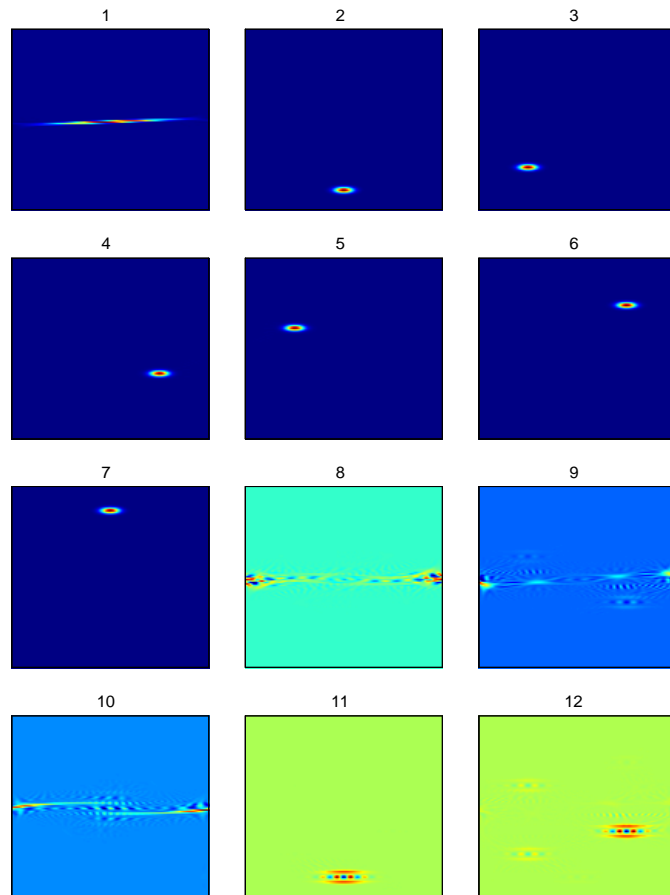


Figure 36: Time-frequency representation of the eigenvectors of the S-method. First seven of them correspond to the normalized signal components. In all subplots horizontal axis is for time and vertical axis is for frequency.

6 Decomposing radar time-varying signals in a strong sea-clutter

We now apply the proposed method to the HFSWR signals with strong sea-clutter. Before we start analysis of experimental data, we will consider some typical situations from the theoretical point of view.

1. When the sea-clutter signal and the target signal are separated in time-frequency plane (occupying unknown and varying ranges in the time-frequency domain) and at the same time, the signal energy is of the clutter energy order, it will be possible to get a decomposition such that the first component corresponds to the stronger clutter and the second component corresponds to the target signal. In this case

$$\begin{aligned}\mathbf{u}_1(n) &\sim \mathbf{f}_{\text{clutter}}(n) = \sqrt{\lambda_1} e^{j\varphi_1} \mathbf{u}_1(n) \\ \mathbf{u}_2(n) &\sim \mathbf{f}_{\text{target}}(n) = \sqrt{\lambda_2} e^{j\varphi_2} \mathbf{u}_2(n)\end{aligned}$$

where φ_1 and φ_2 are arbitrary phase constants. Separate time-frequency representation of the clutter and target signal would be easy in this case.

2. Now consider the case when target signal is much weaker than the sea clutter signal and the value of L is not sufficiently large to complete the integration over clutter and target signal, according to (33). Then, first several components can come from the clutter only (smaller L will increase the number of clutter components). The main part of the clutter and the residual clutter parts are stronger than the target signal. Here, we, now, have to define a criterion to select and resolve the target signal component.

3. The sea-clutter signal and the target signal are close or crossing each other or target signal is highly nonstationary covering wide area. In this case both the clutter and the signal could be separated into few parts, and the criterion for selecting the target components should be defined, as well.

6.1 Criterion for identifying target components

Note that the signal components in HFSWR are single frequency modulated signals, which are concentrated in the time-frequency plane than the clutter residual components. Thus, the criterion for selecting eigenvector(s), being the target signal (or parts of the target signal), could be

$$C_{rit}(p) = \frac{(N+1) \max_{n,k} \{SM_{u_p}(n, k)\}}{\sum_{k=-N/2}^{N/2} \sum_{n=-N/2}^{N/2} |SM_{u_p}(n, k)|}$$

or

$$C_{rit}^-(p) = \frac{(N+1) \max_{n,k} \{SM_{u_p}(n, k)\}}{2 \sum_{k=-N/2}^{N/2} \sum_{n=-N/2}^{N/2} |SM_{u_p}^-(n, k)|} \quad (37)$$

where $SM_{u_p}^-(n, k)$ denotes negative values of $SM_{u_p}(n, k)$. It means that higher concentrated components (greater maximum in the numerator, since all eigenvectors are normalized in energy) with smaller oscillations (smaller mean absolute (negative) value in the denominator) are better candidates for the target signal components. This criterion can be considered as a concentration measure, with infinity power in the numerator and power 1 in the denominator of $C_{rit}(p)$. It can also be understood as the peak-to-average absolute value ratio.

The simplest algorithm is to find the value when $C_{rit}(p)$ reaches a maximal value ($p = p_{\max}$) and assign this eigenvector to the target signal component:

$$\mathbf{f}_{\text{target}}(n) = \mathbf{u}_{p_{\max}}(n).$$

This simple approach works well with most of the considered signals. Of course, the strongest component in decomposition is the clutter, thus $\mathbf{u}_1(n)$ is omitted from the analysis.

For a few considered signals, the target signal component is divided over several eigenvectors, as discussed in cases 2 and 3 mentioned within the previous subsection. In order to deal with these cases, we analyze the range for $C_{rit}(p)$ values. If the whole distribution of one component is concentrated at one point in the time-frequency plane, i.e., $SM_{u_p}(n, k) = A\delta(n - n_0, k - k_0)$, then $C_{rit}(p) = N + 1$. For a component that is uniformly distributed along a single line, i.e., pure linear frequency modulated component, $C_{rit}(p) = 1$. For uniformly spread distribution values over the entire time-frequency plane (obviously not being a signal component) we have $C_{rit}(p) = 1/(N + 1)$. Thus, we can say that if, for example $C_{rit}(i) > P$, where P is of order 1 or just slightly higher, for $i = k, p, \dots, q$, then $\mathbf{u}_i(n)$ are parts of the target signal, i.e.,

$$H(i) = \begin{cases} C_{rit}(i) > P & \mathbf{u}_i(n) \text{ is a target signal component} \\ C_{rit}(i) \leq P & \mathbf{u}_i(n) \text{ is not a target signal component} \end{cases}.$$

Thus, we can take all eigenvectors that satisfy this criterion and form the target signal:

$$\mathbf{f}_{\text{target}}(n) = \sqrt{\lambda_k} \mathbf{u}_k(n) + \sqrt{\lambda_p} \mathbf{u}_p(n) + \dots + \sqrt{\lambda_q} \mathbf{u}_q(n) \quad (38)$$

with $i = k, p, \dots, q$ and $i > 1$, since the first component will always be the strongest one corresponding to the clutter. Note that if L in (30) is not large enough to complete the integration over the clutter, then a few of the largest components will be ones belonging to the clutter and $i > 2$ components should be omitted.

In the time-frequency domain we get

$$SM_{\text{target}}(n, k) = g(\lambda_k)SM_k(n, k) + g(\lambda_p)SM_p(n, k) + \dots + g(\lambda_q)SM_q(n, k) \quad (39)$$

where $g(\lambda)$ is a function of eigenvalue. If we want to take all the components with the same weight $g(\lambda) = 1$, or if we want to keep their original weights $g(\lambda) = \lambda$. Cases between these two are possible, for example $g(\lambda) = \sqrt{\lambda}$.

6.2 Numerical realization

The numerical realization of the S-method (30),(33) is very simple, according to

$$STFT(n, k) = DFT_m\{x(n + m)w(m)\}$$

and

$$SM(n, k) = |STFT(n, k)|^2 + 2 \sum_{i=1}^L \Re[STFT(n, k + i)STFT^*(n, k - i)] \quad (40)$$

or

$$SM_L(n, k) = SM_{L-1}(n, k) + 2\Re[STFT(n, k + L)STFT^*(n, k - L)]$$

where $SM_L(n, k)$ is $SM(n, k)$ calculated with L samples in (30) and $SM_0(n, k) = SPEC(n, k) = |STFT(n, k)|^2$. Symbol $\Re[\cdot]$ stands for real value.

Calculation complexity: The basic step in the S-method realization is in calculation of the STFT by using the FFT algorithms or recursive formulae [17]. The calculation of the STFT in M time instants by using the N samples FFT requires an $MN \log_2 N$ order of basic arithmetic operations (multiplications and additions). Additional block for the S-method calculation, according to (40), requires MNL arithmetic operations. For example, for $N = 1024$ and $L = 10$, the additional number of arithmetic operations is of the same order as the basic STFT calculation. It is significantly less intensive than the calculation of Wigner distribution or any other quadratic representation [17]. In addition, the S-method can be implemented in hardware [21], which makes the calculation complexity problem less important. Furthermore, the coherent integration time in the considered example is quite long. The decomposition of the S-method based matrix is done by using the standard iterative eigenvalue decomposition procedures, with a given number of significant eigenvalues (we used 36 significant eigenvalues). We checked the calculation time in MATLAB algorithms. The eigenvalue decomposition increased this time for 29% of the time required for the calculation of the STFT and the S-method with $L = 10$, $N = 1024$ and $M = 512$.

7 Data analysis and Results

The signals considered here are experimental data of aircraft returns, as used in [23]. The aircraft is a King-Air 200 performing maneuvers, tracked by a HFSWR, with a 10-element linear receiving antenna array. The radar carrier frequency is 5.672 MHz and the pulse repetition frequency is 9.17762 Hz. Each trial corresponds to a block of 256 pulses. Therefore the CIT (coherent integration time) of each signal is 27.89 sec. The King-Air performed two figure-of-eight maneuvers, Figure 37. Each figure-of-eight maneuver consisted of two circles with an approximate diameter of 10km. The first figure-of-eight maneuver was performed at 200 ft (61 m), while the second figure-of-eight maneuver was performed at 500 ft (152 m). The location of the King-Air, when each signal was collected, is marked by a square, Figure 37. Each signal represents a different scenario that could arise when tracking a maneuvering aircraft.

In the HFSWR, beside the target, the signal contains clutter that is primarily due to scattering from the surface of the sea. The received signal of a pulse Doppler radar, taken at a particular range, is viewed in the Fourier transform or Doppler domain. Two sharp peaks, Bragg components, can be observed. These peaks indicate that the dominant form of sea-clutter is due to scattering from sea waves, with wavelengths being half of the wavelength of the radar carrier frequency, travelling radially towards and away from the radar [7], [1]. The Bragg components of the clutter are called 1st order clutter. In addition to the Bragg components, the Doppler spectrum has a continuum called the 2nd order clutter.

7.1 Calculation procedure:

Denote signal length by N . In all considered cases we use $N = 256$.

Step 1. Calculate the STFT (with rectangular window) of the zero-padded signal, oversampled by factor 2.

Step 2. Calculate the S-method of the signal according to (40) for a given L , for example $L = 10$. Size of obtained S-method is $2N = 512$ samples in time and $4N = 1024$ samples in frequency. The central part of the S-method in the frequency domain is equivalent to the Wigner distribution. Note that the frequency range of the S-method is like in the Fourier transform $(-f_s/2, f_s/2)$ and $(-f_s/4, f_s/4)$ for the Wigner distribution, where f_s is the sampling frequency. Only even samples are included in further analysis in order to avoid non-integer indices in (35).

Step 3. Calculate matrix \mathbf{R} according to (35). Since the signal is zero-padded, use only even rows in order to avoid non-integer indices. Since only central part of S-method, and only even samples are used, order of the matrix \mathbf{R} is $N = 256$

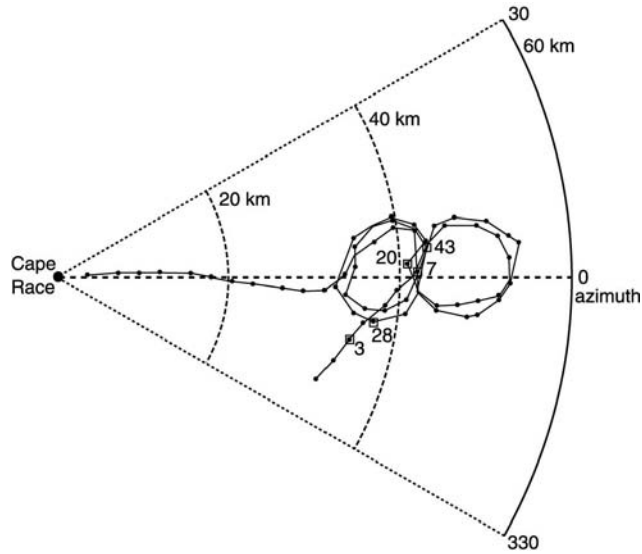


Figure 37: Path of the King-Air 200 as a function of range (in km) and azimuth (in degrees)

Step 4. Decompose \mathbf{R} into eigenvectors and eigenvalues. Note that eigenvectors has the same length as the original signal.

Step 5. Calculate the S-method (40) of the eigenvectors by using the STFT with a window, for example square root Hanning window of 256 samples.

Step 6. Calculate measure (37) and assign the eigenvector corresponding to the maximal measure to the target signal if $C_{rit}^-(p_{\max}) > 2$. If $C_{rit}^-(p_{\max}) \leq 2$ then there is no target signal detected (target signal is too close to the clutter). In this case, repeat steps 1. to 6. with smaller L , for example $L = 4$. If $C_{rit}^-(p_{\max}) > 2$ check if there is any other highly concentrated eigenvector, for example with $C_{rit}^-(p \neq p_{\max}) > 3$. If there is such a highly concentrated eigenvector, it should also be a part of the target signal. Include it according to (38).

Step 7. Show the time-frequency representation of the resulting target signal (44) and calculate its high resolution version (45), with excluded isolated points. High resolution images are obtained by using the high resolution version of the S-method presented in the Appendix. After a high resolution distribution is calculated, the pattern recognition algorithm is used to eliminate instants when isolated points are produced (random maxima at the instants when there is no target signal component). Only the regions where more than 10 connected points of the high resolution S-method exist, are kept for final high resolution presentation.

Step 8. Take the next signal and go to Step 1.

By using this procedure we analyze all positions for the described experiment. The target signal is detected and separated in all cases. In four cases, the target signal was too close to the clutter, and the target was not detected when $L = 10$. The procedure was repeated with $L = 4$, according to the description in step 6, and the target was then detected.

Now, the proposed procedure is used to decompose the signal. The following typical cases are presented here.

- A stationary target signal (aircraft is moving with a constant velocity), far from the clutter, Figure 38. The time-frequency representation of the corresponding eigenvectors is shown in Figure 39.
- A nonstationary target signals far from the clutter, Figures 40, 42 along with time-frequency representation of the eigenvectors, Figure 41, for the signal shown in Figure 40.
- A highly nonstationary target signal covering wide frequency range, Figure 43.
- A nonstationary target signal very close to the clutter, Figure 44.
- A nonstationary target signal intersecting the clutter, Figure 45.

For all the signals, the time-frequency representation (S-method) of the original signal including the clutter, is given (upper right subplot in Figures 38,40,42,43,44,45). Since the clutter is extremely strong, in order to get signal component visible, the limiter is used in time-frequency representation. The upper left subplot represents concentration measure for eigenvectors in all considered cases. Lower subplots present the S-method of the detected target signal component (right) and its highly concentrated version (left). The frequency axis in the highly concentrated representations is scaled to represent target instantaneous radial velocity while dashed line represents target radial velocity obtained by standard FFT technique. Figures 39 and 41 present time-frequency representations of the eigenvectors used for the concentration measure and target signal component detection. Plots for the whole trial are presented in appendix 2.

For comparison with the FFT method, three cases are presented: non-accelerating target far from the Bragg's lines, accelerating target far from the Bragg's lines and the target very close to the Bragg's lines, Figure 46. As expected, in the case of constant velocity (non-accelerating target) the FFT method produces a clear result with a peak corresponding to the Doppler frequency. It is in accordance and in good agreement with the time-frequency result presented in Figure 38. However, in the second case the FFT method is smeared, and the constant frequency estimated based on the FFT does not correspond to the real event of fast varying target velocity,

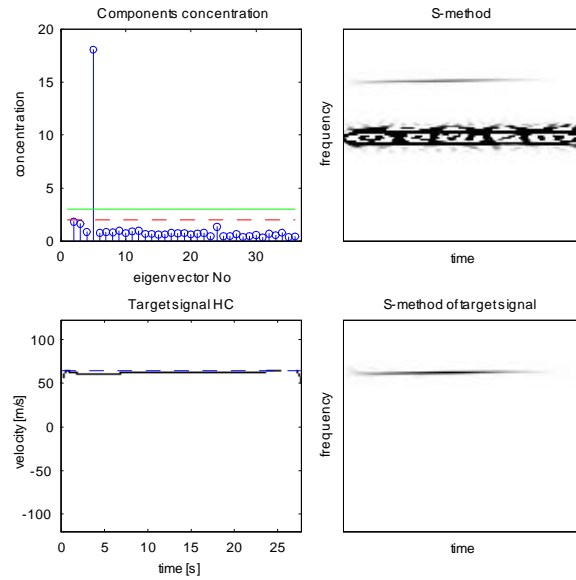


Figure 38: Signal 3 (reference to Figure 1.): Time-frequency representation (top right), Concentration of the eigenvectors time-frequency representations (top left), Time-frequency representation of the detected target signal (bottom right), Highly concentrated time-frequency representation of the detected target signal (bottom left) and FFT estimation of the target velocity (dashed line)

Figure 43. In the third case, there is a slightly smeared peak, but connected to the clutter spectrum. Using the FFT method it would be difficult to conclude that a target exists. The time-frequency based approach clearly indicates that we have a target signal, including its separation by the proposed method, Figure 44. Note that the velocities obtained by using the FFT approach are presented for all considered cases, as mentioned earlier.

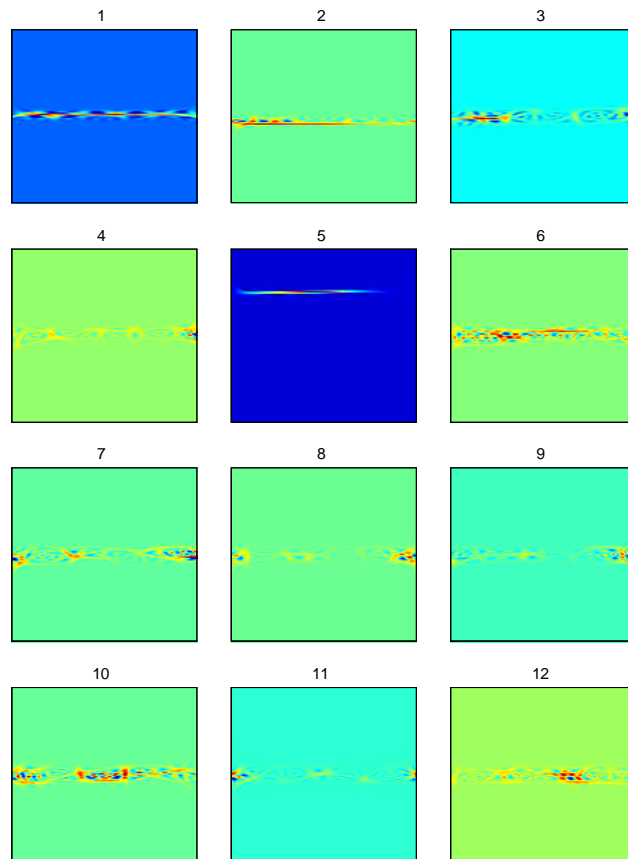


Figure 39: Time frequency representations of the eigenvectors used for the concentration calculation and target signal detection for signal presented in Figure 5. In all subplots horizontal axis is for time and vertical axis is for frequency.

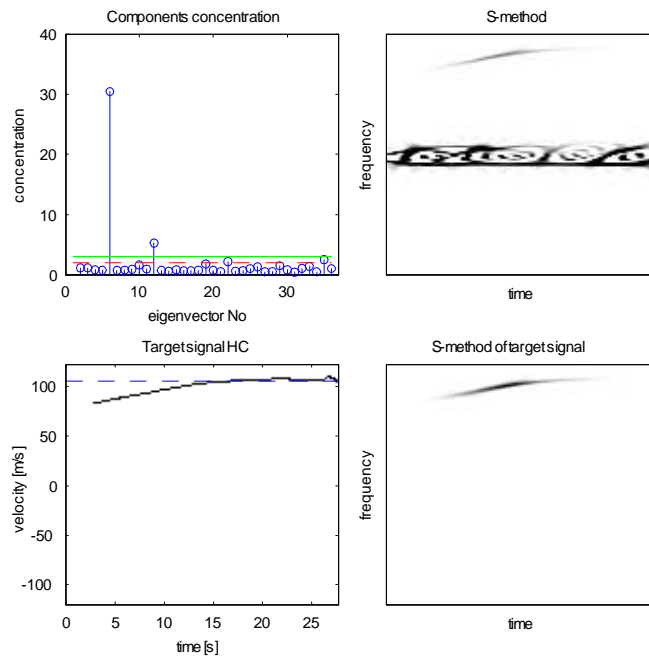


Figure 40: Signal 31: Time-frequency representation (top right), Concentration of the eigenvectors time-frequency representations (top left), Time-frequency representation of the detected target signal (bottom right), Highly concentrated time-frequency representation of the detected target signal (bottom left) and FFT estimation of the target velocity (dashed line)

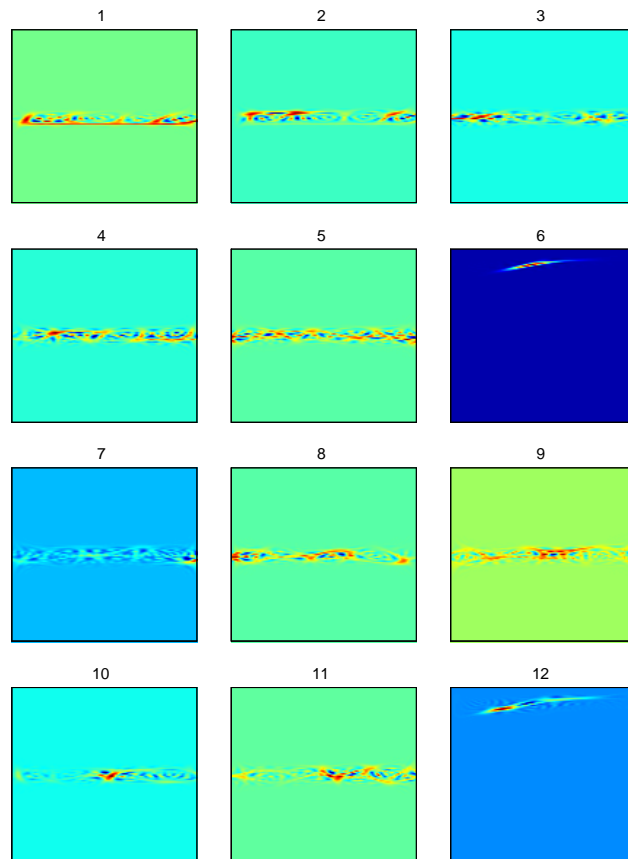


Figure 41: Time frequency representations of the eigenvectors used for the concentration calculation and target signal detection for signal presented in Figure 7. In all subplots horizontal axis is for time and vertical axis is for frequency.

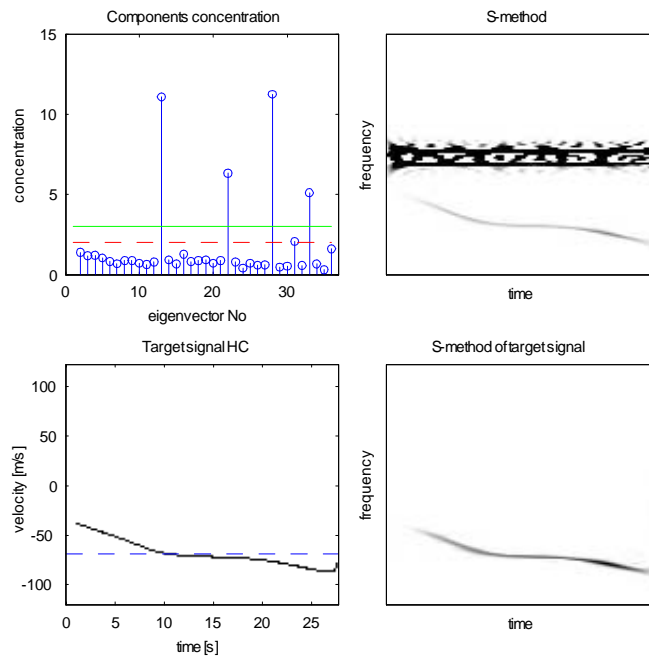


Figure 42: Signal 43: Time-frequency representation (top right), Concentration of the eigenvectors time-frequency representations (top left), Time-frequency representation of the detected target signal (bottom right), Highly concentrated time-frequency representation of the detected target signal (bottom left) and FFT estimation of the target velocity (dashed line)

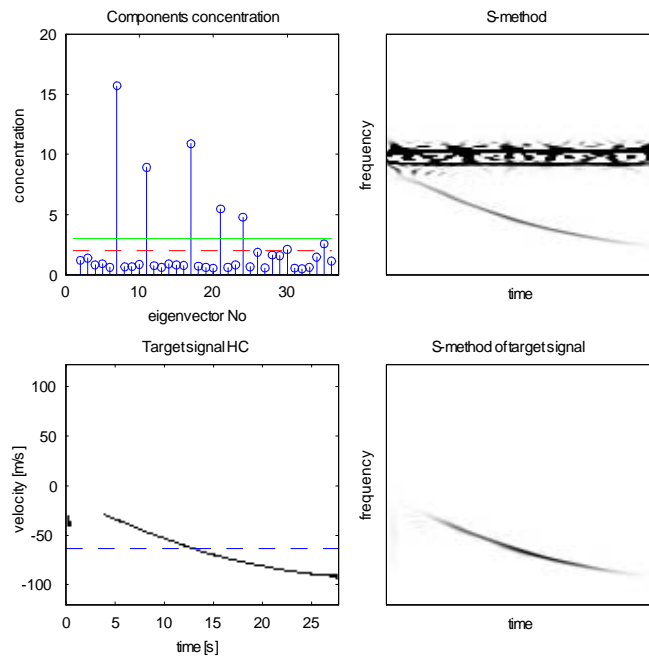


Figure 43: Signal 53: Time-frequency representation (top right), Concentration of the eigenvectors time-frequency representations (top left), Time-frequency representation of the detected target signal (bottom right), Highly concentrated time-frequency representation of the detected target signal (bottom left) and FFT estimation of the target velocity (dashed line)

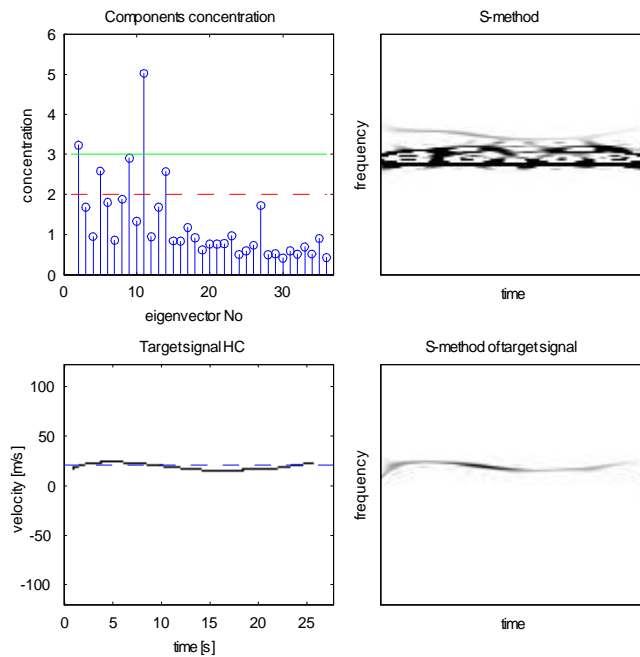


Figure 44: Signal 7: Time-frequency representation (top right), Concentration of the eigenvectors time-frequency representations (top left), Time-frequency representation of the detected target signal (bottom right), Highly concentrated time-frequency representation of the detected target signal (bottom left) and FFT estimation of the target velocity (dashed line)

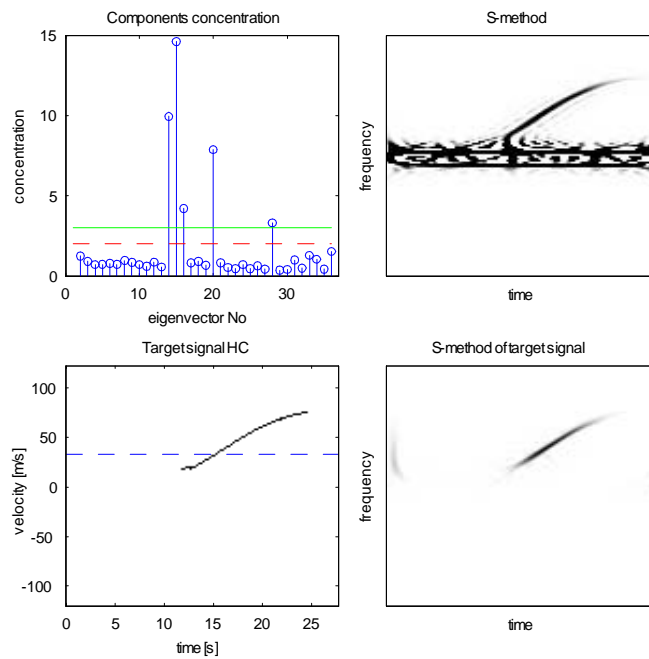


Figure 45: Signal 19: Time-frequency representation (top right), Concentration of the eigenvectors time-frequency representations (top left), Time-frequency representation of the detected target signal (bottom right), Highly concentrated time-frequency representation of the detected target signal (bottom left) and FFT estimation of the target velocity (dashed line)

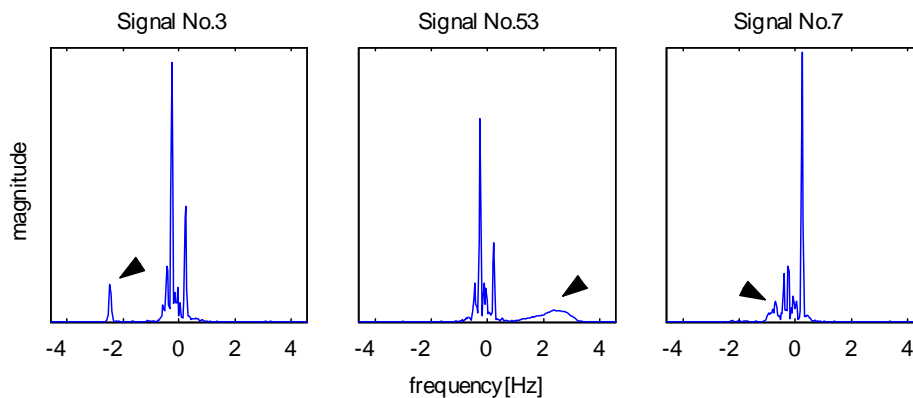


Figure 46: Fourier transform (absolute value) of the three typical signals: nonaccelerating target far from Bragg's lines, accelerating target far from Bragg's lines and target very close to Bragg's lines. Triangle arrows show target signal.

8 Noise Analysis in the Algorithm for Signal Decomposition

Let us consider four component signal, where each component is a Gaussian chirp, contaminated with a white Gaussian complex noise $\varepsilon(n)$:

$$x(n) = \sum_{k=1}^4 A_k e^{j\omega_k(n-d_k) + ja_k \frac{(n-d_k)^2}{2}} e^{-\frac{(n-d_k)^2}{256}} + \varepsilon(n)$$

where $d_1 = d_2 = -64$, $d_3 = 0$, $d_4 = 64$, $\omega_1 = \omega_4 = 0$, $\omega_2 = -\frac{3\pi}{4}$, $\omega_3 = \frac{3\pi}{4}$, $a_1 = a_3 = \frac{1}{256\pi}$, $a_2 = a_4 = -\frac{1}{256\pi}$, and $-128 \leq n \leq 127$. Note that the signal components are separated in the time-frequency plane.

In the noiseless case we will assume that $\varepsilon(n) = 0$ and $A_1 = 1.3$, $A_2 = 1.2$, $A_3 = 1.1$ and $A_4 = 1.0$. Rectangular window of 64 samples length is used and $L = 36$ is chosen in order to satisfy conditions from Proposition 1. The results are presented in Table 1 and Figure 47. The energy of each signal component and corresponding eigenvalue is presented in Table 1. Note that eigenvalues correspond well to the components energies. Figure 47 presents spectrogram of the original signal, TFRs of the first four eigenvectors and TFR of the reconstructed signal.

Component	1	2	3	4
Energy	67.8	57.7	48.5	40.1
Eigenvalue	67.5	57.5	48.3	39.9

Table 1: Component energies and corresponding eigenvalues

The decomposition algorithm is applied to the considered signal with $A_1 = A_2 = A_3 = A_4 = 1$ for signal to noise ratio 0 dB (Figure 48) and -4 dB (Figure 49). Hanning window, 128 samples length and $L = 16$ is used in both cases. In both cases all signal components are separated, and the reconstructed signal is obtained without noise in the parts of the time-frequency plane where there are no signal components. In noisy cases, equal components energies can be used because high noise introduce different eigenvalues in the decomposition process, avoiding possible ambiguity.

8.1 Noise analysis

If the analyzed signal is corrupted with noise, then the assumption that only M eigenvalues are different from zero is not valid. On the other hand, the noise components are distributed over all N eigenvectors.

The described decomposition algorithm is analyzed for various SNR and with different algorithm parameters (L in the S-method calculation and window length in the STFT calculation). The results are shown in Tables 2 and 3. For each combination of SNR, L and window length h , the algorithm is repeated 100 times, giving total of 400 components for detection. The percentage of missed components is shown in tables and used as measure of algorithm robustness.

SNR	$L = 8$	$L = 16$	$L = 32$	$L = 64$
0dB	3.50%	0.00%	0.00%	0.00%
-2dB	6.50%	0.00%	0.50%	0.00%
-4dB	10.00%	3.25%	2.50%	3.50%
-6dB	20.25%	14.75%	11.50%	7.50%
-8dB	35.50%	29.50%	22.75%	21.00%

Table 2: Sensitivity of the proposed algorithm to the choice of L for various SNR. Window length is 128 samples.

SNR	$h = 160$	$h = 128$	$h = 64$
0dB	0.25%	0.00%	0.50%
-2dB	0.50%	0.50%	0.75%
-4dB	3.50%	2.50%	4.50%
-6dB	16.25%	11.50%	14.00%
-8dB	28.00%	22.75%	33.25%

Table 3: Sensitivity of the proposed algorithm to the choice of window length h for various SNR with $L = 64$

It is shown that decomposition algorithm is very robust with respect to the parameter values. The heuristic analysis gives some estimations of parameter values. Namely if we want to obtain Wigner distribution then the parameter L should be equal to the half of the component frequency support (in discrete domain). Time window in STFT calculation should be long enough so the whole component is covered by window. On the other hand very large window can combine two components in one eigenvector.

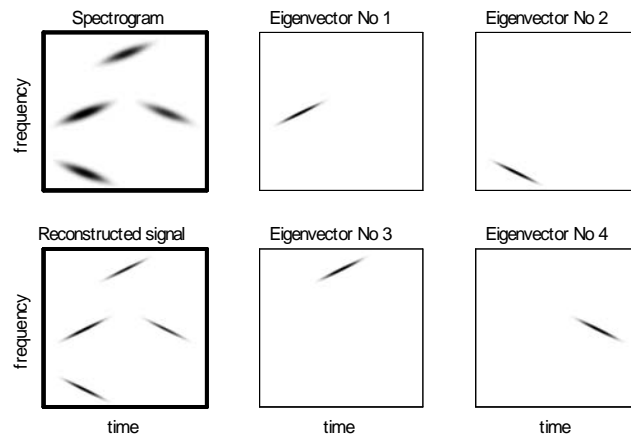


Figure 47: Spectrogram, reconstructed signal and TFRs of the first four eigenvectors - noiseless case

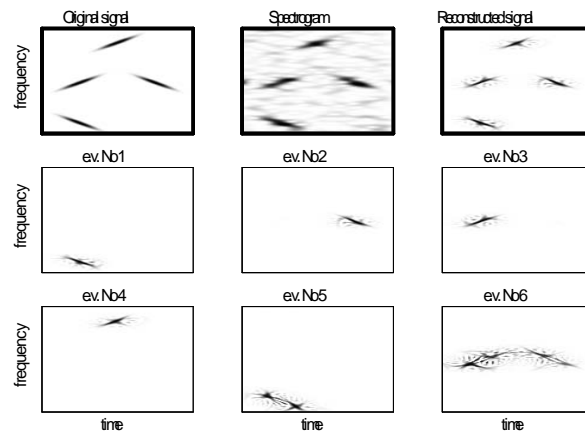


Figure 48: Spectrogram of noisy signal, eigenvectors TFRs and TFR of the reconstructed signal for 0dB SNR

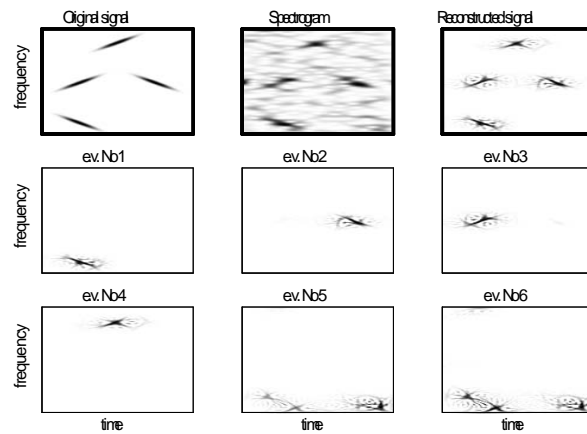


Figure 49: Spectrogram of noisy signal, eigenvectors TFRs and TFR of the reconstructed signal for -4dB SNR.

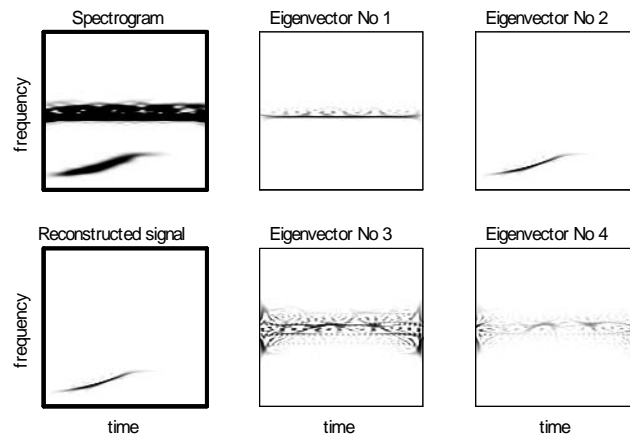


Figure 50: Decomposition of a real HF radar signal in a strong sea-clutter (realization 1)

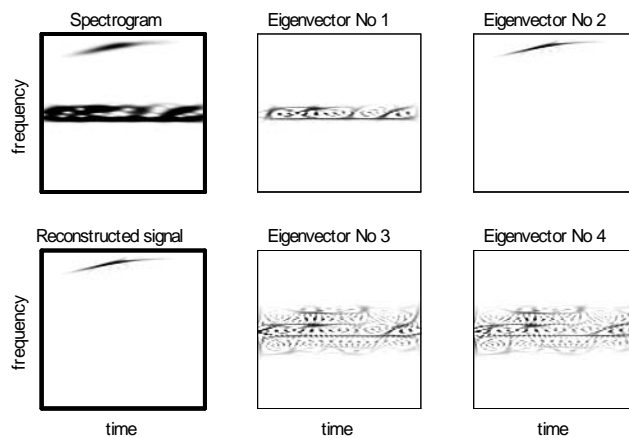


Figure 51: Decomposition of a real HF radar signal in a strong sea-clutter (realization 2)

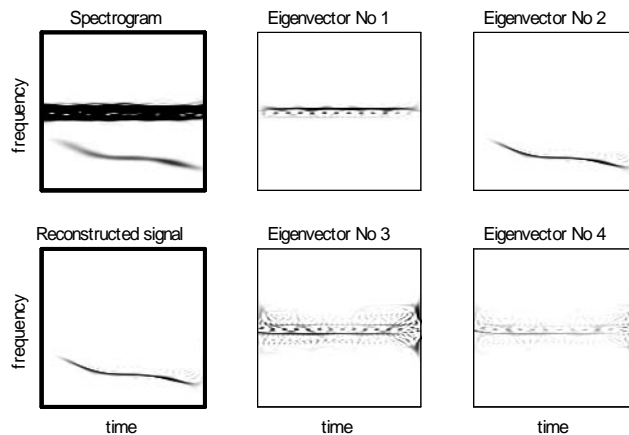


Figure 52: Decomposition of a real HF radar signal in a strong sea-clutter (realization 3)

9 Conclusion

The analysis and processing of radar signals are usually performed in the time or frequency domain. These methods can be inefficient in the cases when significant time variations of frequency content are present, like as in the High-Frequency Surface-Wave Radar (HFSWR) radar signals considered in this report.

This report examines the possibility of improving the detection of accelerating targets using High-Frequency Surface-Wave Radar (HFSWR) in the presence of sea-clutter. Because we are dealing with high speeds and accelerations, the time-frequency analysis has the capability of improving detection, since its resolution abilities are not reduced by a spread in the Doppler signature.

In this report, we proposed a new time-frequency based signal decomposition method. This approach is based upon the eigenvalue decomposition method, combined with the S-method that produces a sum of the Wigner distribution of individual signal components. The proposed decomposition method is theoretically derived. The efficiency and accuracy of the proposed decomposition method is demonstrated on simulated examples. Then, it is used in improving the analysis of signals obtained from a maneuvering low-altitude aircraft using HFSWR in the presence of sea-clutter. Since we are dealing with high speeds and accelerations of the aircraft, the time-frequency method improves the detection, because its resolution abilities are not reduced by a spread in the Doppler signature. The study performed by using the new method demonstrates that the use of time-frequency signal decomposition can improve target velocity estimation and detection performance of the HFSWR. The method provides true time-varying Doppler shift within the considered time, which is not possible with the Fourier transform method that provides only its average value. In addition, the proposed method successfully detects the target signal in all cases of the presented real experiment, which is not the case when the detection is performed by the Fourier transform method.

The noise analysis is performed in the algorithm for signal decomposition and it is shown that the choice of algorithm parameters does not have a great influence on the decomposition process. The method presented here is not restricted to this application, but it can be applied also in various other settings of nonstationary signal analysis and filtering, for example, moving target identification in Inverse Synthetic Aperture Radar (SAR) images and micro-Doppler separation from Inverse Synthetic Aperture Radar (ISAR) images, etc.

Although this new approach demonstrates the improved detection performance of an accelerated air target using HFSWR in sea-clutter environment, a more detailed analysis will be performed in a future study in relation to other clutter environments such as ionosphere, meteors, and lighting environments. Furthermore, the s-method

based detectors will be developed for real-time operational scenarios and will then be compared with existing Fourier Transform based detectors. Once the new approach outperforms the currently available detector methods, numerically efficient algorithms will be developed for real-time operations.

References

1. D. Barrick: "First-order theory and analysis of MF/HF/VHF scatter from the sea", *IEEE Trans. on Antennas and Propagation*, vol.20, No.1, Jan.1972, pp.2-10.
2. B. Boashash, B. Ristic: "Polynomial time-frequency distributions and time-varying higher order spectra: Applications to analysis of multicomponent FM signals and to treatment of multiplicative noise" *Signal Processing*, vol.67, no.1, May 1998, pp.1-23.
3. B. Boashash, Ed.: *Time-frequency signal analysis and processing*, Elsevier, 2003.
4. G.F. Bourdeaux-Bartels: "Time-varying signal processing using Wigner distribution synthesis techniques", in *The Wigner Distribution-Theory and Applications in Signal Processing*, W.Mecklenbrauker, Ed, Amsterdam: Elsevier 1997.
5. V.C. Chen and H. Ling: *Time-frequency transforms for radar imaging and signal analysis*, Artech House, Boston, MA, USA, 2002.
6. L. Cohen, *Time-frequency analysis*, Prentice-Hall Inc., New York, USA, 1995.
7. D.D. Crombie: "Doppler spectrum of sea echo at 13.56 Mc/s". *Nature*, No.175, 1955, pp.681-682.
8. G.S. Cunningham, W.J. Williams: "Vector-valued time-frequency representations", *IEEE Trans. on Signal Processing*, vol. 44, no.7, July 1996, pp.1642 - 1656.
9. A. Francos, M. Porat: "Analysis and synthesis of multicomponent signals using positive time-frequency distributions", *IEEE Trans.on Signal Processing*, vol.47, no.2, Feb.1999, pp.493-504.
10. P. Goncalves, R.G. Baraniuk: "Pseudo affine Wigner distributions: definition and kernel formulation", *IEEE Trans.SP*, vol.46, no.6, June 1998, pp.1505-1516.
11. F. Hlawatsch, W. Krattenthaler: "Bilinear signal synthesis", *IEEE Trans. on Signal Processing*, vol. 40 , no.2, Feb. 1992, pp.352 - 363,
12. J. Jeong, W.J. Williams: "Kernel design for reduced interference distributions" *IEEE Trans. on Signal Processing*, vol.40, Feb.1992, pp.402-412.

13. W. Mu, M.G. Amin, Y. Zhang: "Bilinear signal synthesis in array processing", *IEEE Trans. on Signal Processing*, vol. 51, no. 1, Jan. 2003, pp.90-100.
14. S. Qian, D. Chen: *Joint time-frequency analysis: methods and applications*, Prentice-Hall Inc., New York, USA, 1996.
15. C. Richard: "Time-frequency-based detection using discrete-time discrete-frequency Wigner distributions", *IEEE Trans. on Signal Processing*, vol.50, no.9, Sept.2002, pp.2170-2176.
16. L. L. Scharf and B. Friedlander: "Toeplitz and Hankel kernels for estimating time-varying spectra of discrete-time random processes," *IEEE Trans. Signal Process.*, vol. 49, no.1, pp. 179–189, 2001.
17. LJ. Stanković: "A method for time-frequency analysis", *IEEE Trans. on Signal Processing*, vol.42, Jan. 1994, pp. 225-229.
18. LJ. Stanković: "An analysis of some time-frequency and time-scale distributions" *Annales Telecomm.*, Sep/Oct. 1994, pp.505-517.
19. LJ. Stanković and J.F. Böhme: "Time-frequency analysis of multiple resonances in combustion engine signals," *Signal Processing*, vol.79, no.1, pp.15-28, Nov.1999.
20. LJ.Stanković, I.Djurović: "A note on 'An overview of aliasing errors in discrete-time formulations of time-frequency representations' ", *IEEE Trans.on Signal Processing*, vol.49, no.1, Jan.2001, pp.257-259.
21. S. Stanković, LJ. Stanković: "An architecture for the realization of a system for time-frequency analysis", *IEEE Trans.CAS-II*, vol. 44, July 1997, pp.600-604.
22. S. Stanković, The auto-term representation by the reduced interference distributions; The procedure for a kernel design, *IEEE Trans. on Signal Processing*, Vol.44, No.6, June 1996, pp.1557-1564.
23. T. Thayaparan and S. Kennedy: "Detection of a manoeuvring air target in sea-clutter using joint time-frequency analysis techniques", *IEE Proc.-Radar Sonar Navig.*, vol. 151, No. 1, Feb.2004, pp.19-30.
24. T. Thayaparan, G. Lampropoulos, S.K. Wong, E. Riseborough.(2003). "Focusing ISAR images using adaptive joint time-frequency algorithm on simulated and experimental radar data", *DRDC Ottawa TM 2003-089, Defence R&D Canada - Ottawa*.
25. A. Yasotharan, T. Thayaparan: "Strengths and limitations of the Fourier method for detecting accelerating targets by pulse Doppler radar", *IEE Proc. Radar, Sonar and Navigation*, vol.149, no.2, pp.83-88.

26. T. Thayaparan and S. Kennedy, "Detection of a manoeuvring air target in sea-clutter using joint time-frequency analysis techniques", *IEE Proc.-Radar Sonar Navig.*, vol. 151, No. 1, Feb.2004, pp.19-30.

10 Appendix 1: High-resolution S-method with relation to the Capon's method

As shown in [16] all spectral estimators can be considered as either being smoothed or being cross-calculated. The first family leads to the variations of smoothed spectrograms, while the other leads to the variations of the estimators defined in [17]. Here, we will show that the Capon's method can be considered as a version of the smoothed spectrograms (spectrograms of eigenvectors for close signal components and spectrograms of signal components for separated components). A form of highly concentrated distributions based on the S-method may be defined in an analog manner, using the analysis presented in this paper.

The Capon's filtering method applied to $N + 1$ samples of a signal $f(n)$, being a sum of complex sinusoids $\exp(j\omega_i n)$, denoted in a vector form as $\mathbf{f}(n)$ results in the distribution

$$S_{Cap}(n, k) = \frac{1}{\mathbf{a}^*(k) \hat{\mathbf{R}}_{\mathbf{f}}^{-1} \mathbf{a}(k)}, \quad (41)$$

where $*$ denotes Hermitian transpose and $\mathbf{a}(k) = [1 \ e^{j2\pi k/(N+1)} \dots e^{j2\pi k}]^T$, with

$$\hat{\mathbf{R}}_{\mathbf{f}} = E\{\mathbf{f}(n)\mathbf{f}^*(n)\}. \quad (42)$$

In practice, the autocorrelation matrix $\hat{\mathbf{R}}_{\mathbf{f}}$ is estimated by:

$$\hat{\mathbf{R}}_{\mathbf{f}}(n, K) = \frac{1}{K} \sum_{p=1}^K \mathbf{f}(n+p)\mathbf{f}^*(n+p) + \rho \mathbf{I} = \frac{1}{K} \mathbf{Q}\mathbf{Q}^* + \rho \mathbf{I}, \quad (43)$$

where \mathbf{I} is the identity matrix used for regularization and \mathbf{Q} is the matrix whose columns are signal vectors $\mathbf{f}(n+p)$, $p = 1, \dots, K$.

The Capon's form can be written by using eigenvalue decomposition of the autocorrelation matrix $\hat{\mathbf{R}}_{\mathbf{f}}(n, K)$ as

$$\hat{\mathbf{R}}_{\mathbf{f}}(n, K) = \frac{1}{K} \mathbf{Q}\mathbf{Q}^* + \rho \mathbf{I} = \frac{1}{K} \mathbf{V}\mathbf{\Lambda}\mathbf{V}^* + \rho \mathbf{I},$$

By using this decomposition, we can write

$$\hat{\mathbf{R}}_{\mathbf{f}}^{-1}(n, K) = \frac{1}{\rho} \left[\mathbf{I} - \sum_{p=1}^K \left(1 + \frac{\rho K}{\lambda_p}\right)^{-1} \mathbf{V}_p \mathbf{V}_p^* \right]$$

where \mathbf{V}_p are eigenvectors and λ_p are eigenvalues of $\hat{\mathbf{R}}_{\mathbf{f}}(n, K)$. The Capon's form then reads

$$S_{CapK}(n, k) = \frac{\rho}{N + 1 - \sum_{p=1}^K \frac{\lambda_p}{K\rho + \lambda_p} SPEC_{V_p}(n, k)},$$

where $SPEC_{V_p}(\omega, t)$ are the spectrograms of the eigenvectors and $\rho \rightarrow 0$. For separated components the eigenvectors correspond to the signal components, summed with the same weights.

In our case, the S-method form that corresponds to the Capon's form would lead to the factor of

$$SM_{nor}(n, k) = \sum_{p=1}^K SM_{u_p}(n, k)$$

instead of $\sum_{p=1}^K SPEC_{V_p}(n, k)$ in the Capon's form, resulting in a distribution:

$$\begin{aligned} SM_{CK}(n, k) &= \frac{\rho}{N + 1 - \sum_{p=1}^K \rho_p SM_{u_p}(n, k)} \\ &= \frac{A}{1 - \sum_{p=1}^K c_p SM_{u_p}(n, k)}, \end{aligned} \quad (44)$$

where $A = \rho/(N + 1)$ and $c_p = \rho_p/(N + 1)$.

In the realization we used a very simple normalized version of the highly concentrated S-method:

$$SM_{CK}(n, k) = \frac{1}{1 - \sum_{p=1}^K \frac{SM_{u_p}(n, k)}{1.01 \max_k \{SM_{u_p}(n, k)\}}}. \quad (45)$$

11 Appendix 2: Plots for the whole trial

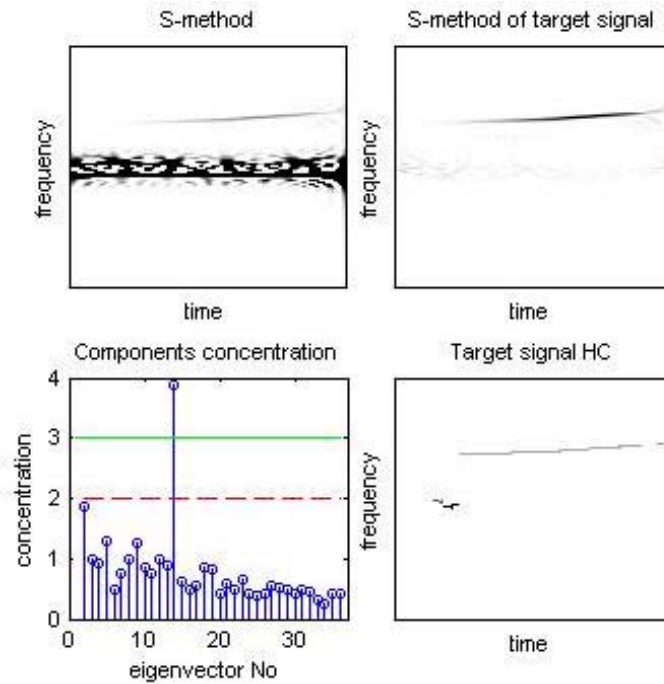


Figure 53: Signal 1- Concentration of the eigenvectors time-frequency representations (bottom left), Time-frequency representation of the detected target signal (top right), Highly concentrated time-frequency representation of the detected target signal (bottom right)

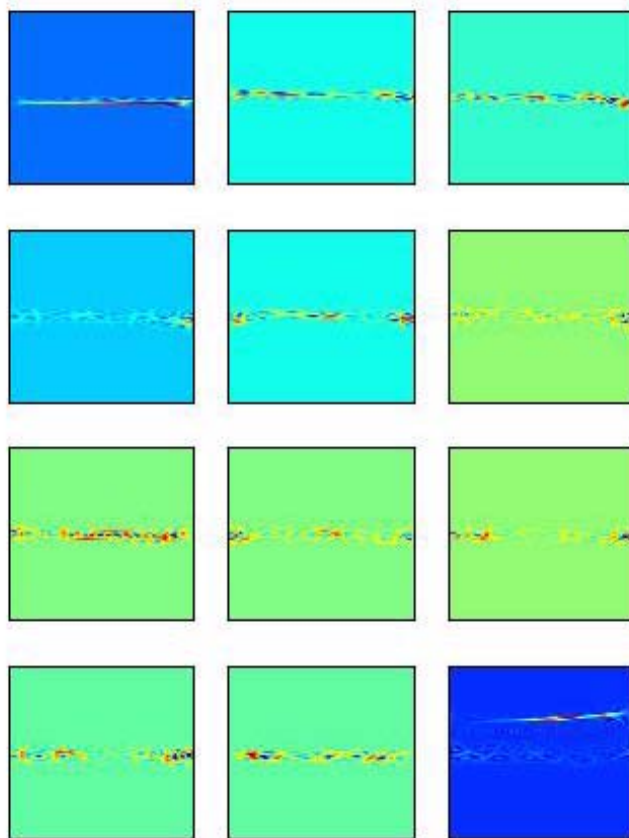


Figure 54: Signal 1 - The frequency representation of the eigenvectors used for the concentration calculation and target detection. In all subplots horizontal axis is for time and vertical axis is for frequency

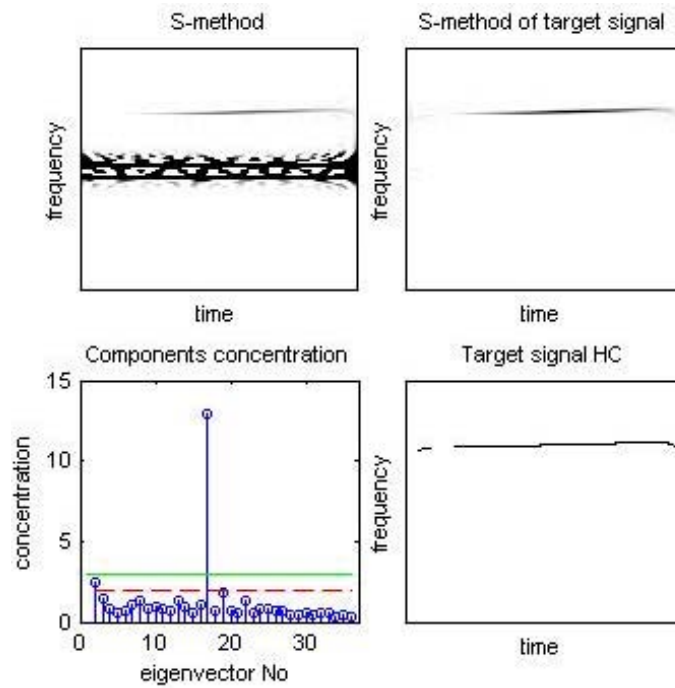


Figure 55: Signal 2 - Concentration of the eigenvectors time-frequency representations (bottom left), Time-frequency representation of the detected target signal (top right), Highly concentrated time-frequency representation of the detected target signal (bottom right)

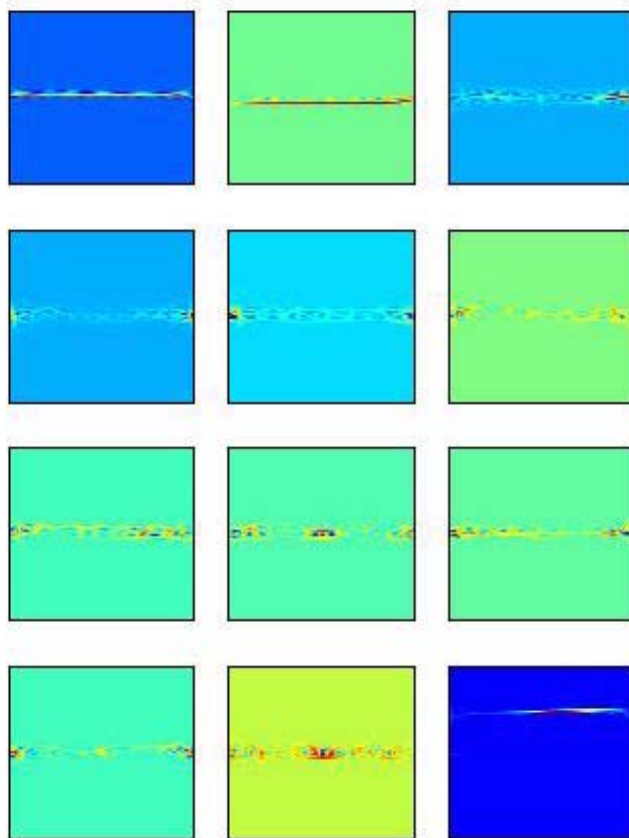


Figure 56: Signal 2 - The frequency representation of the eigenvectors used for the concentration calculation and target detection. In all subplots horizontal axis is for time and vertical axis is for frequency

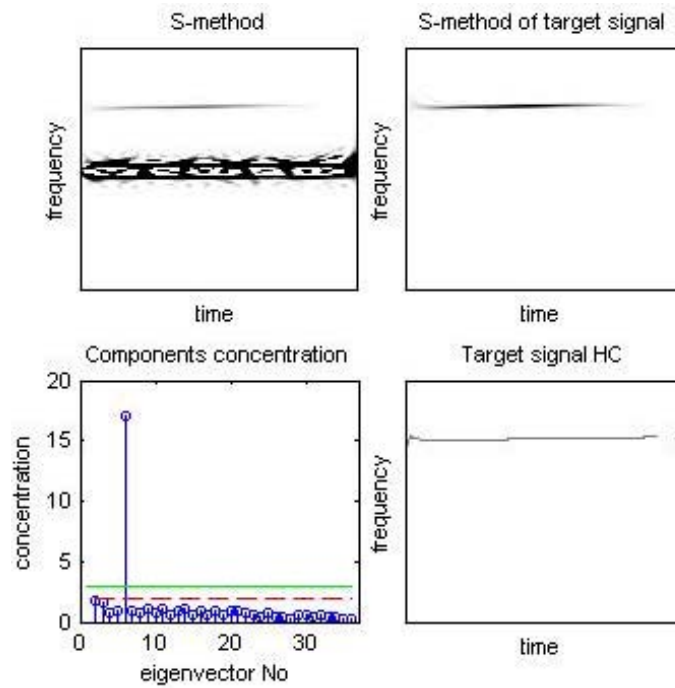


Figure 57: Signal 3 - Concentration of the eigenvectors time-frequency representations (bottom left), Time-frequency representation of the detected target signal (top right), Highly concentrated time-frequency representation of the detected target signal (bottom right)

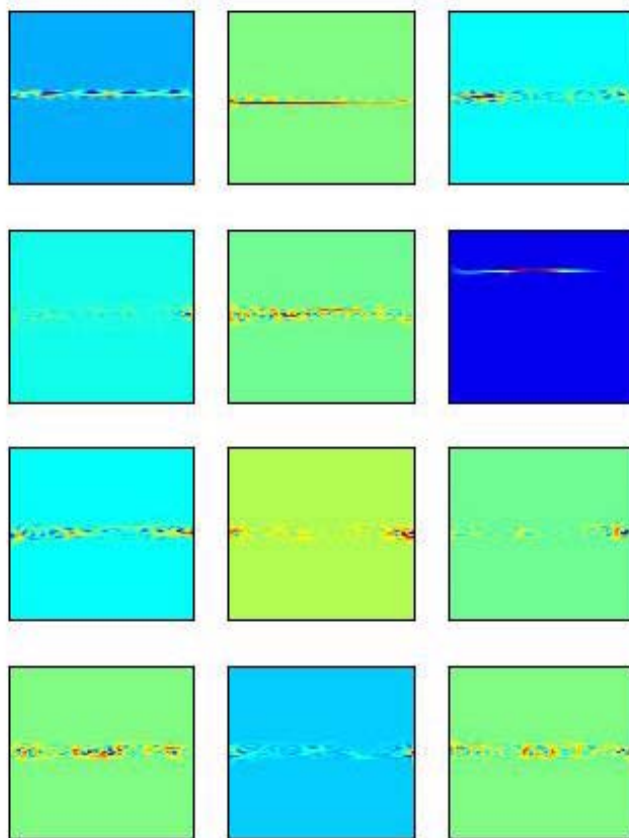


Figure 58: Signal 3 - The frequency representation of the eigenvectors used for the concentration calculation and target detection. In all subplots horizontal axis is for time and vertical axis is for frequency

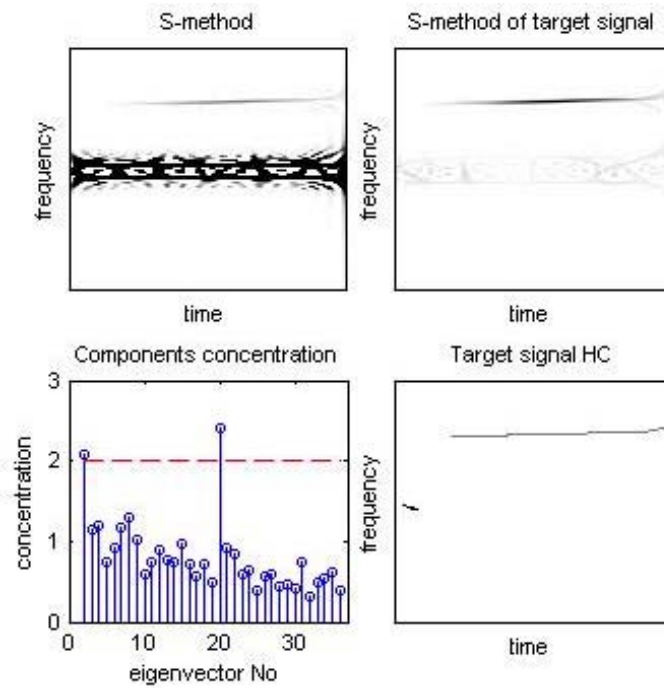


Figure 59: Signal 4 - Concentration of the eigenvectors time-frequency representations (bottom left), Time-frequency representation of the detected target signal (top right), Highly concentrated time-frequency representation of the detected target signal (bottom right)

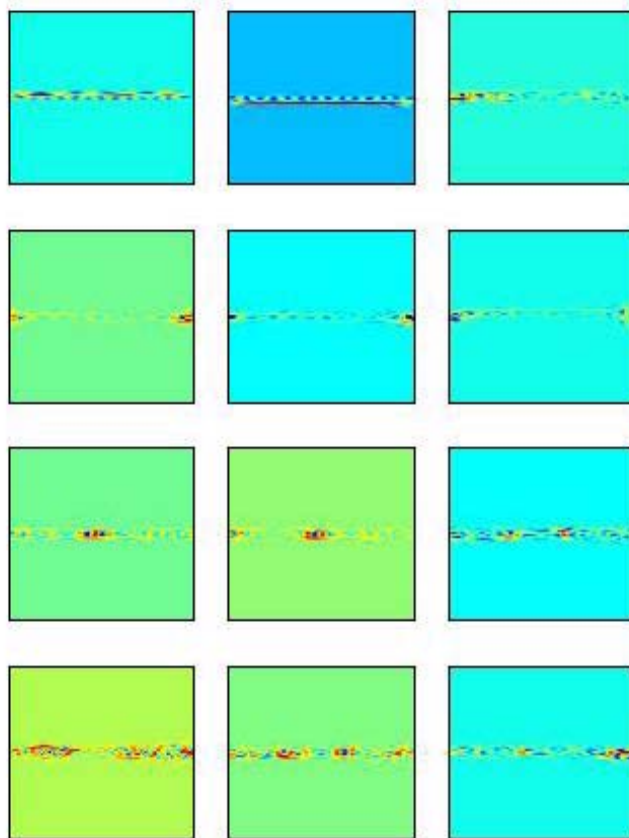


Figure 60: Signal 4 - The frequency representation of the eigenvectors used for the concentration calculation and target detection. In all subplots horizontal axis is for time and vertical axis is for frequency

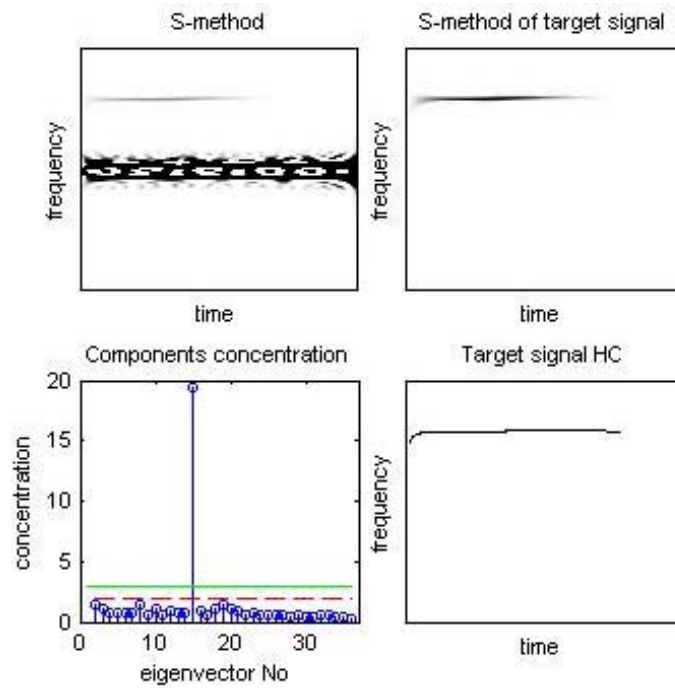


Figure 61: Signal 5 - Concentration of the eigenvectors time-frequency representations (bottom left), Time-frequency representation of the detected target signal (top right), Highly concentrated time-frequency representation of the detected target signal (bottom right)

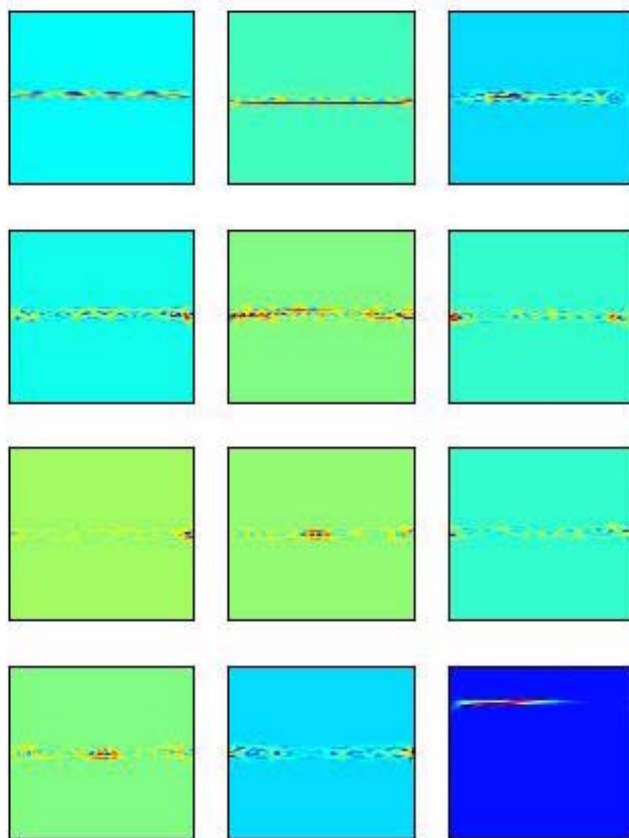


Figure 62: Signal 5 - The frequency representation of the eigenvectors used for the concentration calculation and target detection. In all subplots horizontal axis is for time and vertical axis is for frequency

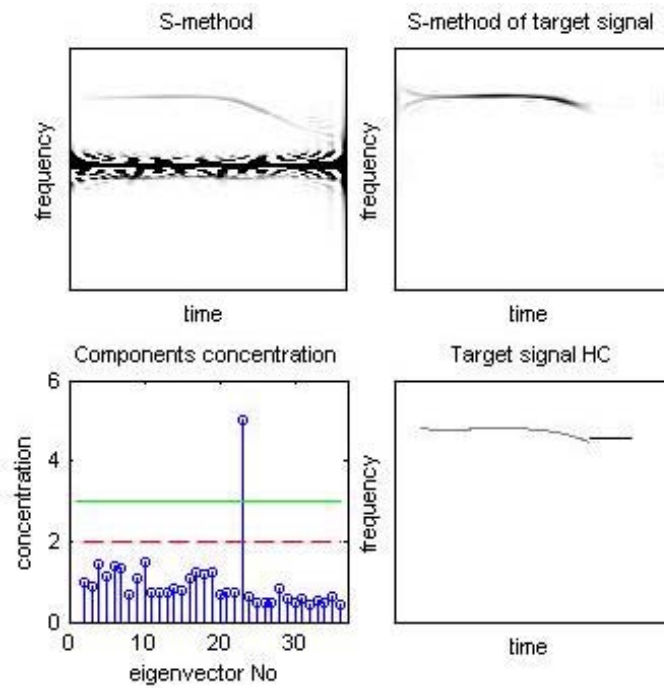


Figure 63: Signal 6 - Concentration of the eigenvectors time-frequency representations (bottom left), Time-frequency representation of the detected target signal (top right), Highly concentrated time-frequency representation of the detected target signal (bottom right)

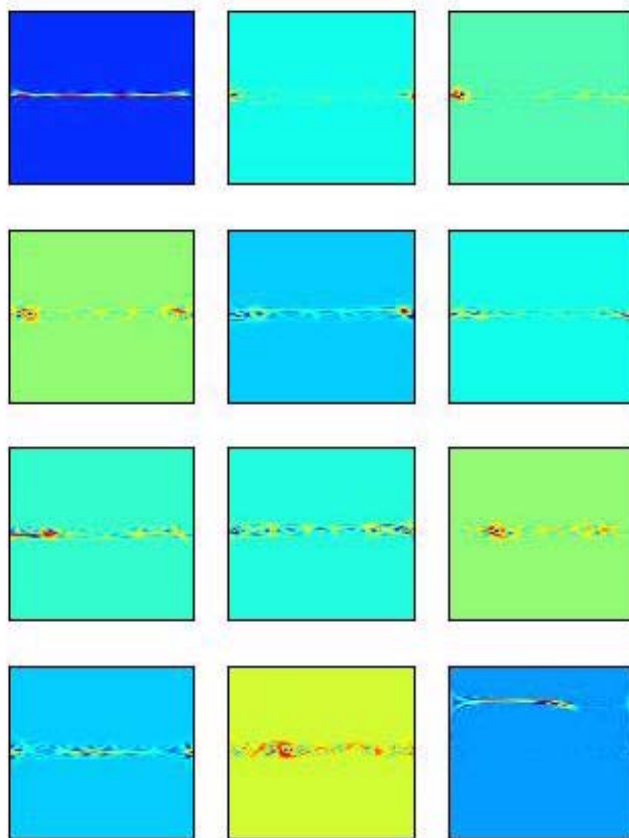


Figure 64: Signal 6 - The frequency representation of the eigenvectors used for the concentration calculation and target detection. In all subplots horizontal axis is for time and vertical axis is for frequency

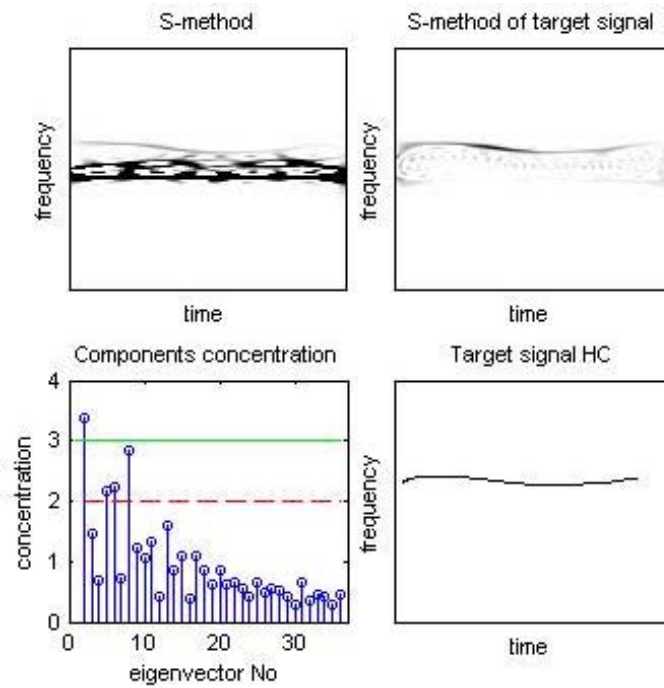


Figure 65: Signal 7 - Concentration of the eigenvectors time-frequency representations (bottom left), Time-frequency representation of the detected target signal (top right), Highly concentrated time-frequency representation of the detected target signal (bottom right)

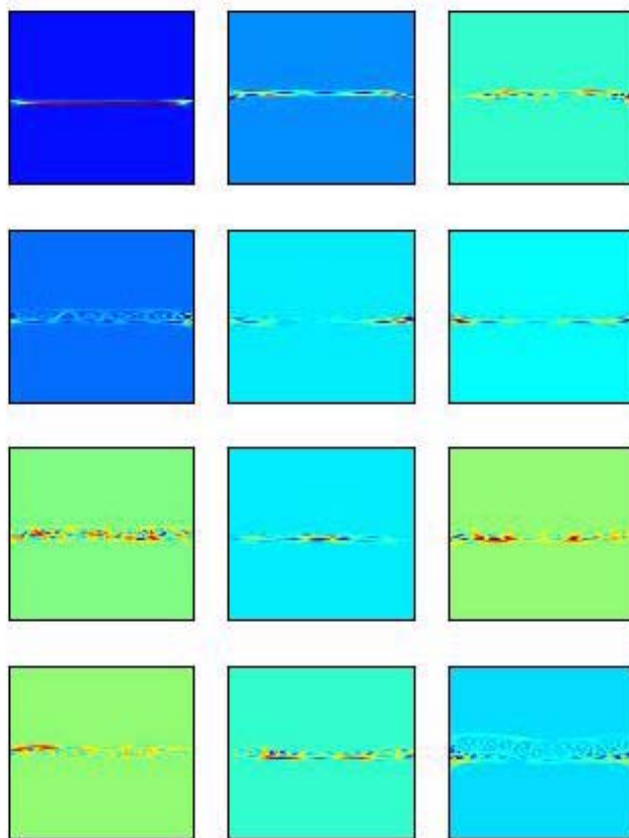


Figure 66: Signal 7 - The frequency representation of the eigenvectors used for the concentration calculation and target detection. In all subplots horizontal axis is for time and vertical axis is for frequency

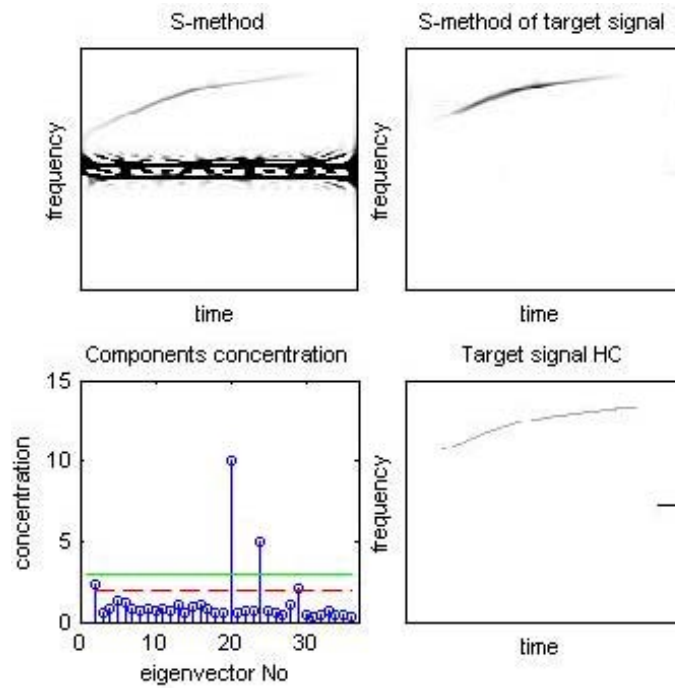


Figure 67: Signal 8 - Concentration of the eigenvectors time-frequency representations (bottom left), Time-frequency representation of the detected target signal (top right), Highly concentrated time-frequency representation of the detected target signal (bottom right)

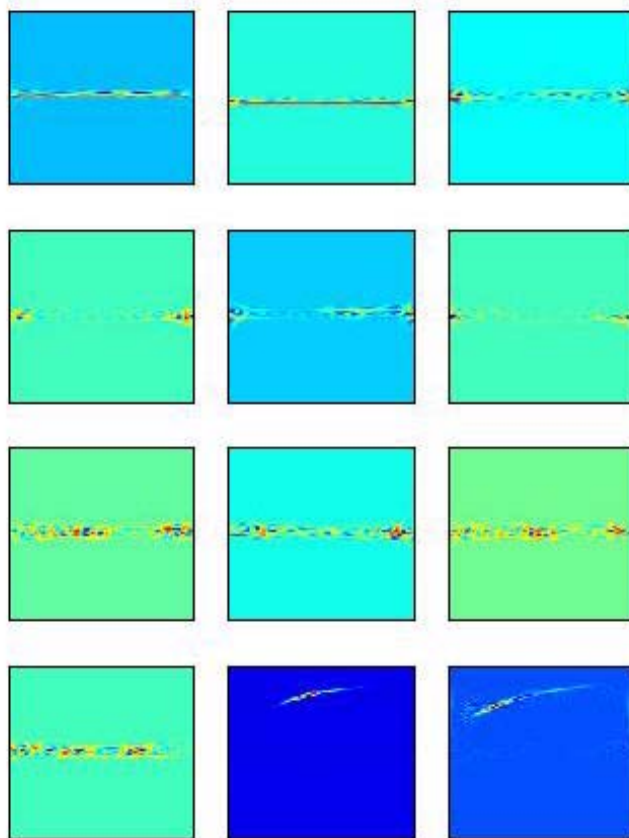


Figure 68: Signal 8 - The frequency representation of the eigenvectors used for the concentration calculation and target detection. In all subplots horizontal axis is for time and vertical axis is for frequency

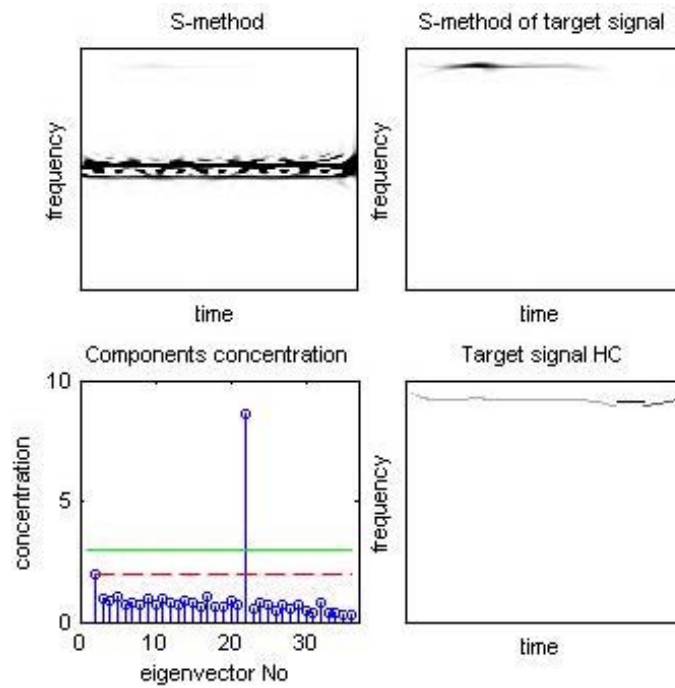


Figure 69: Signal 9 - Concentration of the eigenvectors time-frequency representations (bottom left), Time-frequency representation of the detected target signal (top right), Highly concentrated time-frequency representation of the detected target signal (bottom right)

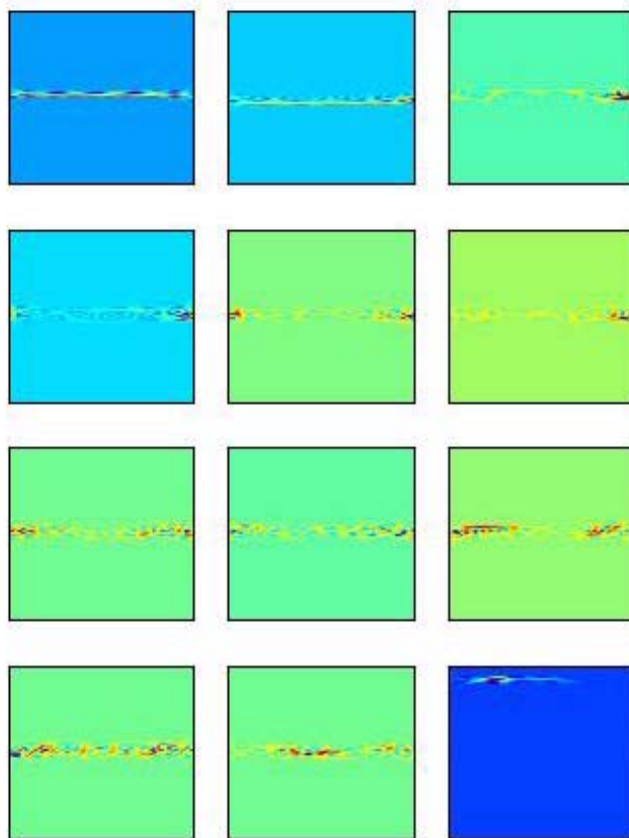


Figure 70: Signal 9 - The frequency representation of the eigenvectors used for the concentration calculation and target detection. In all subplots horizontal axis is for time and vertical axis is for frequency

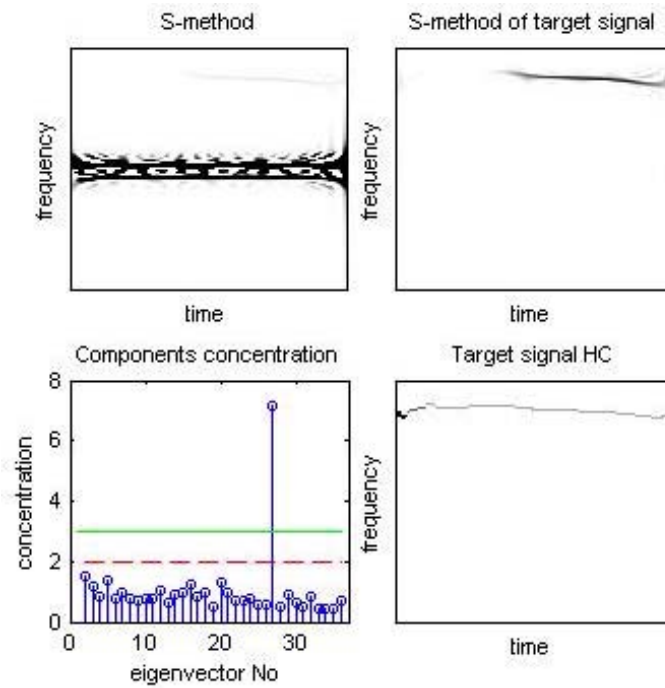


Figure 71: Signal 10 - Concentration of the eigenvectors time-frequency representations (bottom left), Time-frequency representation of the detected target signal (top right), Highly concentrated time-frequency representation of the detected target signal (bottom right)

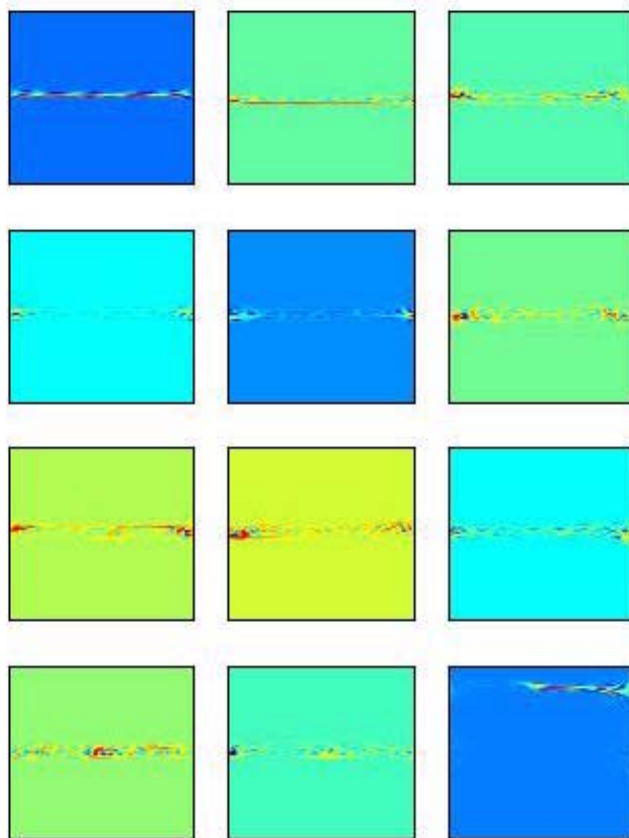


Figure 72: Signal 10 - The frequency representation of the eigenvectors used for the concentration calculation and target detection. In all subplots horizontal axis is for time and vertical axis is for frequency

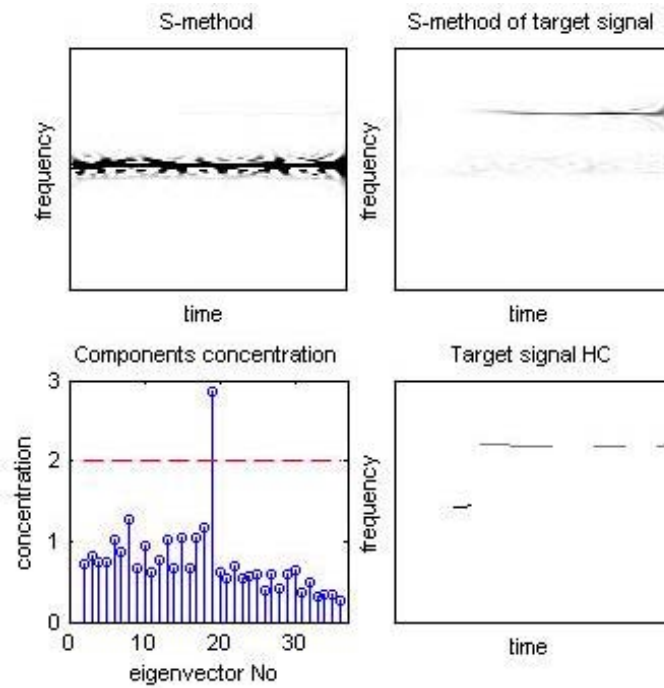


Figure 73: Signal 11 - Concentration of the eigenvectors time-frequency representations (bottom left), Time-frequency representation of the detected target signal (top right), Highly concentrated time-frequency representation of the detected target signal (bottom right)

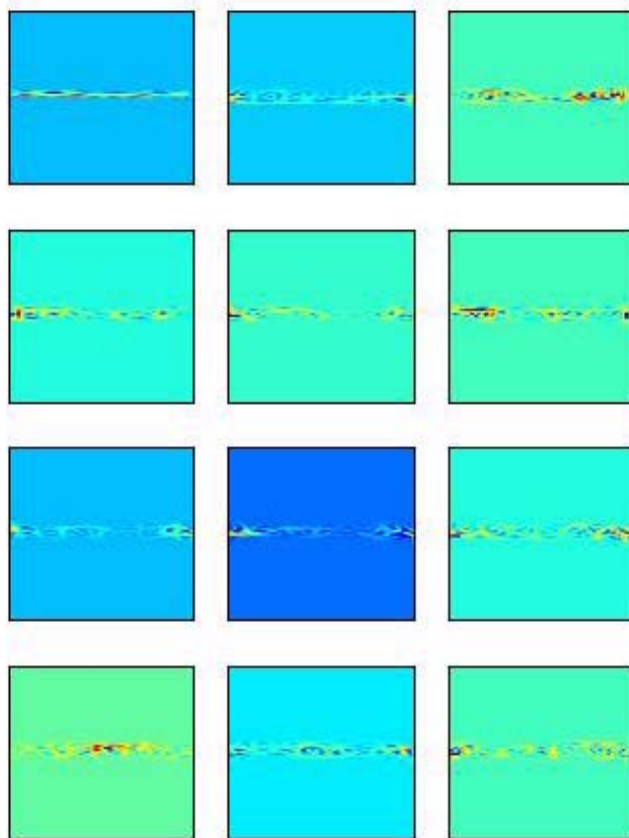


Figure 74: Signal 11 - The frequency representation of the eigenvectors used for the concentration calculation and target detection. In all subplots horizontal axis is for time and vertical axis is for frequency

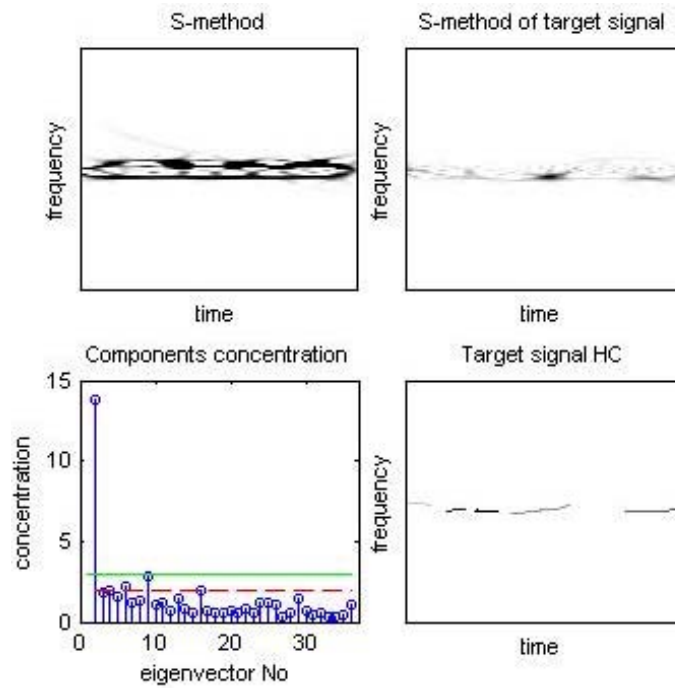


Figure 75: Signal 12 - Concentration of the eigenvectors time-frequency representations (bottom left), Time-frequency representation of the detected target signal (top right), Highly concentrated time-frequency representation of the detected target signal (bottom right)

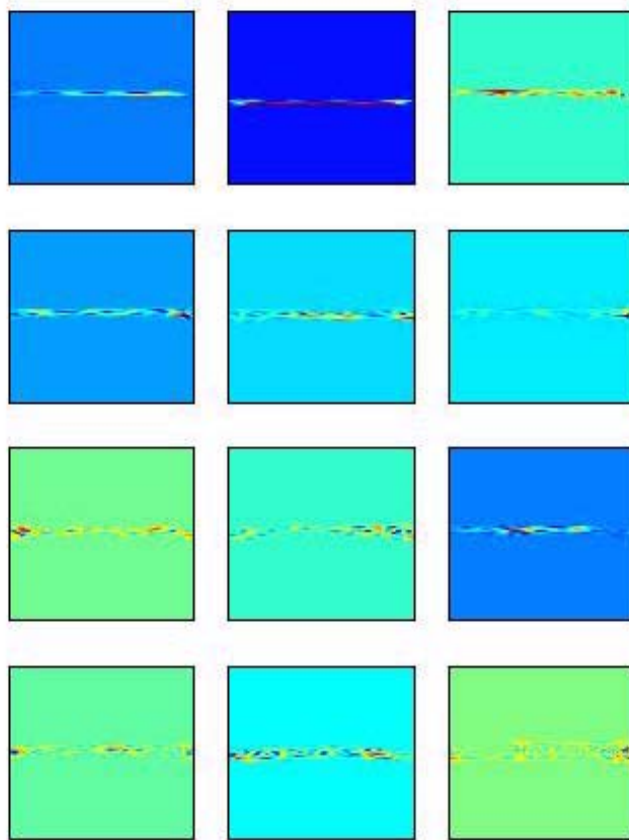


Figure 76: Signal 12 - The frequency representation of the eigenvectors used for the concentration calculation and target detection. In all subplots horizontal axis is for time and vertical axis is for frequency

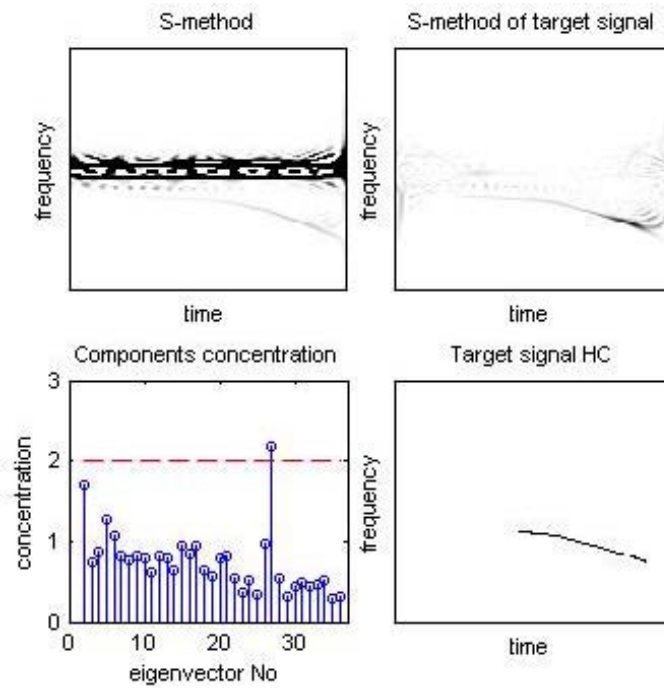


Figure 77: Signal 13 - Concentration of the eigenvectors time-frequency representations (bottom left), Time-frequency representation of the detected target signal (top right), Highly concentrated time-frequency representation of the detected target signal (bottom right)

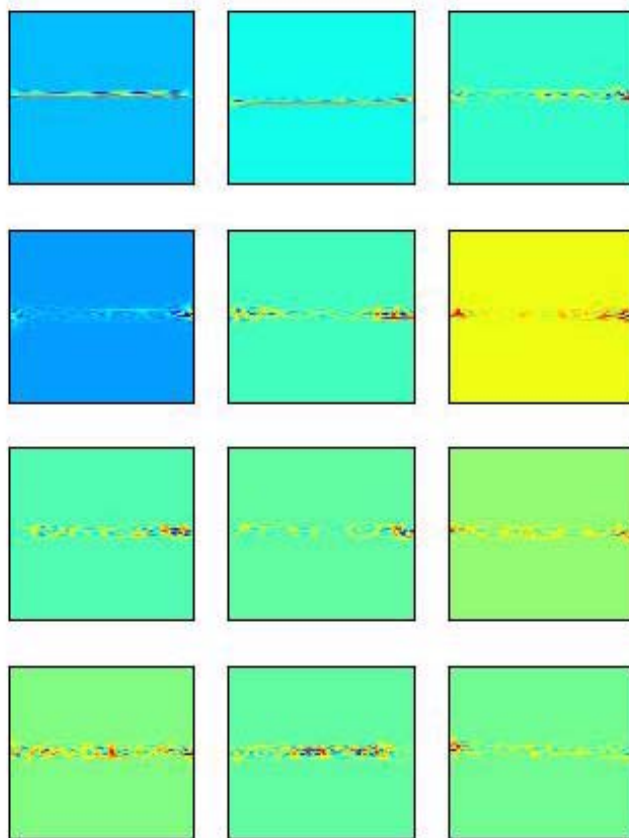


Figure 78: Signal 13 - The frequency representation of the eigenvectors used for the concentration calculation and target detection. In all subplots horizontal axis is for time and vertical axis is for frequency

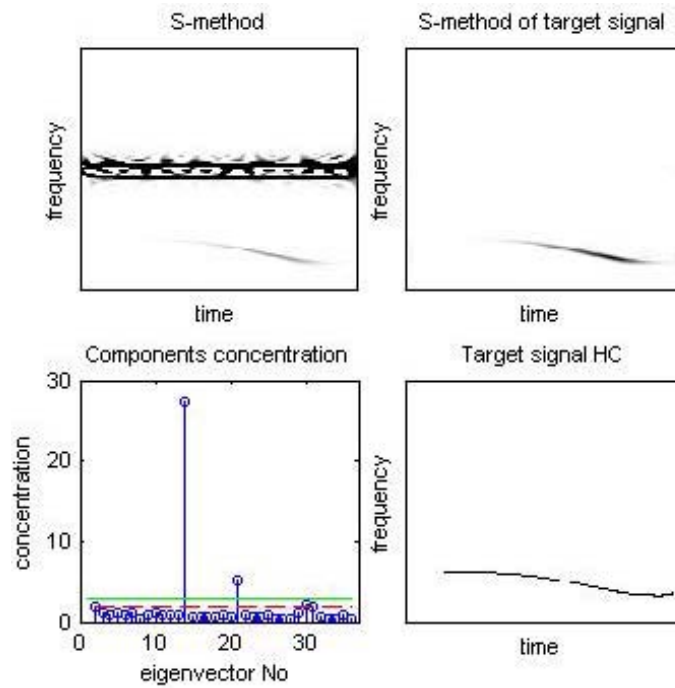


Figure 79: Signal 14 - Concentration of the eigenvectors time-frequency representations (bottom left), Time-frequency representation of the detected target signal (top right), Highly concentrated time-frequency representation of the detected target signal (bottom right)

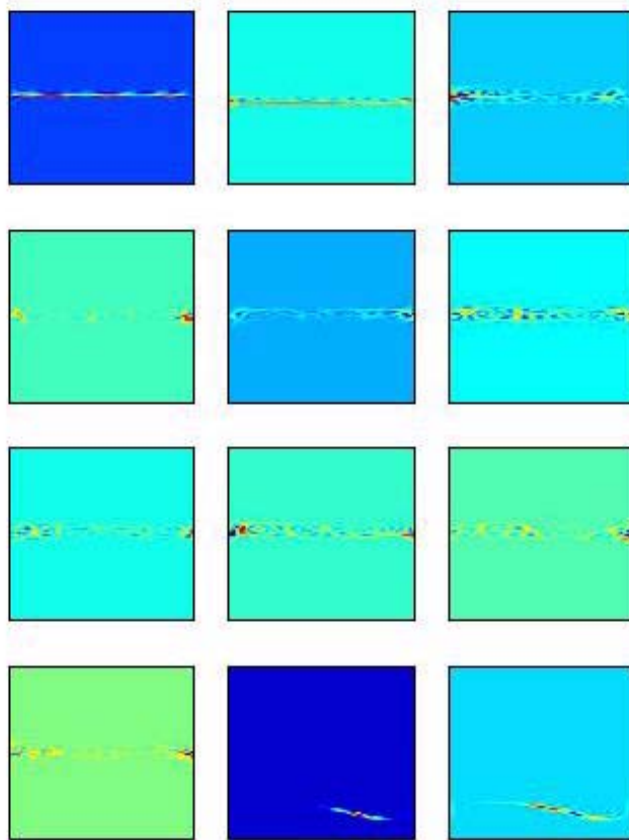


Figure 80: Signal 14 - The frequency representation of the eigenvectors used for the concentration calculation and target detection. In all subplots horizontal axis is for time and vertical axis is for frequency

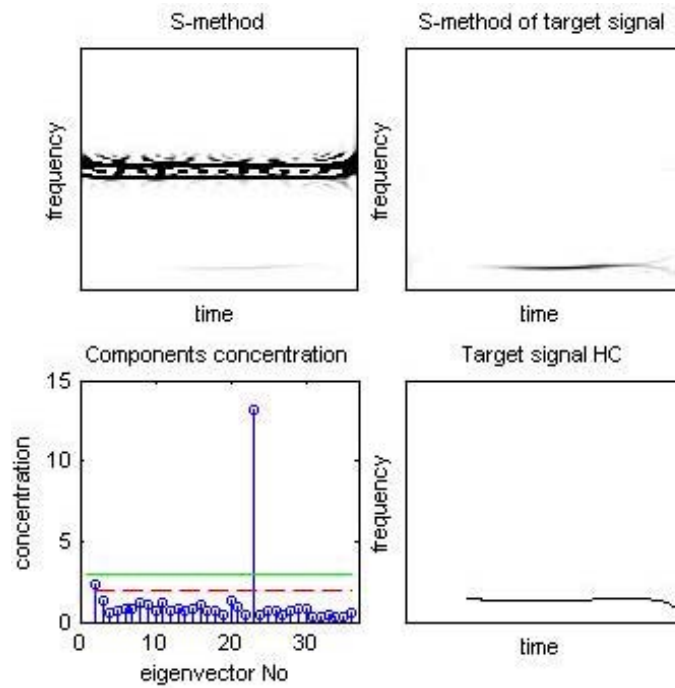


Figure 81: Signal 15 - Concentration of the eigenvectors time-frequency representations (bottom left), Time-frequency representation of the detected target signal (top right), Highly concentrated time-frequency representation of the detected target signal (bottom right)

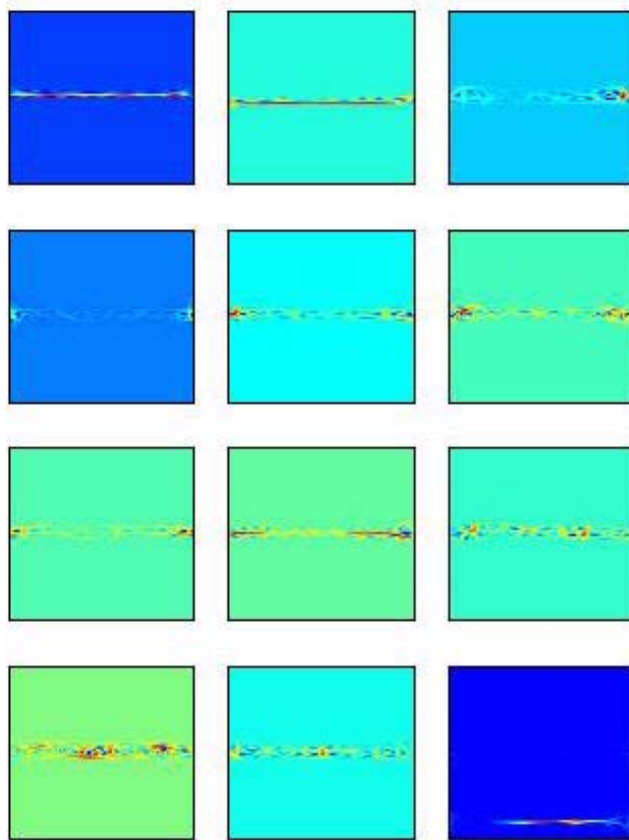


Figure 82: Signal 15 - The frequency representation of the eigenvectors used for the concentration calculation and target detection. In all subplots horizontal axis is for time and vertical axis is for frequency

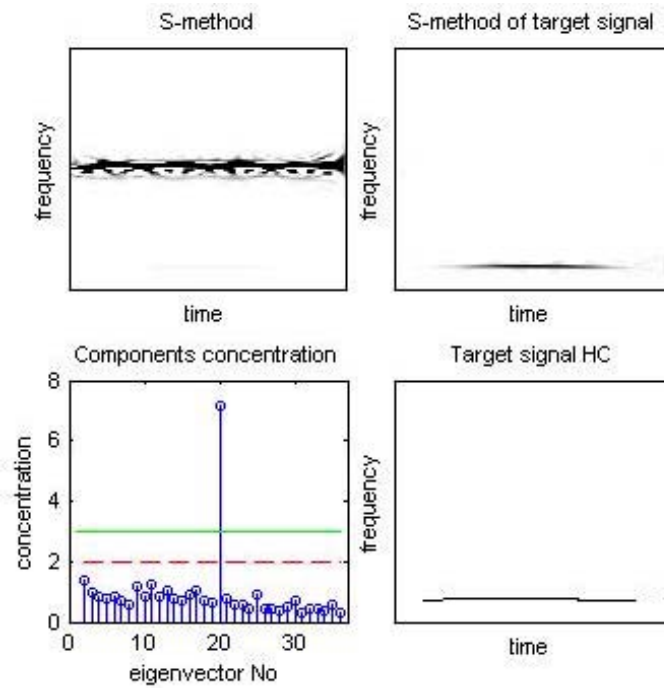


Figure 83: Signal 16 - Concentration of the eigenvectors time-frequency representations (bottom left), Time-frequency representation of the detected target signal (top right), Highly concentrated time-frequency representation of the detected target signal (bottom right)

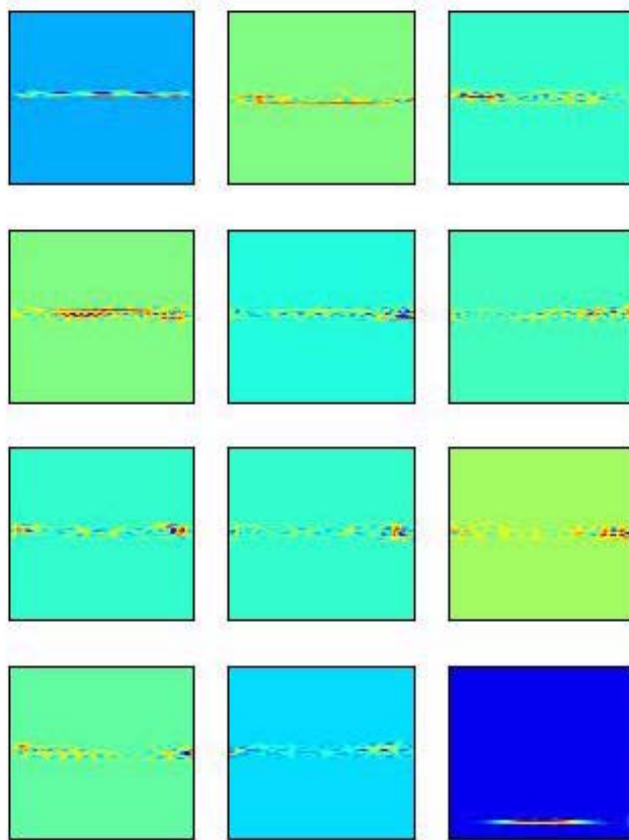


Figure 84: Signal 16 - The frequency representation of the eigenvectors used for the concentration calculation and target detection. In all subplots horizontal axis is for time and vertical axis is for frequency

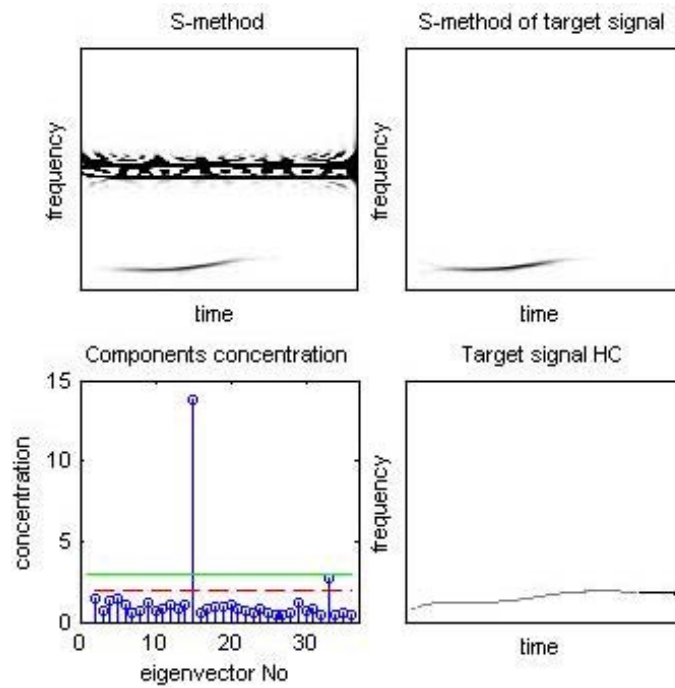


Figure 85: Signal 17 - Concentration of the eigenvectors time-frequency representations (bottom left), Time-frequency representation of the detected target signal (top right), Highly concentrated time-frequency representation of the detected target signal (bottom right)

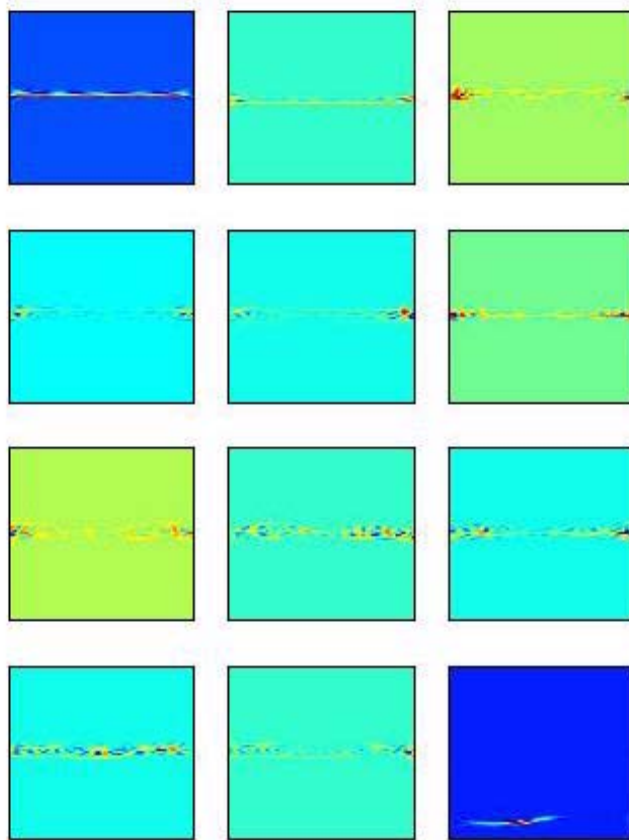


Figure 86: Signal 17 - The frequency representation of the eigenvectors used for the concentration calculation and target detection. In all subplots horizontal axis is for time and vertical axis is for frequency

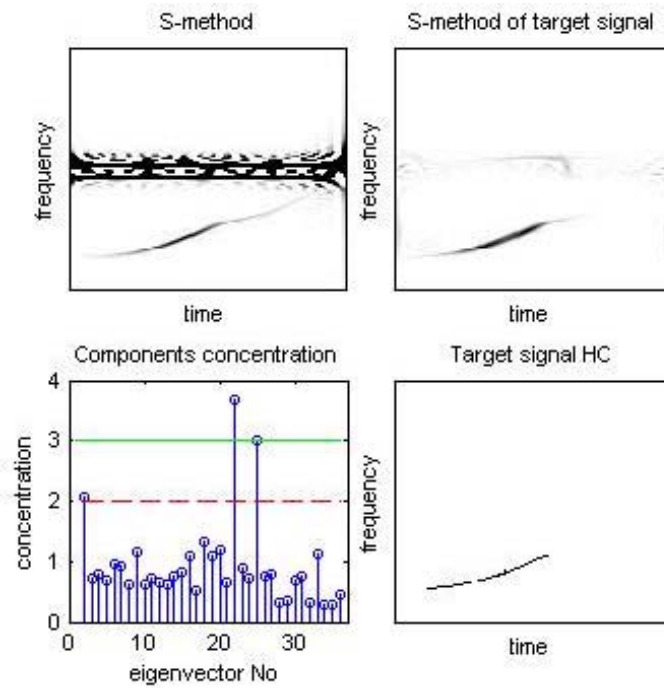


Figure 87: Signal 18 - Concentration of the eigenvectors time-frequency representations (bottom left), Time-frequency representation of the detected target signal (top right), Highly concentrated time-frequency representation of the detected target signal (bottom right)

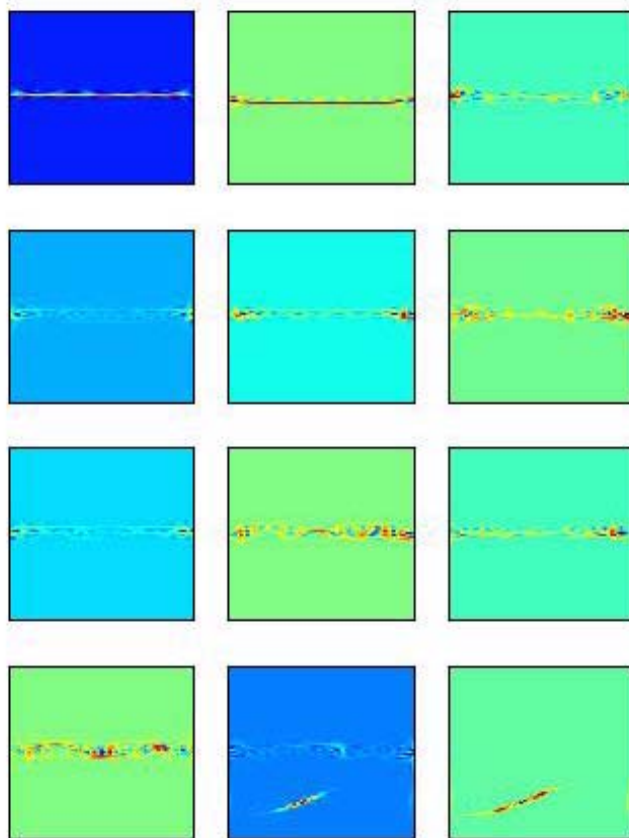


Figure 88: Signal 18 - The frequency representation of the eigenvectors used for the concentration calculation and target detection. In all subplots horizontal axis is for time and vertical axis is for frequency

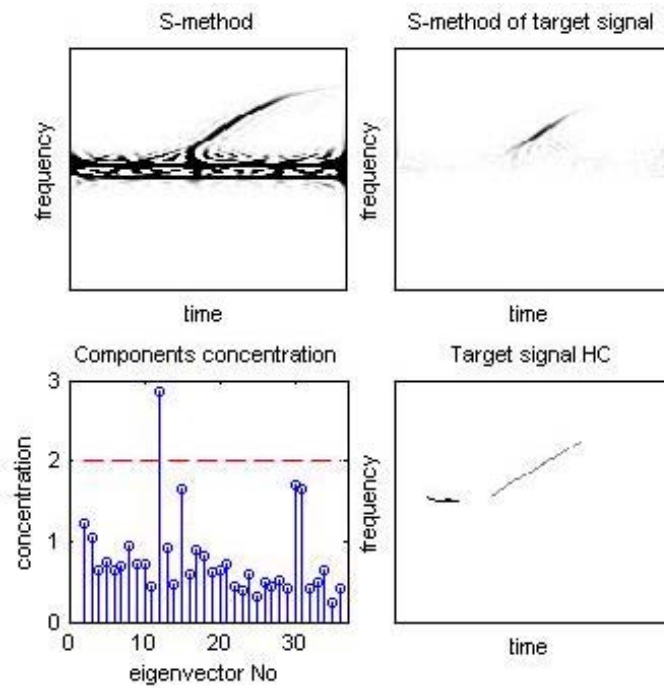


Figure 89: Signal 19 - Concentration of the eigenvectors time-frequency representations (bottom left), Time-frequency representation of the detected target signal (top right), Highly concentrated time-frequency representation of the detected target signal (bottom right)

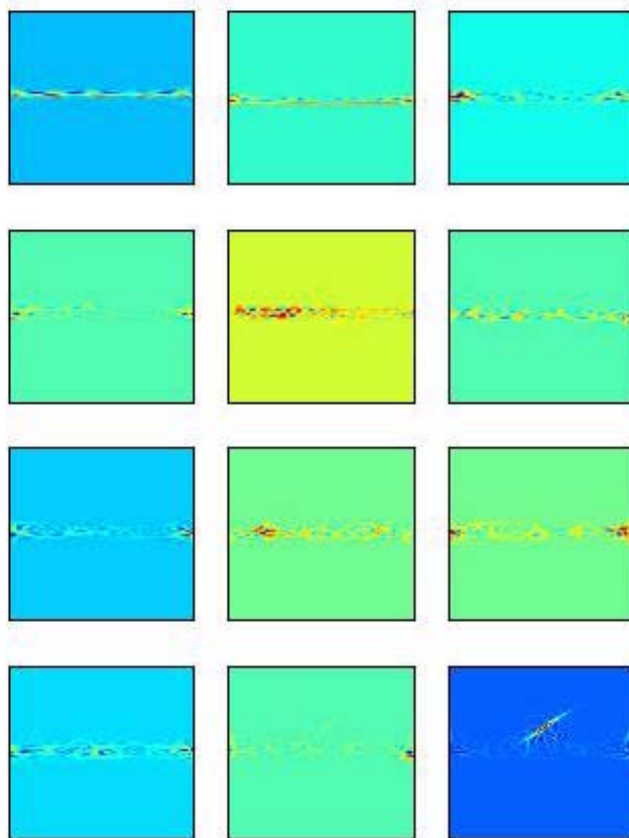


Figure 90: Signal 19 - The frequency representation of the eigenvectors used for the concentration calculation and target detection. In all subplots horizontal axis is for time and vertical axis is for frequency

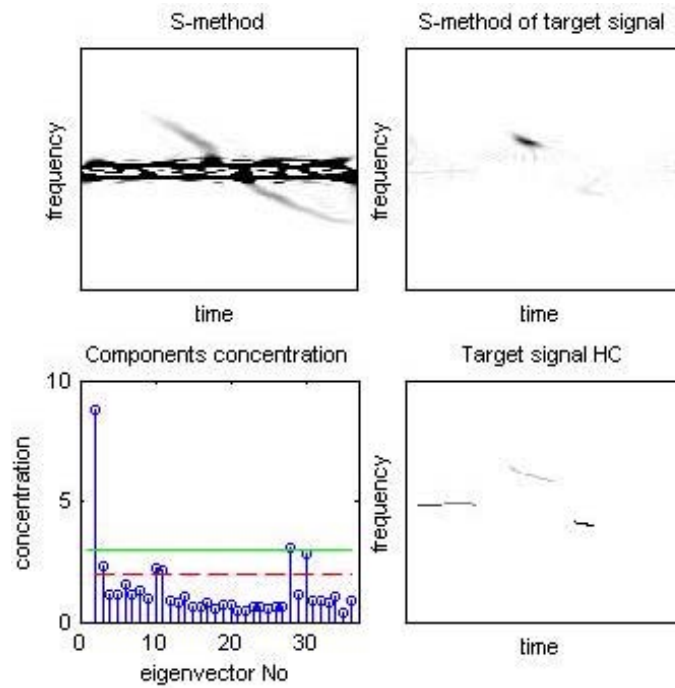


Figure 91: Signal 20 - Concentration of the eigenvectors time-frequency representations (bottom left), Time-frequency representation of the detected target signal (top right), Highly concentrated time-frequency representation of the detected target signal (bottom right)

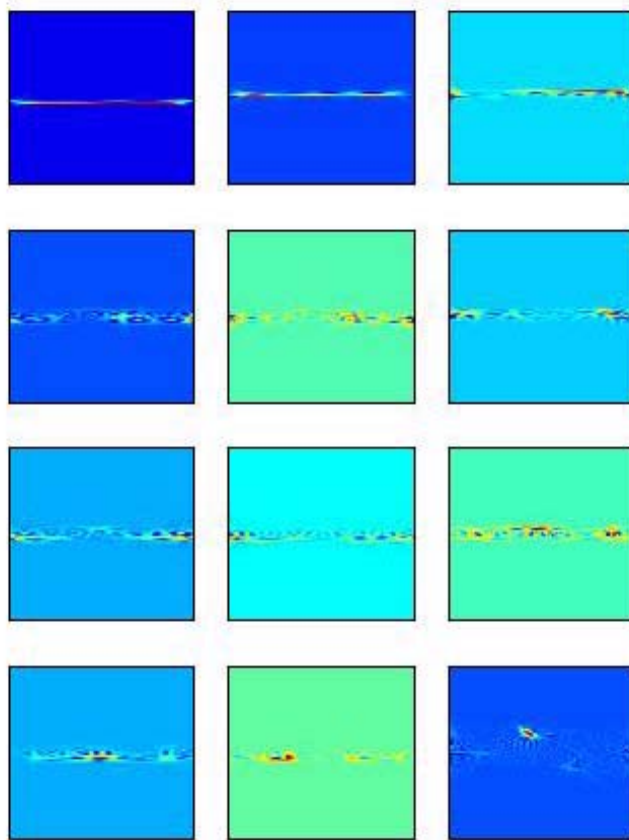


Figure 92: Signal 20 - The frequency representation of the eigenvectors used for the concentration calculation and target detection. In all subplots horizontal axis is for time and vertical axis is for frequency

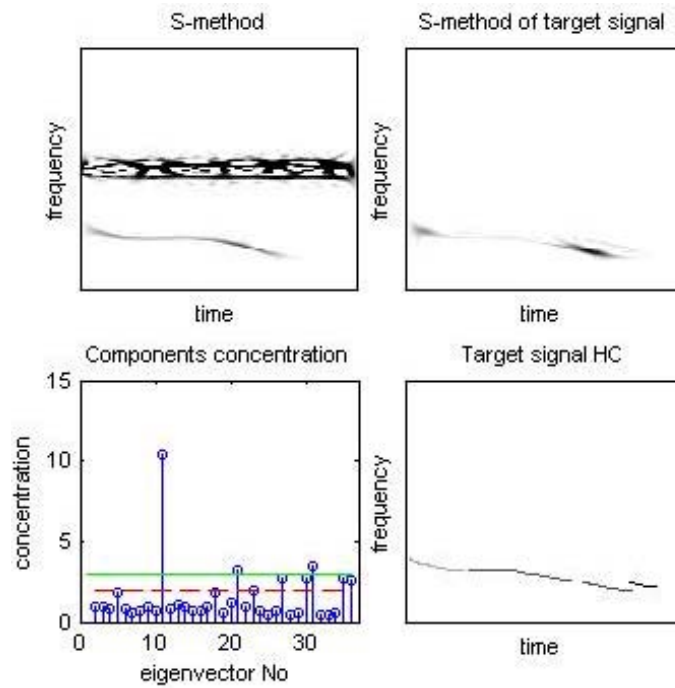


Figure 93: Signal 21 - Concentration of the eigenvectors time-frequency representations (bottom left), Time-frequency representation of the detected target signal (top right), Highly concentrated time-frequency representation of the detected target signal (bottom right)

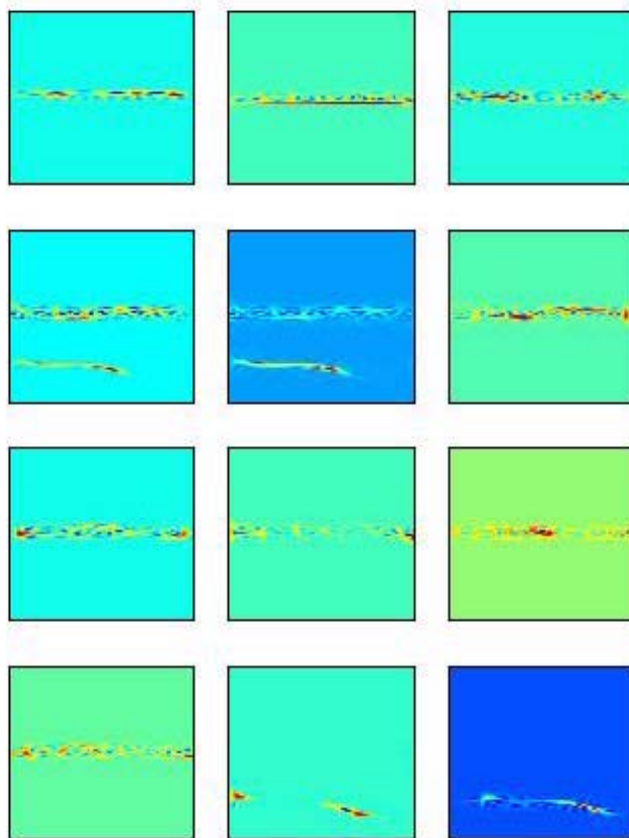


Figure 94: Signal 21 - The frequency representation of the eigenvectors used for the concentration calculation and target detection. In all subplots horizontal axis is for time and vertical axis is for frequency

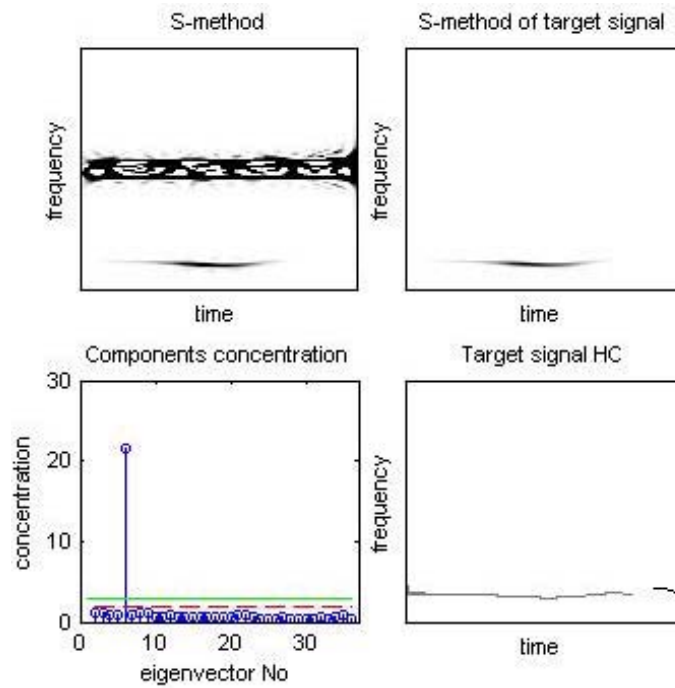


Figure 95: Signal 22 - Concentration of the eigenvectors time-frequency representations (bottom left), Time-frequency representation of the detected target signal (top right), Highly concentrated time-frequency representation of the detected target signal (bottom right)

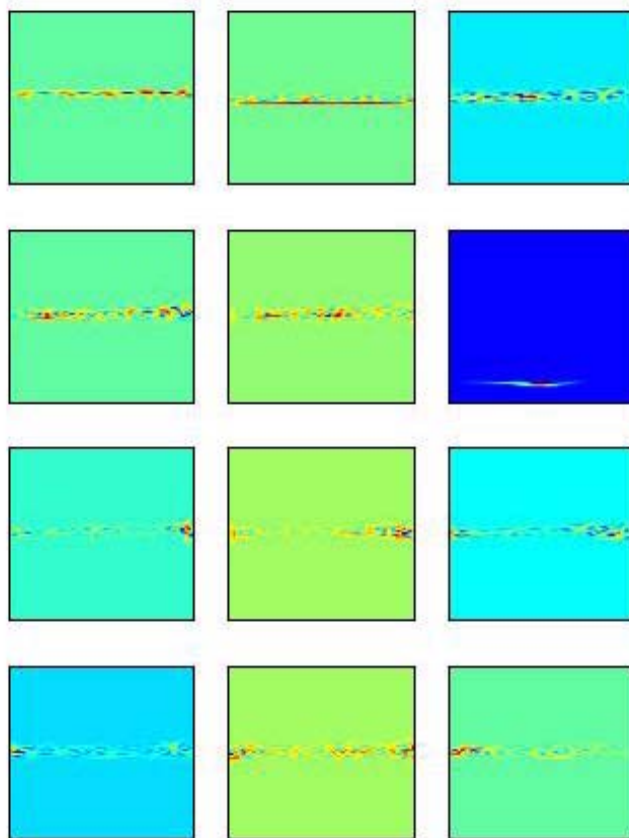


Figure 96: Signal 22 - The frequency representation of the eigenvectors used for the concentration calculation and target detection. In all subplots horizontal axis is for time and vertical axis is for frequency

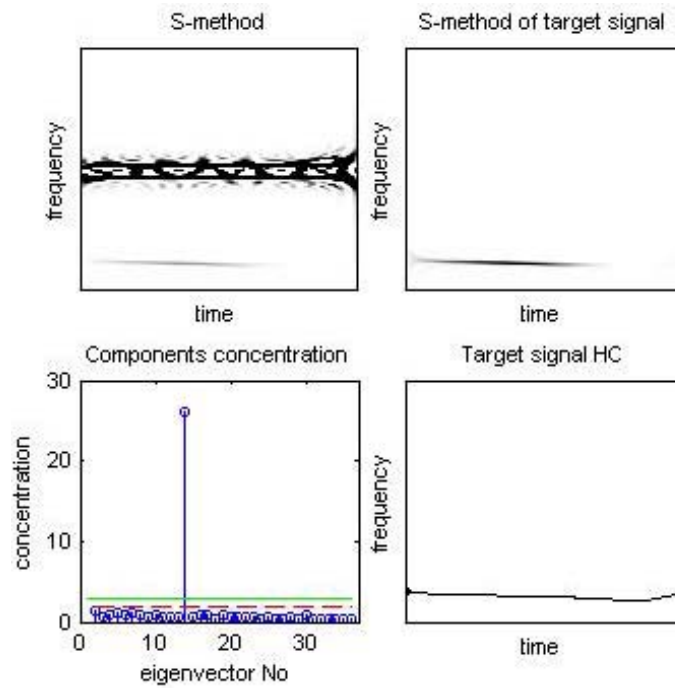


Figure 97: Signal 23 - Concentration of the eigenvectors time-frequency representations (bottom left), Time-frequency representation of the detected target signal (top right), Highly concentrated time-frequency representation of the detected target signal (bottom right)

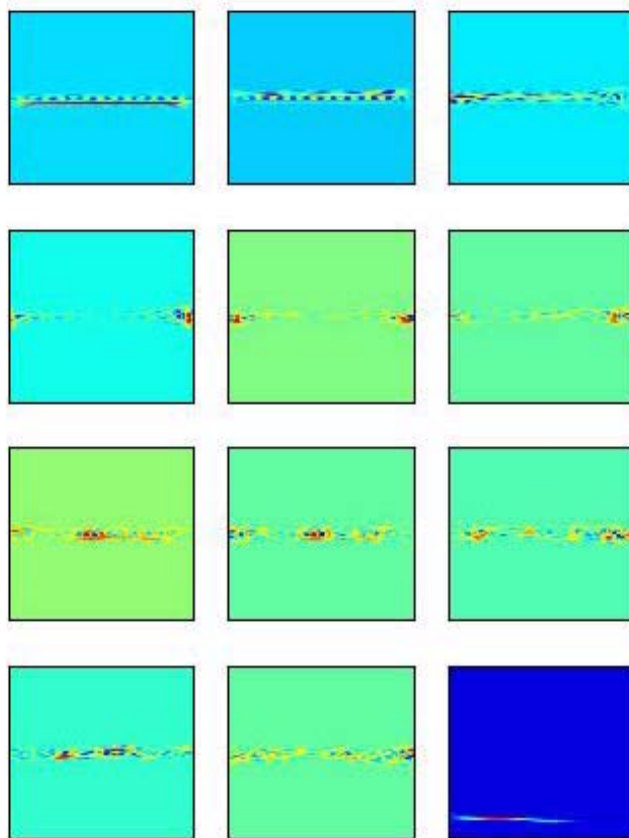


Figure 98: Signal 23 - The frequency representation of the eigenvectors used for the concentration calculation and target detection. In all subplots horizontal axis is for time and vertical axis is for frequency

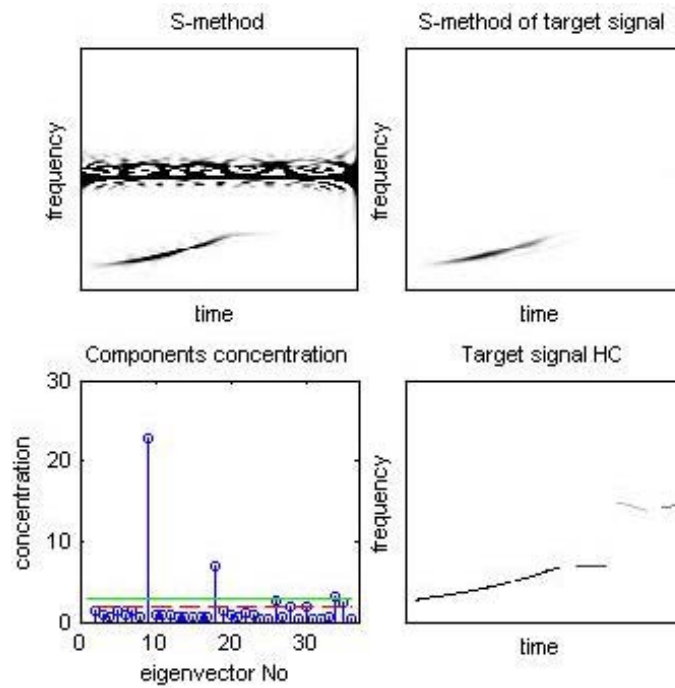


Figure 99: Signal 24 - Concentration of the eigenvectors time-frequency representations (bottom left), Time-frequency representation of the detected target signal (top right), Highly concentrated time-frequency representation of the detected target signal (bottom right)

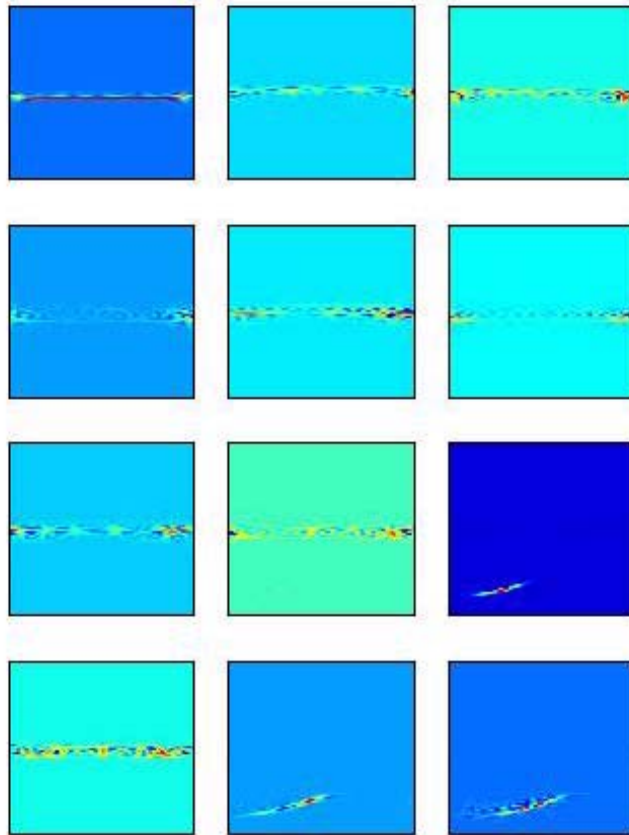


Figure 100: Signal 24 - The frequency representation of the eigenvectors used for the concentration calculation and target detection. In all subplots horizontal axis is for time and vertical axis is for frequency

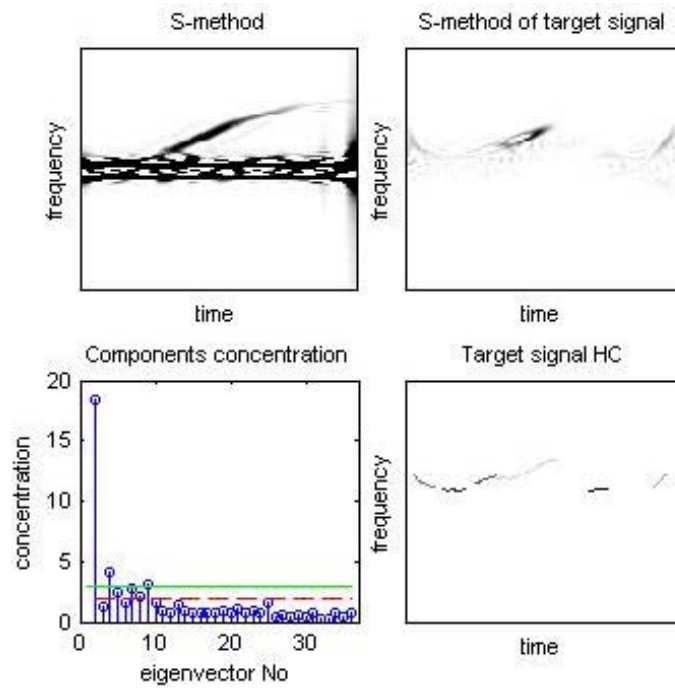


Figure 101: Signal 25 - Concentration of the eigenvectors time-frequency representations (bottom left), Time-frequency representation of the detected target signal (top right), Highly concentrated time-frequency representation of the detected target signal (bottom right)

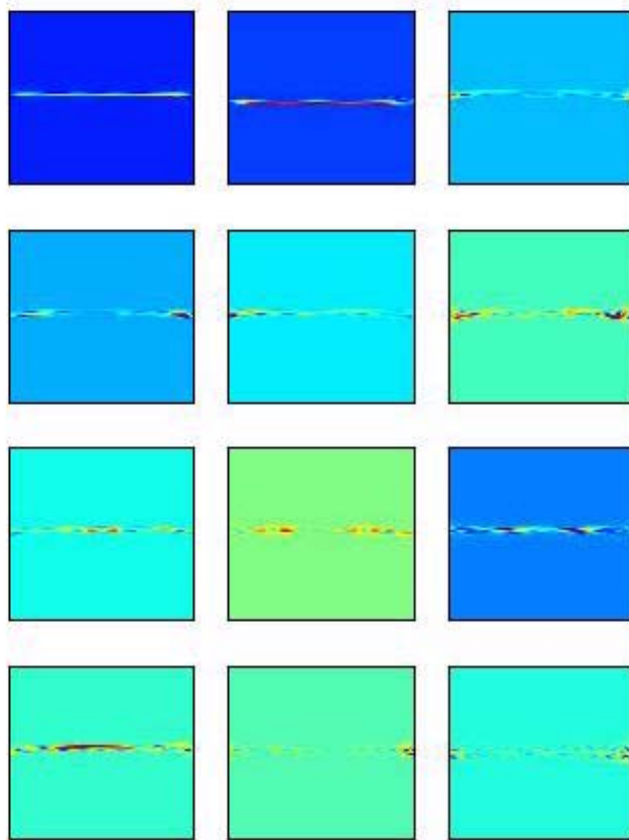


Figure 102: Signal 25 - The frequency representation of the eigenvectors used for the concentration calculation and target detection. In all subplots horizontal axis is for time and vertical axis is for frequency

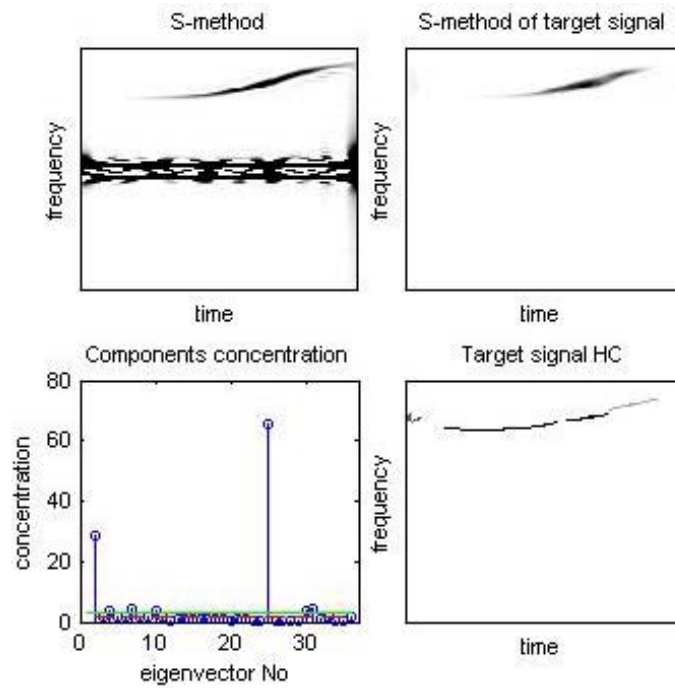


Figure 103: Signal 26 - Concentration of the eigenvectors time-frequency representations (bottom left), Time-frequency representation of the detected target signal (top right), Highly concentrated time-frequency representation of the detected target signal (bottom right)

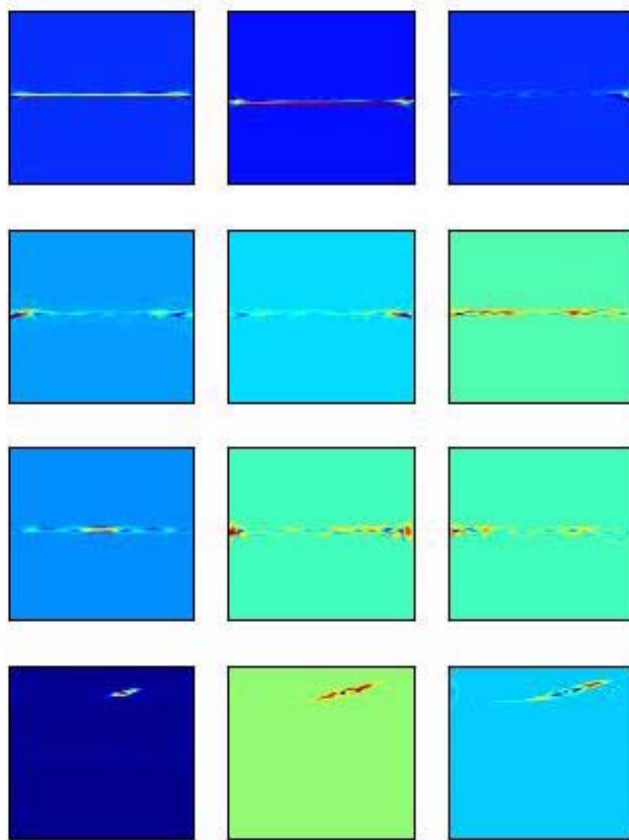


Figure 104: Signal 26 - The frequency representation of the eigenvectors used for the concentration calculation and target detection. In all subplots horizontal axis is for time and vertical axis is for frequency

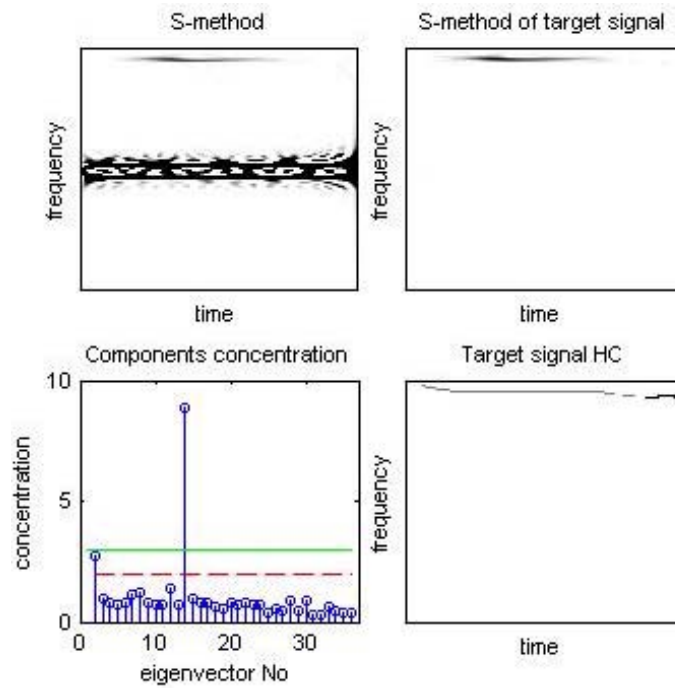


Figure 105: Signal 27 - Concentration of the eigenvectors time-frequency representations (bottom left), Time-frequency representation of the detected target signal (top right), Highly concentrated time-frequency representation of the detected target signal (bottom right)

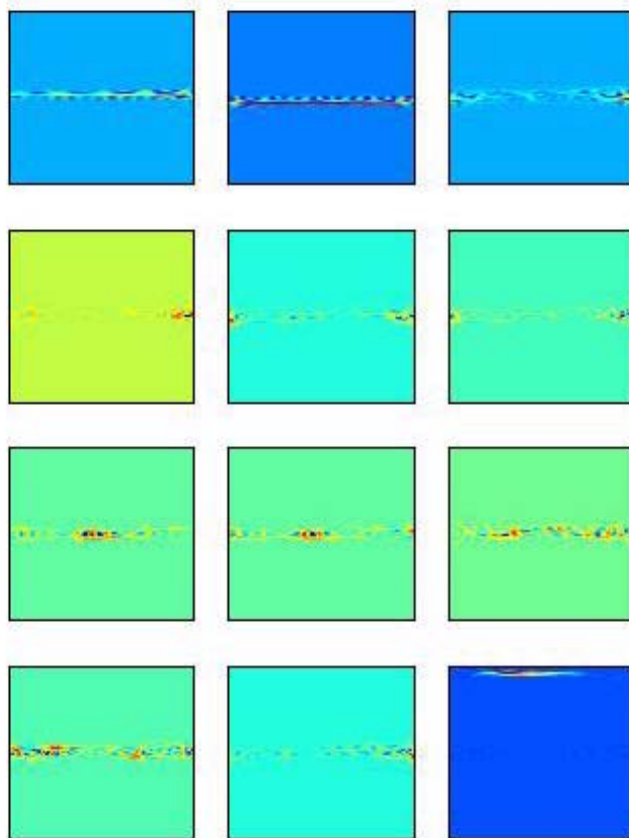


Figure 106: Signal 27 - The frequency representation of the eigenvectors used for the concentration calculation and target detection. In all subplots horizontal axis is for time and vertical axis is for frequency

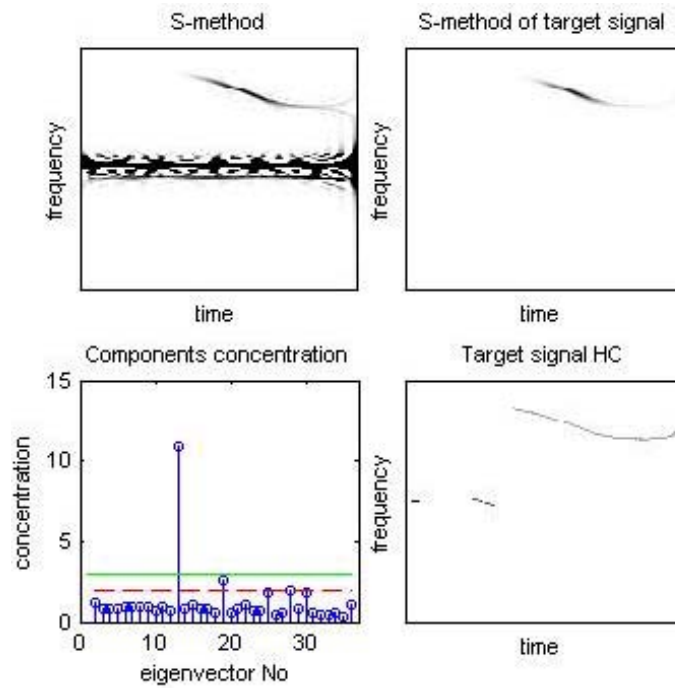


Figure 107: Signal 28 - Concentration of the eigenvectors time-frequency representations (bottom left), Time-frequency representation of the detected target signal (top right), Highly concentrated time-frequency representation of the detected target signal (bottom right)

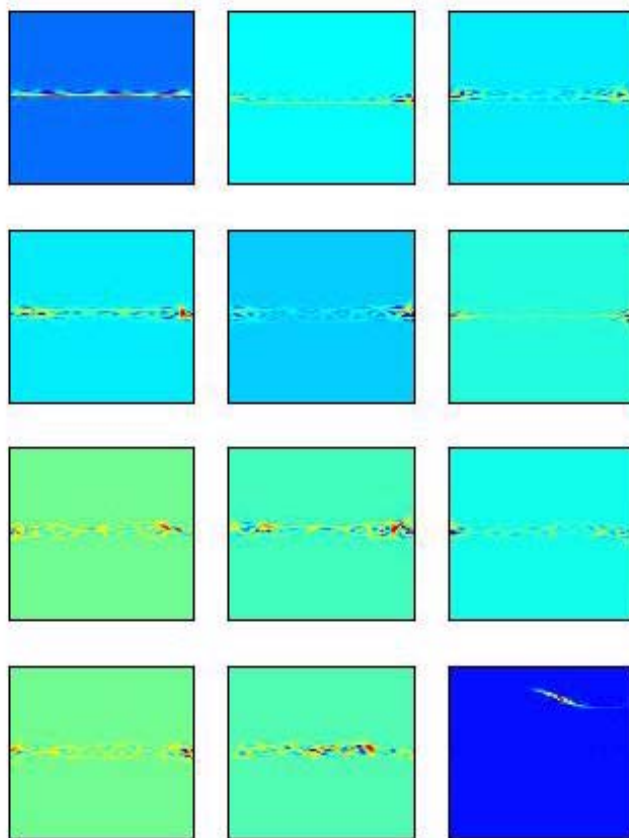


Figure 108: Signal 28 - The frequency representation of the eigenvectors used for the concentration calculation and target detection. In all subplots horizontal axis is for time and vertical axis is for frequency

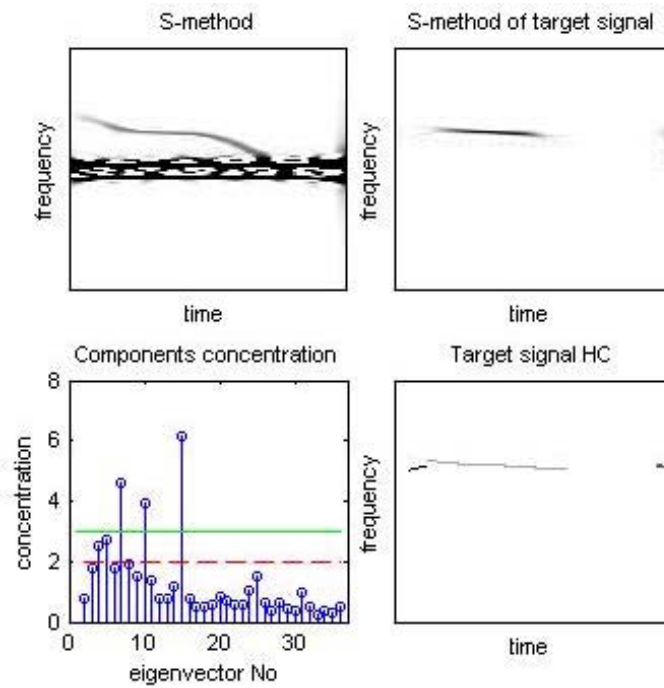


Figure 109: Signal 29 - Concentration of the eigenvectors time-frequency representations (bottom left), Time-frequency representation of the detected target signal (top right), Highly concentrated time-frequency representation of the detected target signal (bottom right)

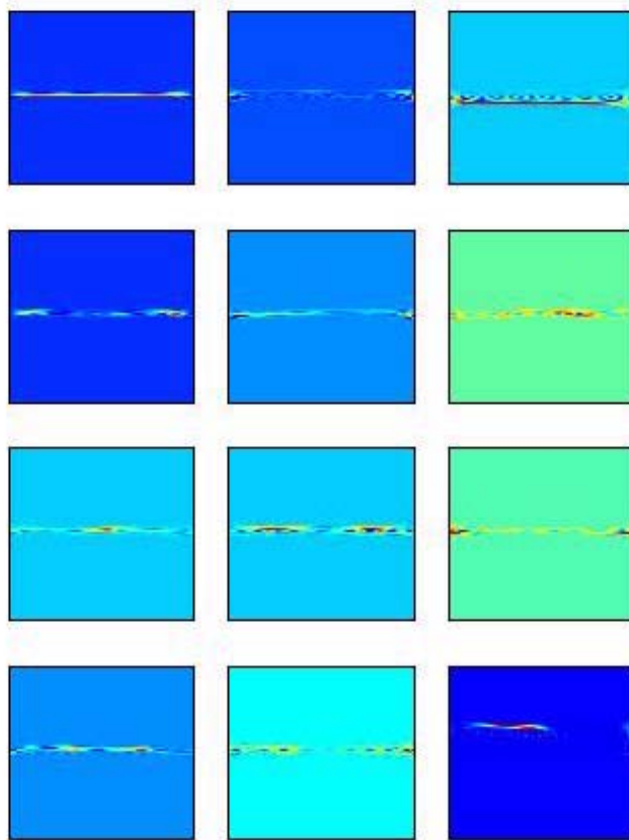


Figure 110: Signal 29 - The frequency representation of the eigenvectors used for the concentration calculation and target detection. In all subplots horizontal axis is for time and vertical axis is for frequency

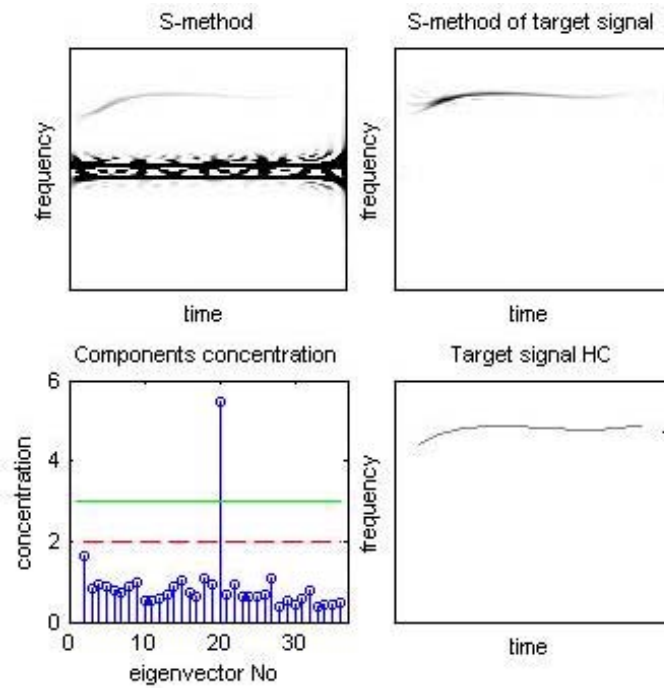


Figure 111: Signal 30 - Concentration of the eigenvectors time-frequency representations (bottom left), Time-frequency representation of the detected target signal (top right), Highly concentrated time-frequency representation of the detected target signal (bottom right)

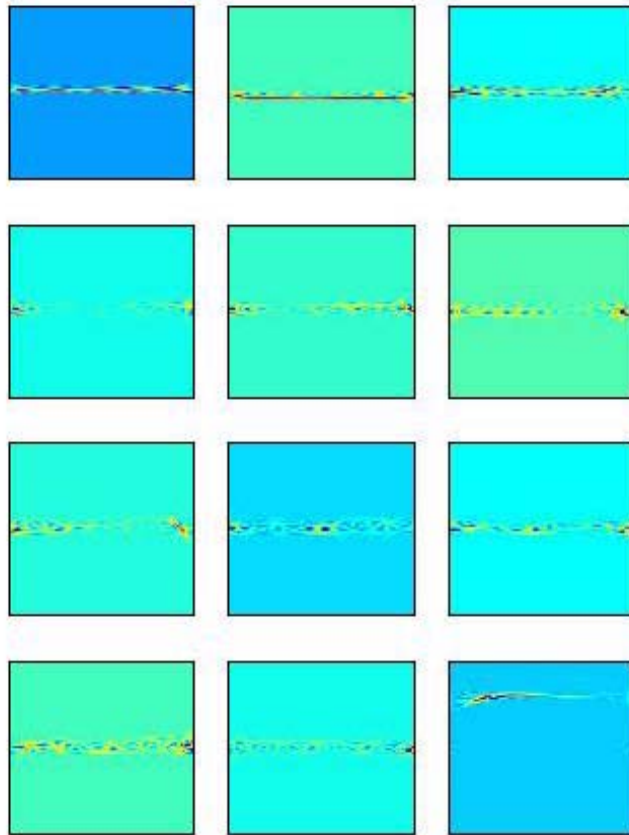


Figure 112: Signal 30 - The frequency representation of the eigenvectors used for the concentration calculation and target detection. In all subplots horizontal axis is for time and vertical axis is for frequency

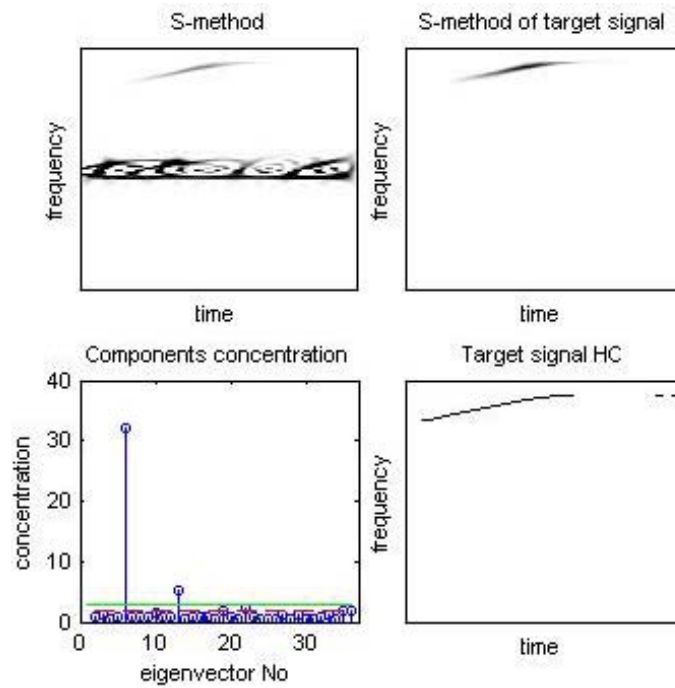


Figure 113: Signal 31 - Concentration of the eigenvectors time-frequency representations (bottom left), Time-frequency representation of the detected target signal (top right), Highly concentrated time-frequency representation of the detected target signal (bottom right)

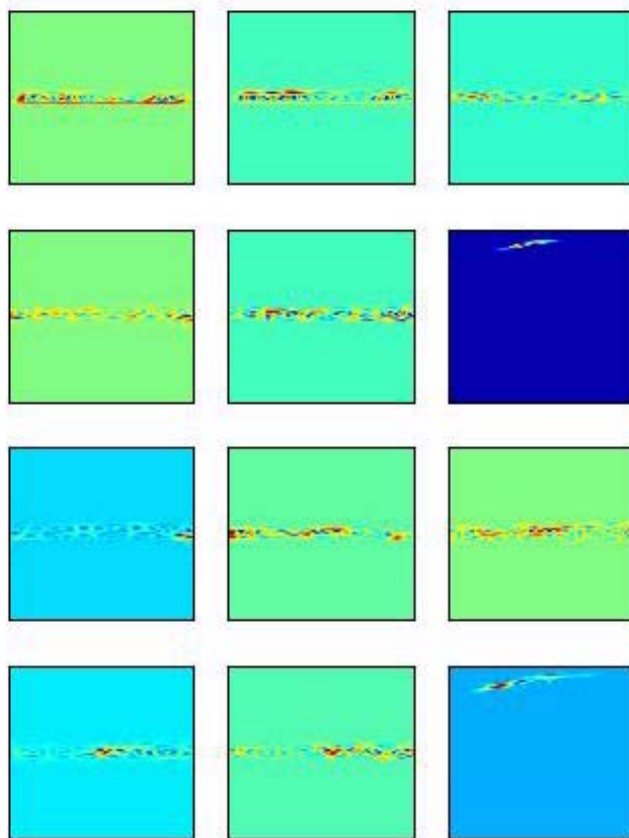


Figure 114: Signal 31 - The frequency representation of the eigenvectors used for the concentration calculation and target detection. In all subplots horizontal axis is for time and vertical axis is for frequency

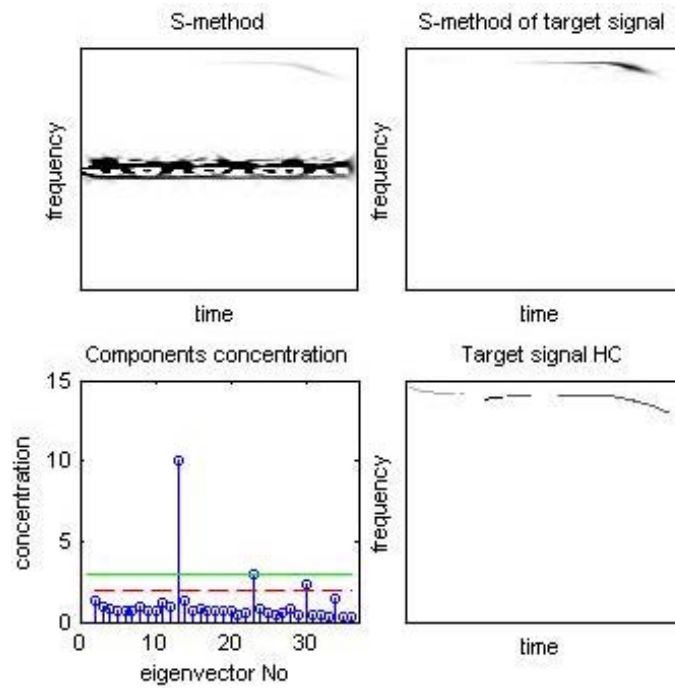


Figure 115: Signal 32 - Concentration of the eigenvectors time-frequency representations (bottom left), Time-frequency representation of the detected target signal (top right), Highly concentrated time-frequency representation of the detected target signal (bottom right)

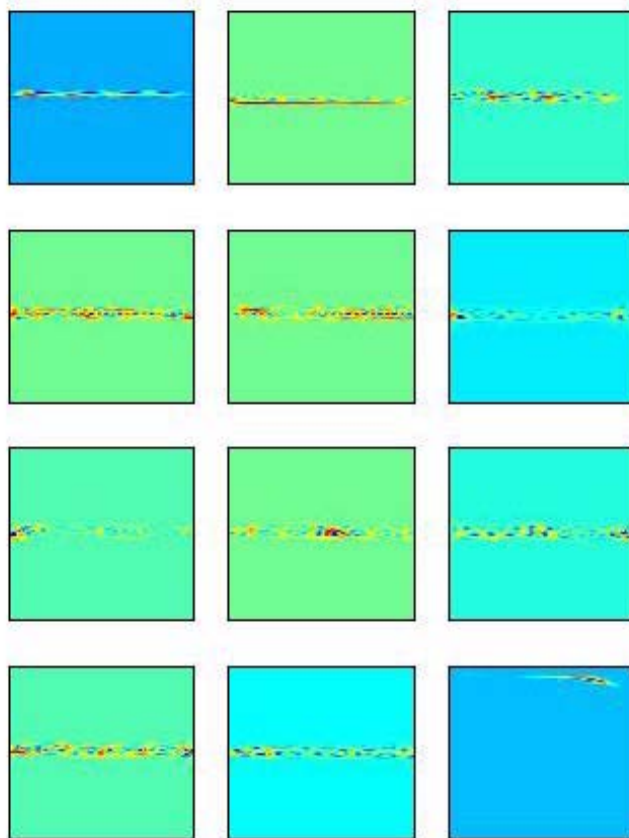


Figure 116: Signal 32 - The frequency representation of the eigenvectors used for the concentration calculation and target detection. In all subplots horizontal axis is for time and vertical axis is for frequency

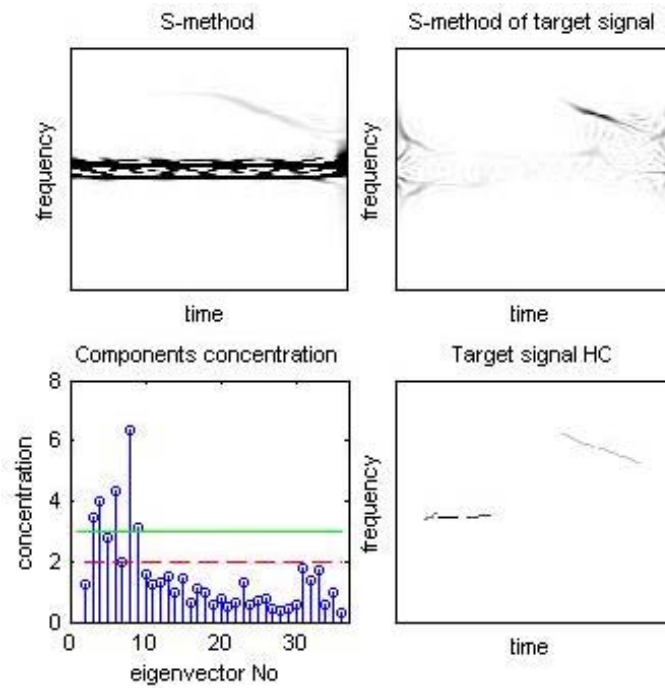


Figure 117: Signal 33 - Concentration of the eigenvectors time-frequency representations (bottom left), Time-frequency representation of the detected target signal (top right), Highly concentrated time-frequency representation of the detected target signal (bottom right)

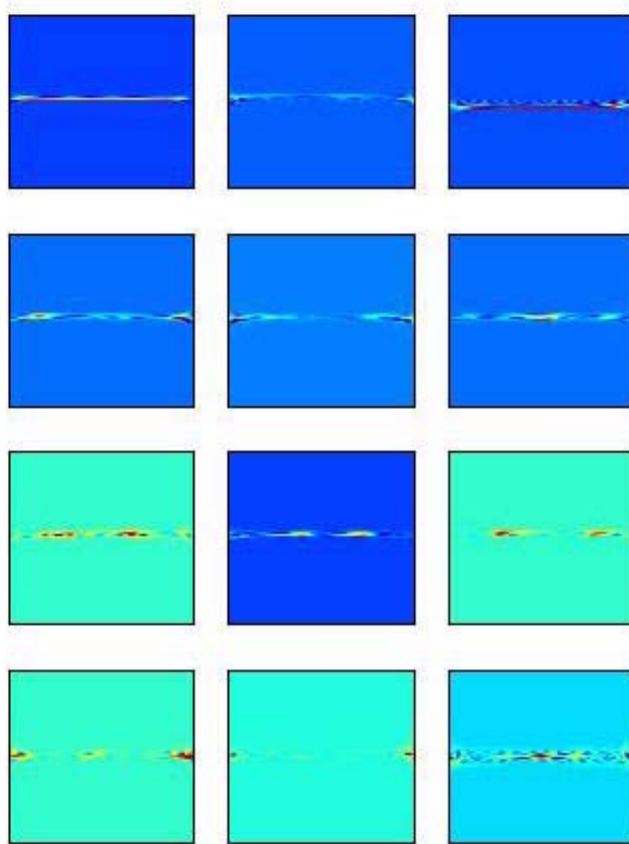


Figure 118: Signal 33 - The frequency representation of the eigenvectors used for the concentration calculation and target detection. In all subplots horizontal axis is for time and vertical axis is for frequency

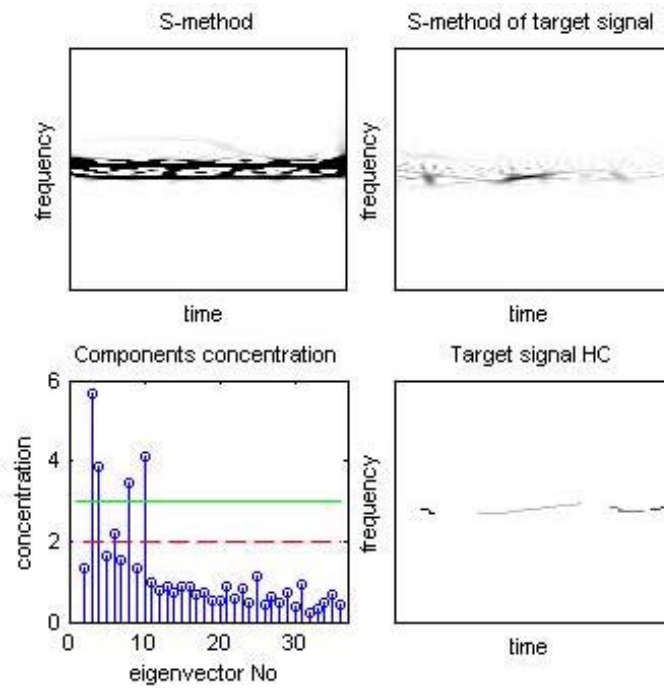


Figure 119: Signal 34 - Concentration of the eigenvectors time-frequency representations (bottom left), Time-frequency representation of the detected target signal (top right), Highly concentrated time-frequency representation of the detected target signal (bottom right)

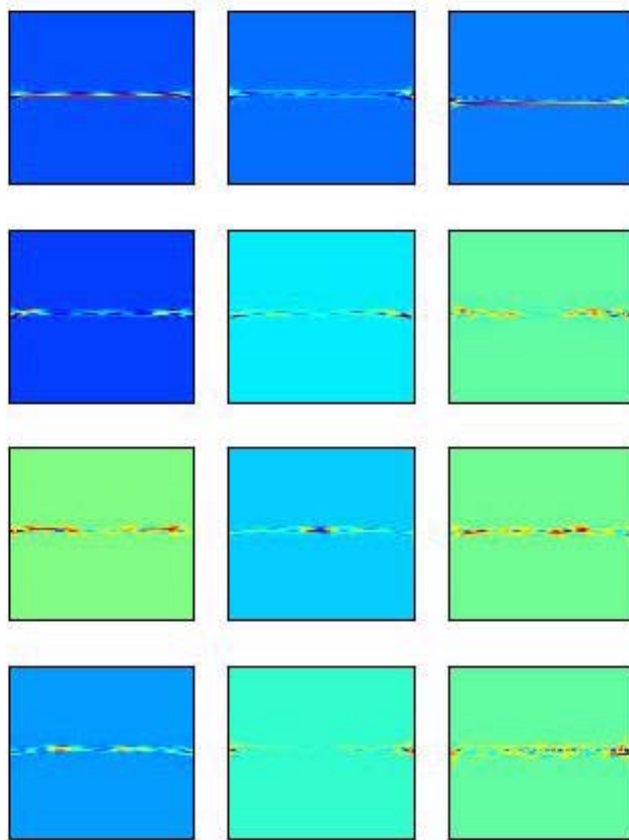


Figure 120: Signal 34 - The frequency representation of the eigenvectors used for the concentration calculation and target detection. In all subplots horizontal axis is for time and vertical axis is for frequency

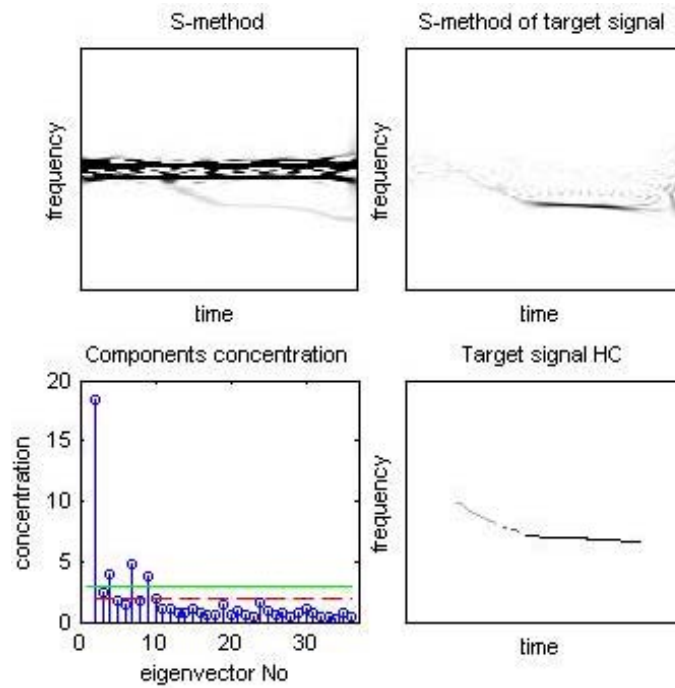


Figure 121: Signal 35 - Concentration of the eigenvectors time-frequency representations (bottom left), Time-frequency representation of the detected target signal (top right), Highly concentrated time-frequency representation of the detected target signal (bottom right)

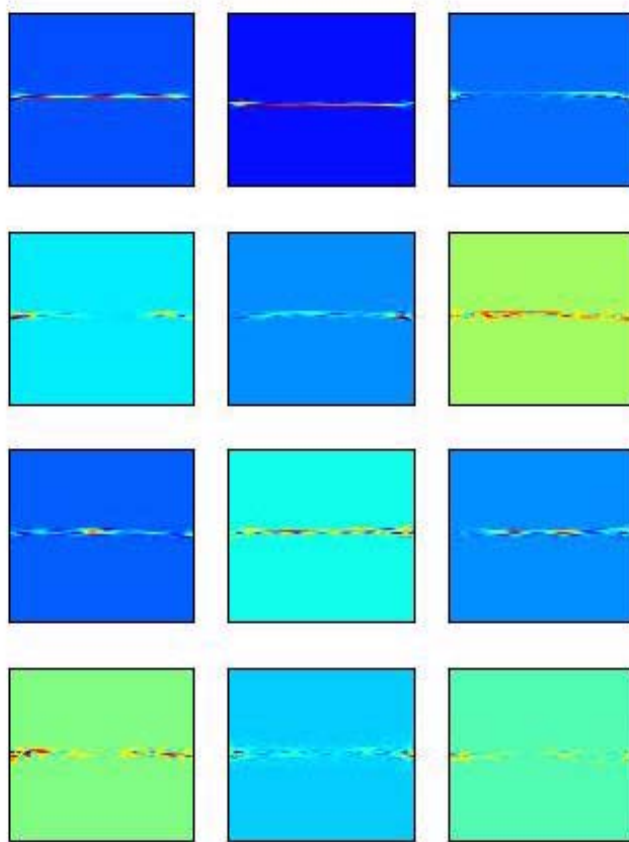


Figure 122: Signal 35 - The frequency representation of the eigenvectors used for the concentration calculation and target detection. In all subplots horizontal axis is for time and vertical axis is for frequency

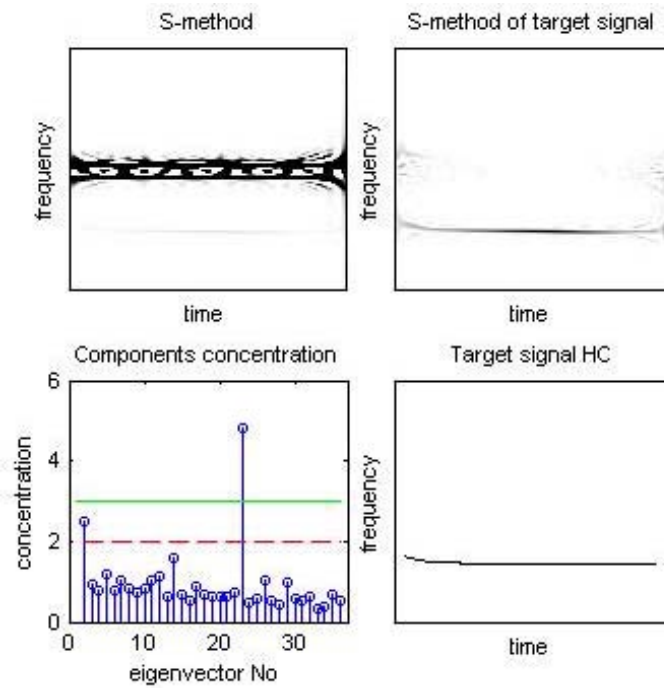


Figure 123: Signal 36 - Concentration of the eigenvectors time-frequency representations (bottom left), Time-frequency representation of the detected target signal (top right), Highly concentrated time-frequency representation of the detected target signal (bottom right)

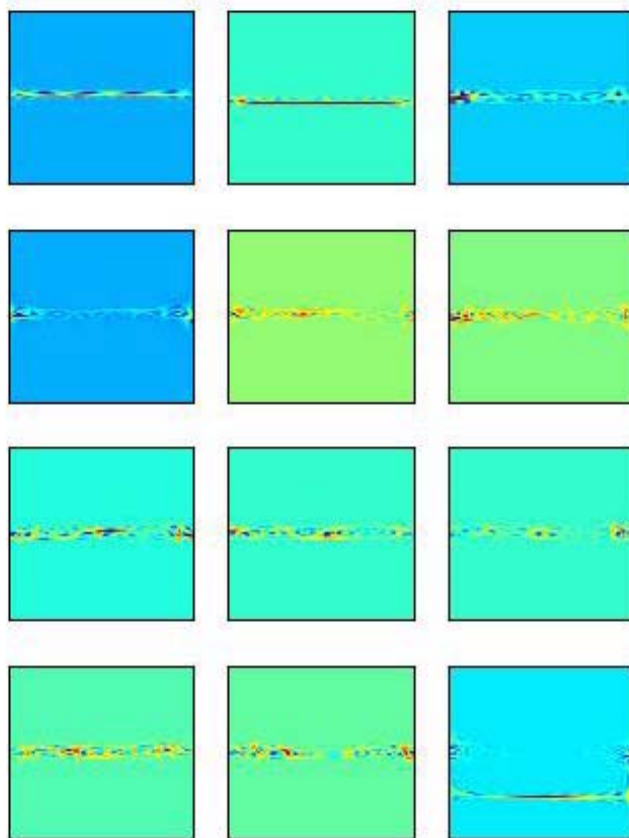


Figure 124: Signal 36 - The frequency representation of the eigenvectors used for the concentration calculation and target detection. In all subplots horizontal axis is for time and vertical axis is for frequency

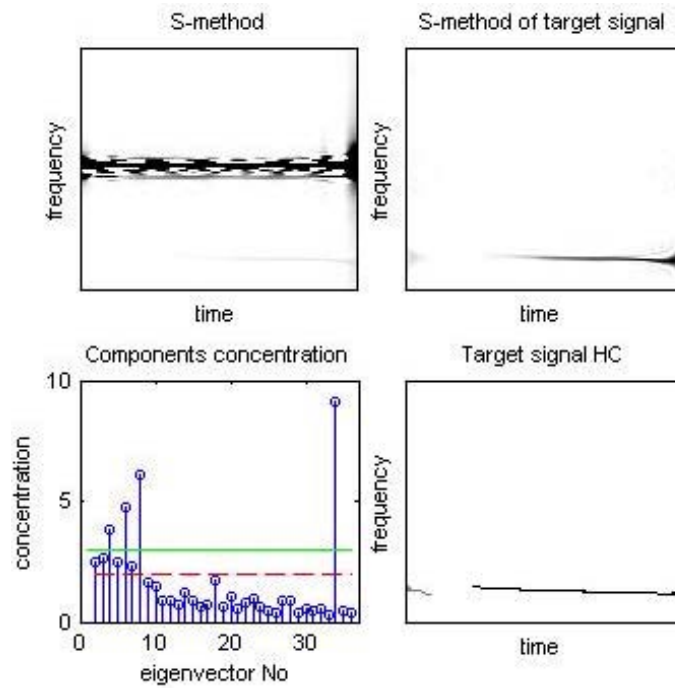


Figure 125: Signal 37 - Concentration of the eigenvectors time-frequency representations (bottom left), Time-frequency representation of the detected target signal (top right), Highly concentrated time-frequency representation of the detected target signal (bottom right)

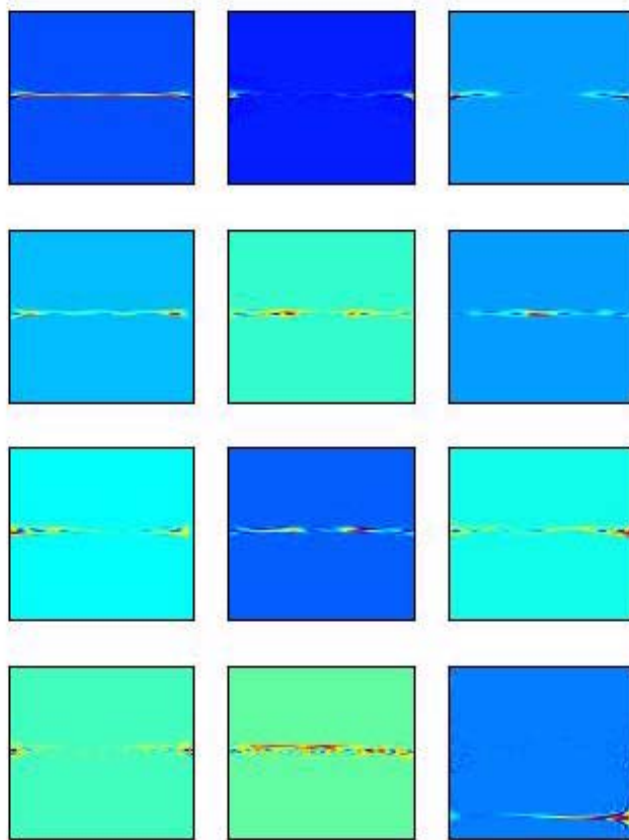


Figure 126: Signal 37 - The frequency representation of the eigenvectors used for the concentration calculation and target detection. In all subplots horizontal axis is for time and vertical axis is for frequency

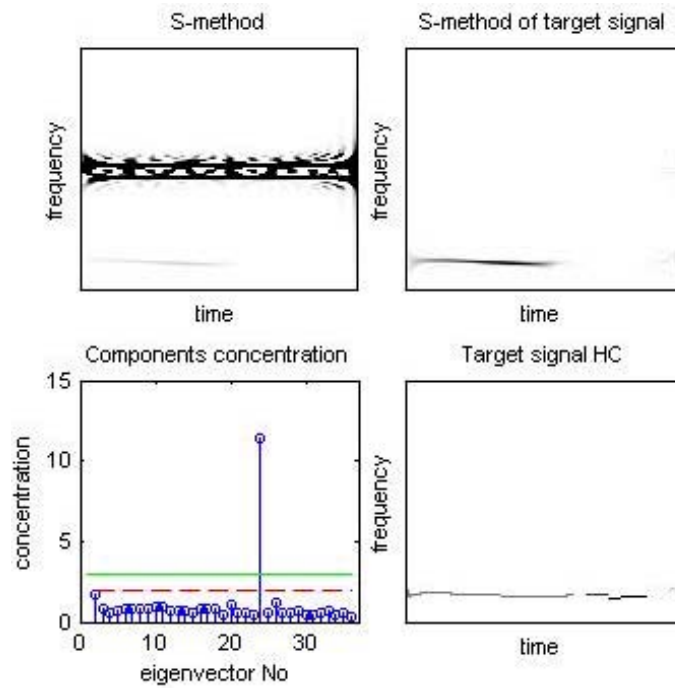


Figure 127: Signal 38 - Concentration of the eigenvectors time-frequency representations (bottom left), Time-frequency representation of the detected target signal (top right), Highly concentrated time-frequency representation of the detected target signal (bottom right)

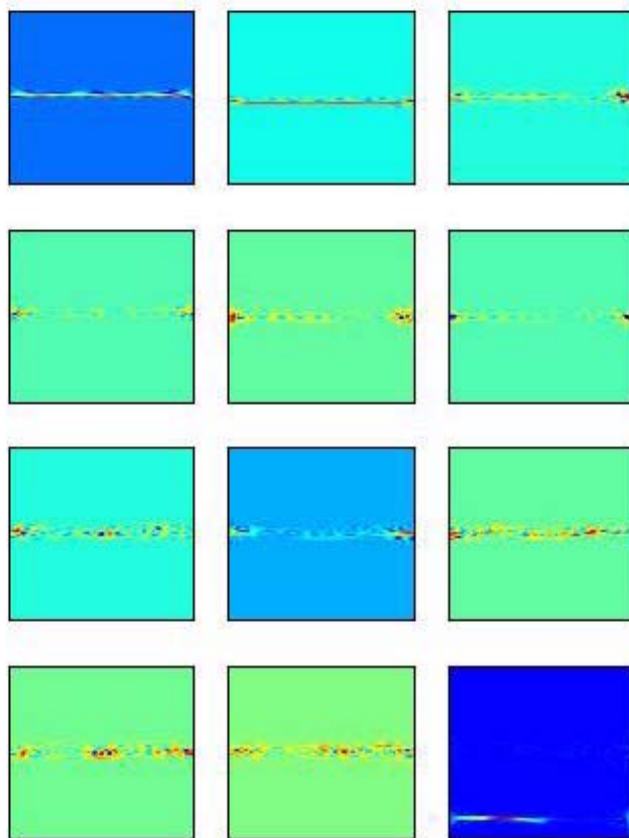


Figure 128: Signal 38 - The frequency representation of the eigenvectors used for the concentration calculation and target detection. In all subplots horizontal axis is for time and vertical axis is for frequency

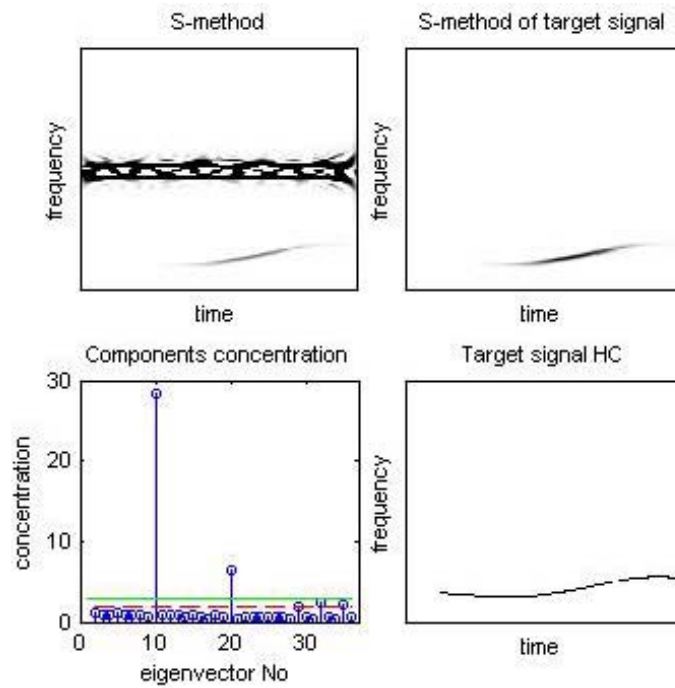


Figure 129: Signal 39 - Concentration of the eigenvectors time-frequency representations (bottom left), Time-frequency representation of the detected target signal (top right), Highly concentrated time-frequency representation of the detected target signal (bottom right)

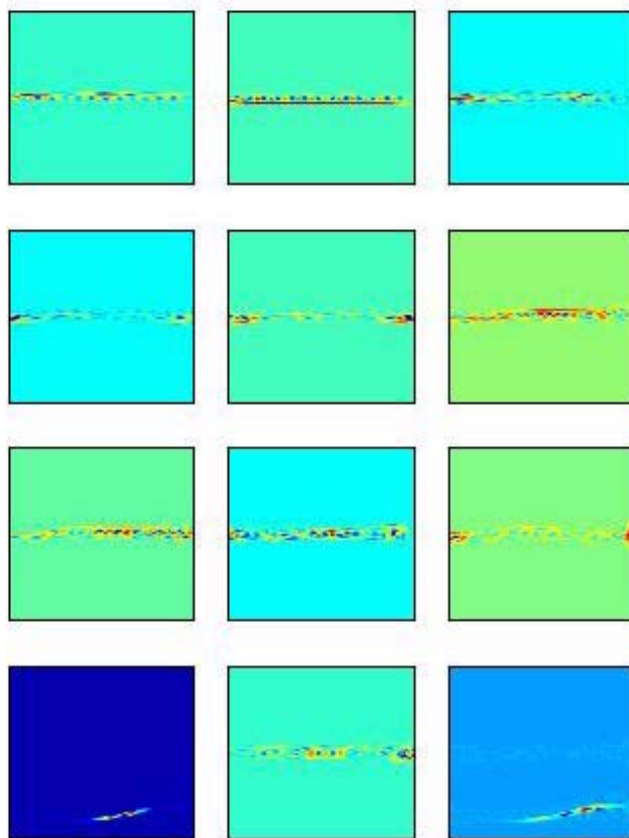


Figure 130: Signal 39 - The frequency representation of the eigenvectors used for the concentration calculation and target detection. In all subplots horizontal axis is for time and vertical axis is for frequency

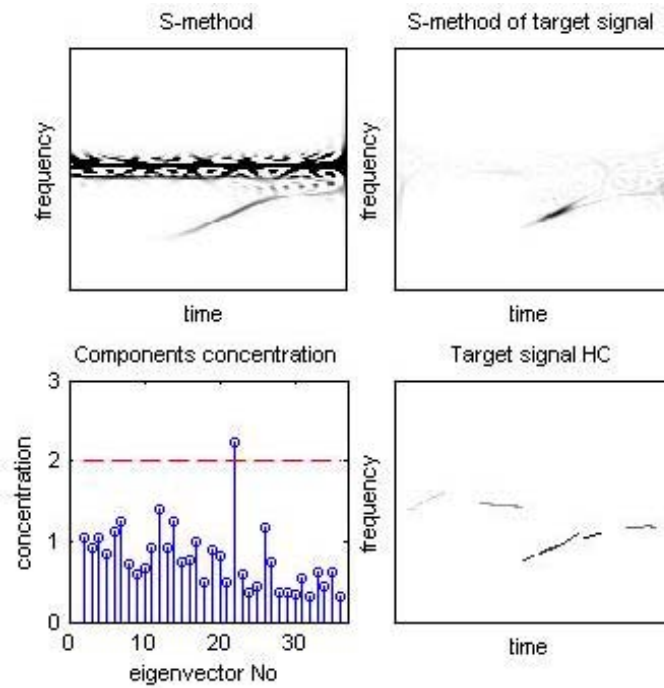


Figure 131: Signal 40 - Concentration of the eigenvectors time-frequency representations (bottom left), Time-frequency representation of the detected target signal (top right), Highly concentrated time-frequency representation of the detected target signal (bottom right)

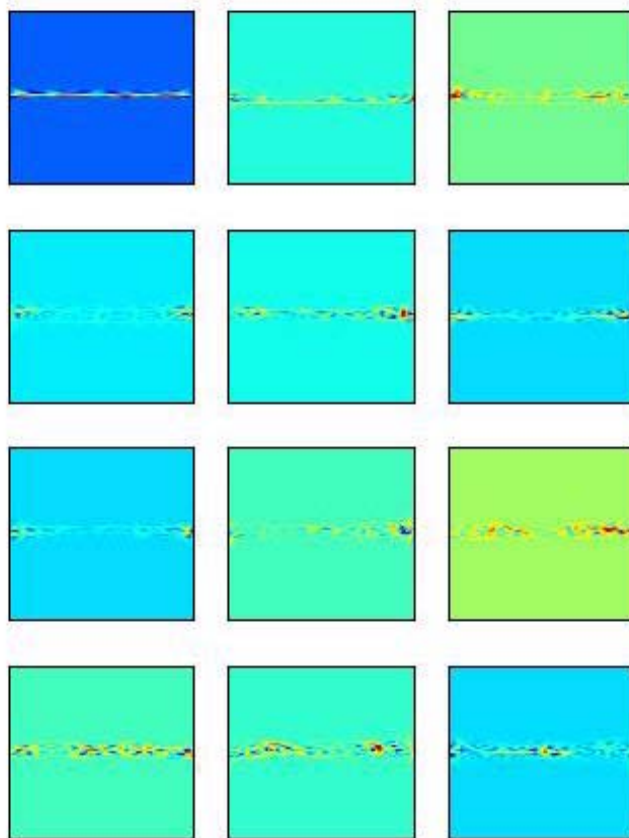


Figure 132: Signal 40 - The frequency representation of the eigenvectors used for the concentration calculation and target detection. In all subplots horizontal axis is for time and vertical axis is for frequency

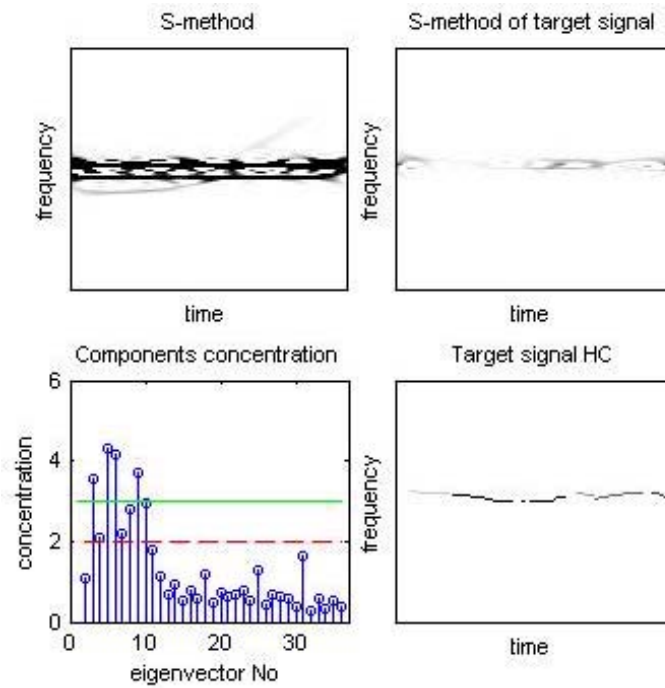


Figure 133: Signal 41 - Concentration of the eigenvectors time-frequency representations (bottom left), Time-frequency representation of the detected target signal (top right), Highly concentrated time-frequency representation of the detected target signal (bottom right)

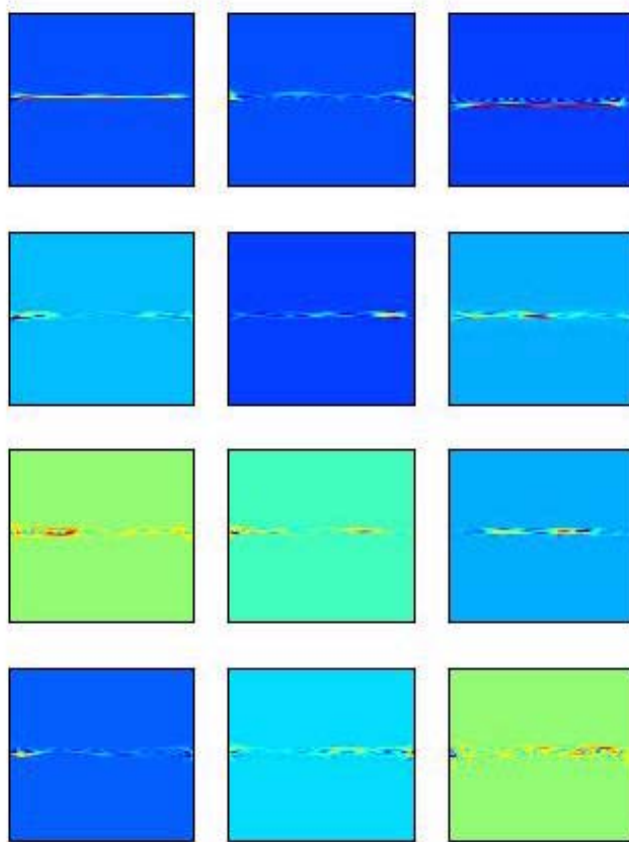


Figure 134: Signal 41 - The frequency representation of the eigenvectors used for the concentration calculation and target detection. In all subplots horizontal axis is for time and vertical axis is for frequency

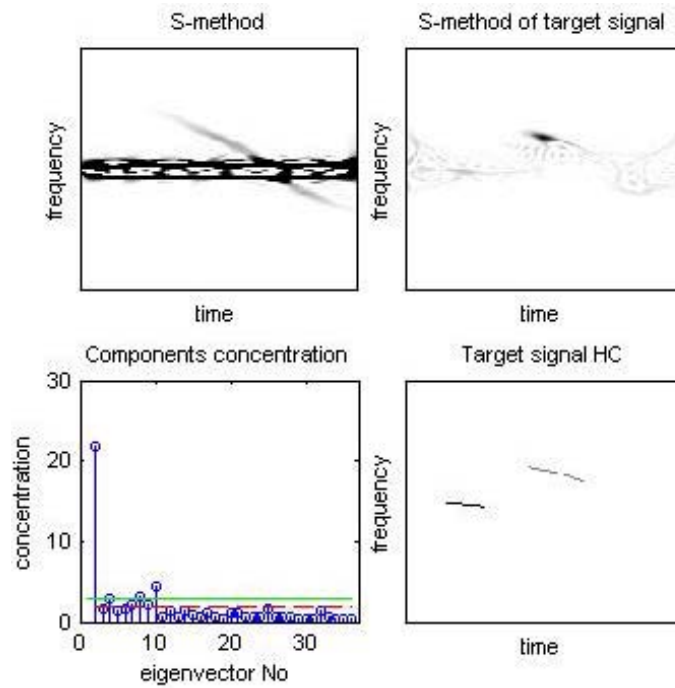


Figure 135: Signal 42 - Concentration of the eigenvectors time-frequency representations (bottom left), Time-frequency representation of the detected target signal (top right), Highly concentrated time-frequency representation of the detected target signal (bottom right)

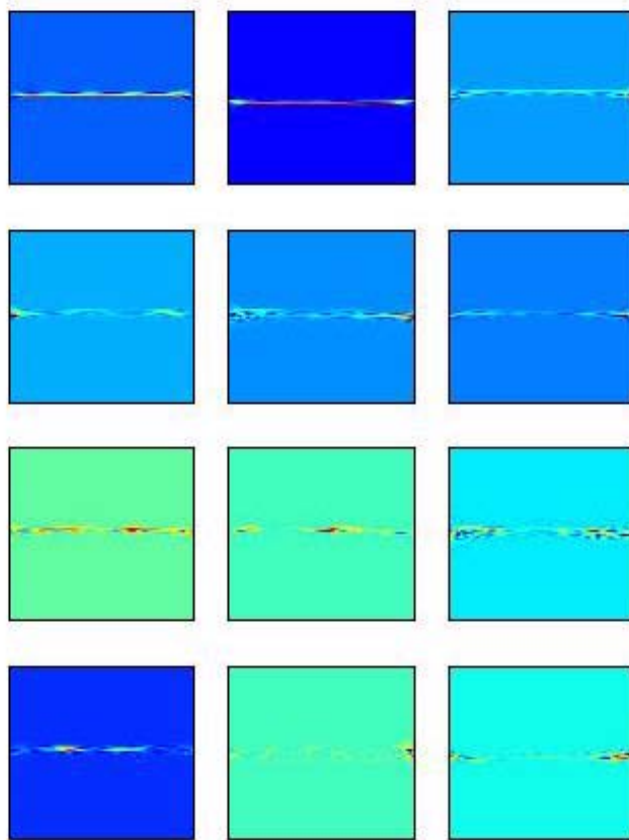


Figure 136: Signal 42 - The frequency representation of the eigenvectors used for the concentration calculation and target detection. In all subplots horizontal axis is for time and vertical axis is for frequency

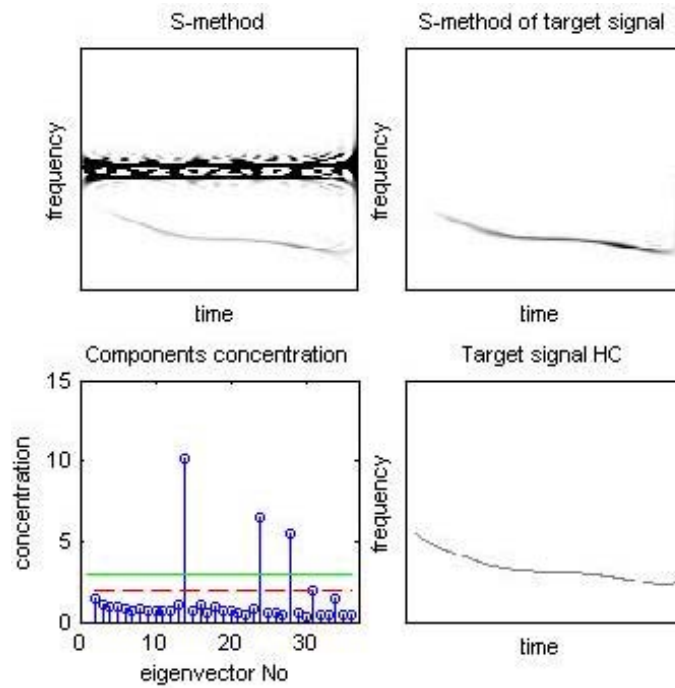


Figure 137: Signal 43 - Concentration of the eigenvectors time-frequency representations (bottom left), Time-frequency representation of the detected target signal (top right), Highly concentrated time-frequency representation of the detected target signal (bottom right)

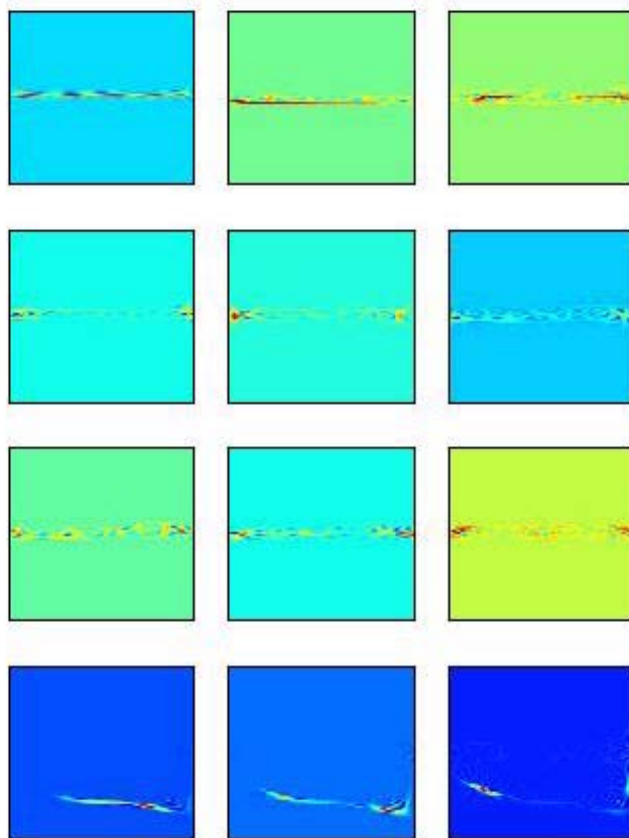


Figure 138: Signal 43 - The frequency representation of the eigenvectors used for the concentration calculation and target detection. In all subplots horizontal axis is for time and vertical axis is for frequency

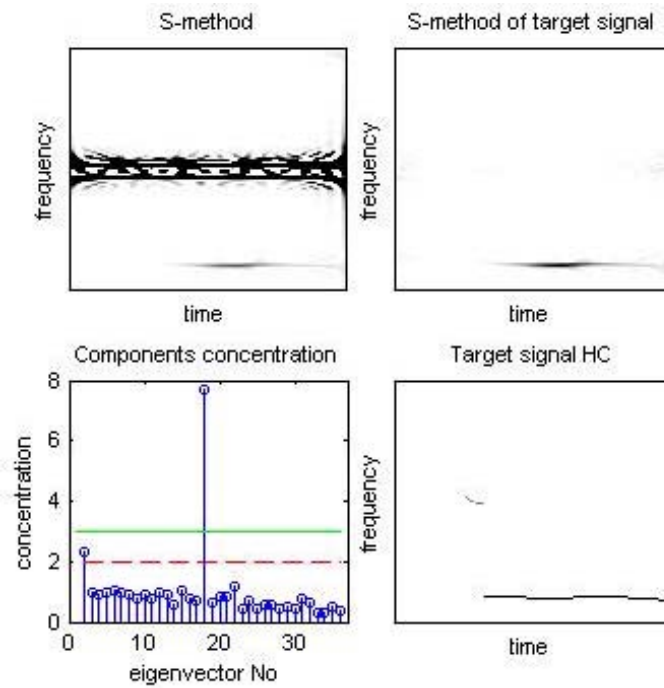


Figure 139: Signal 44 - Concentration of the eigenvectors time-frequency representations (bottom left), Time-frequency representation of the detected target signal (top right), Highly concentrated time-frequency representation of the detected target signal (bottom right)

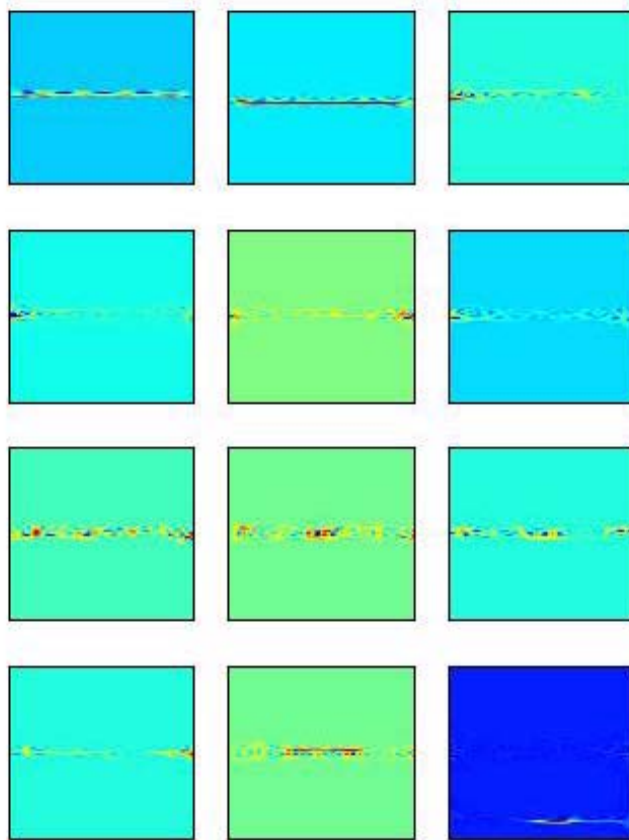


Figure 140: Signal 44 - The frequency representation of the eigenvectors used for the concentration calculation and target detection. In all subplots horizontal axis is for time and vertical axis is for frequency

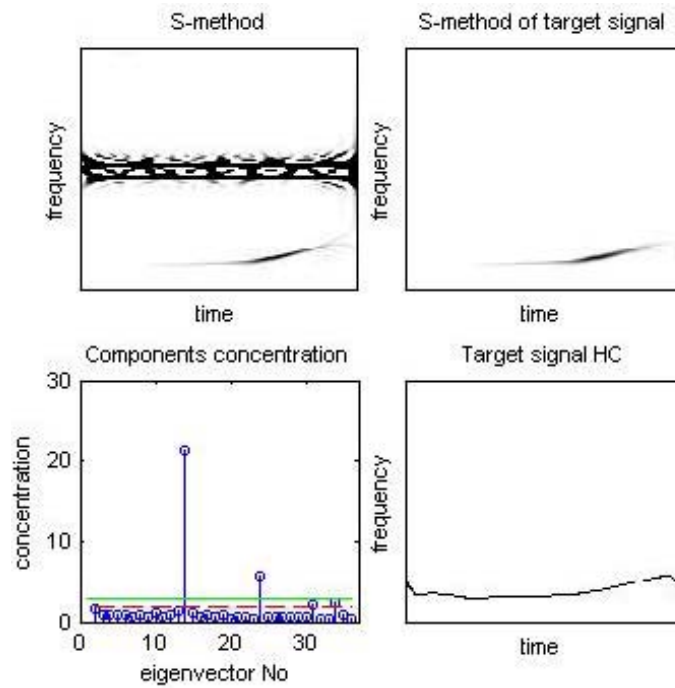


Figure 141: Signal 45 - Concentration of the eigenvectors time-frequency representations (bottom left), Time-frequency representation of the detected target signal (top right), Highly concentrated time-frequency representation of the detected target signal (bottom right)

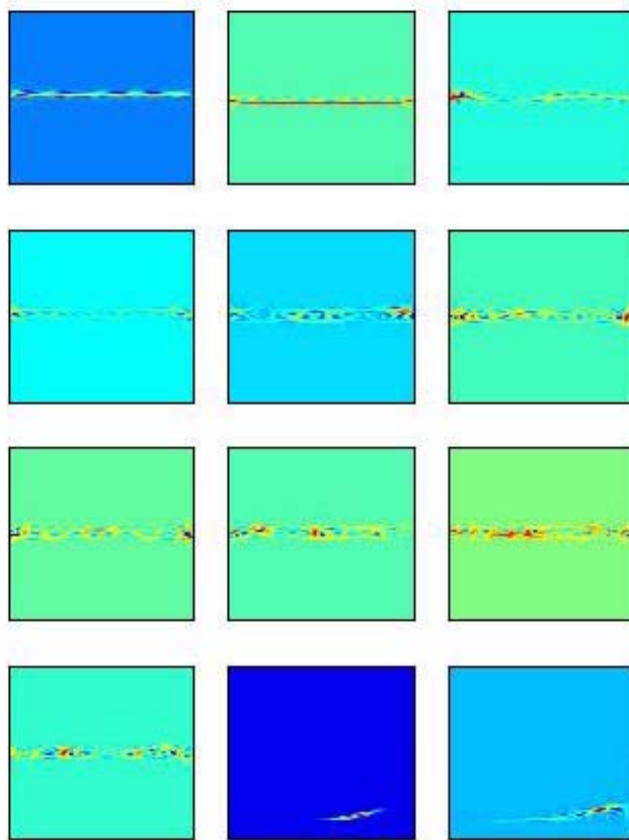


Figure 142: Signal 45 - The frequency representation of the eigenvectors used for the concentration calculation and target detection. In all subplots horizontal axis is for time and vertical axis is for frequency

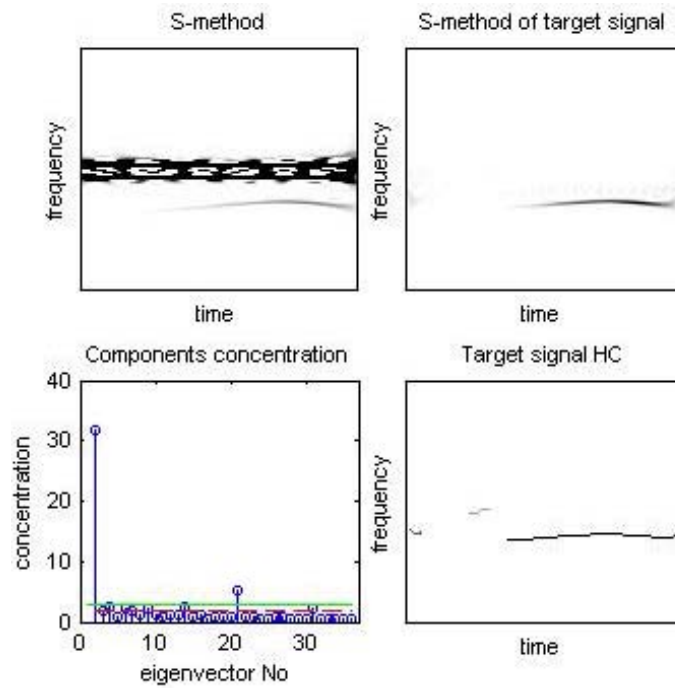


Figure 143: Signal 46 - Concentration of the eigenvectors time-frequency representations (bottom left), Time-frequency representation of the detected target signal (top right), Highly concentrated time-frequency representation of the detected target signal (bottom right)

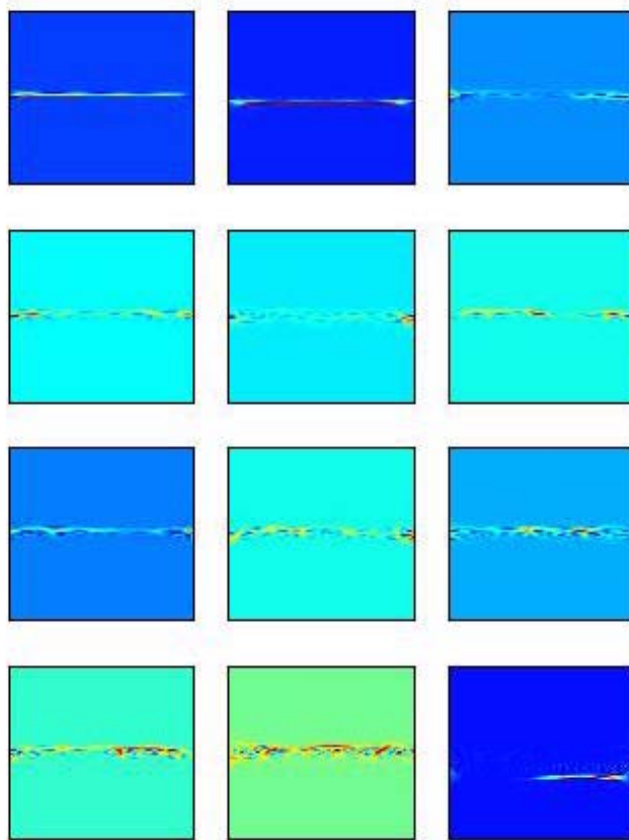


Figure 144: Signal 46 - The frequency representation of the eigenvectors used for the concentration calculation and target detection. In all subplots horizontal axis is for time and vertical axis is for frequency

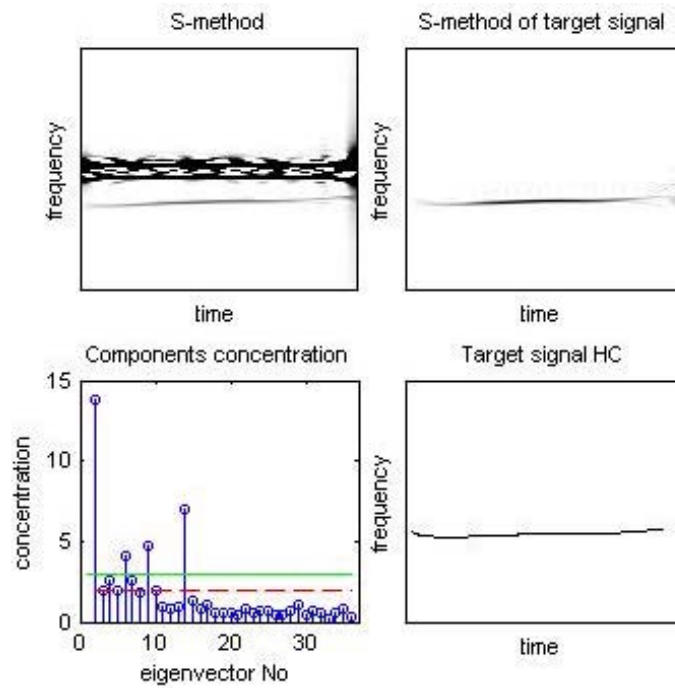


Figure 145: Signal 47 - Concentration of the eigenvectors time-frequency representations (bottom left), Time-frequency representation of the detected target signal (top right), Highly concentrated time-frequency representation of the detected target signal (bottom right)

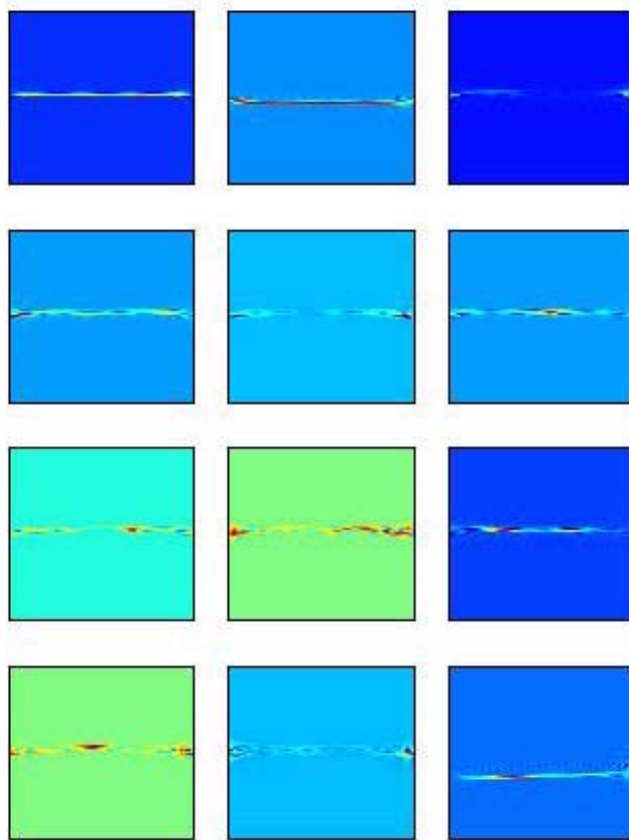


Figure 146: Signal 47 - The frequency representation of the eigenvectors used for the concentration calculation and target detection. In all subplots horizontal axis is for time and vertical axis is for frequency

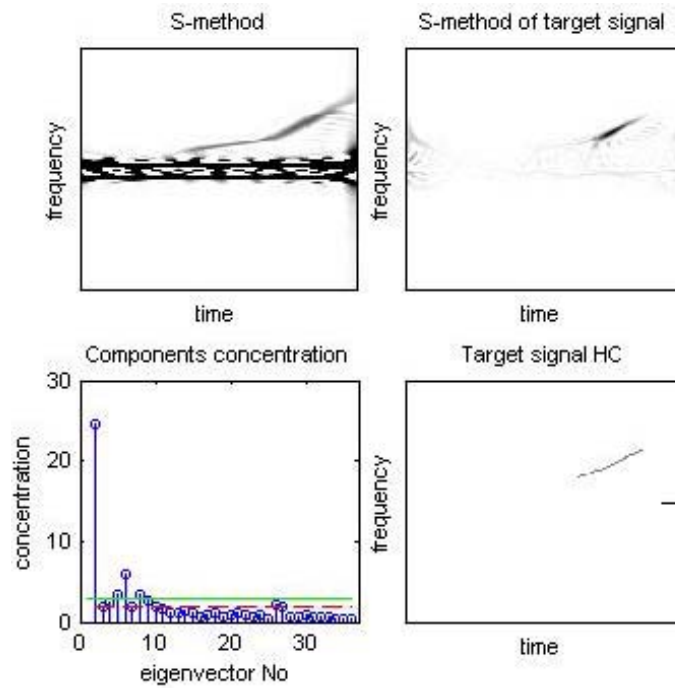


Figure 147: Signal 48 - Concentration of the eigenvectors time-frequency representations (bottom left), Time-frequency representation of the detected target signal (top right), Highly concentrated time-frequency representation of the detected target signal (bottom right)

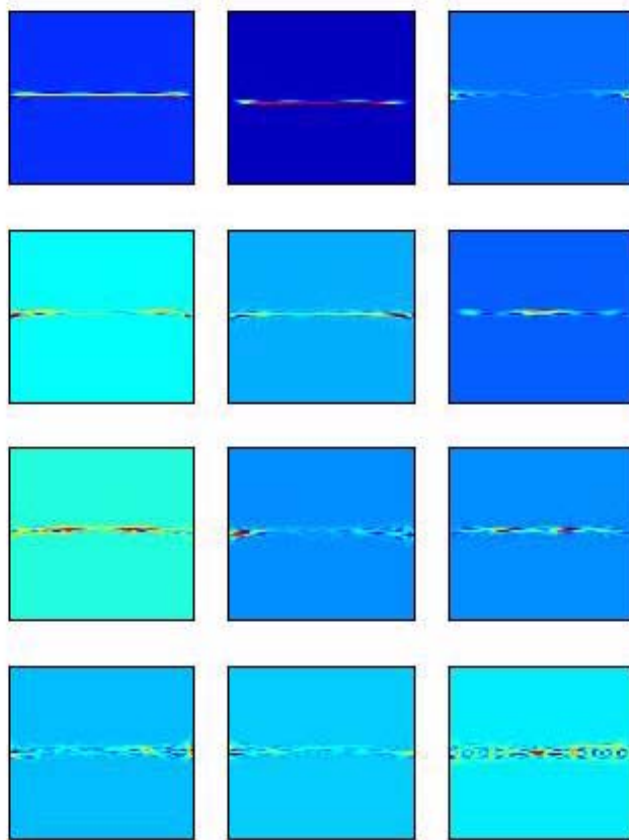


Figure 148: Signal 48 - The frequency representation of the eigenvectors used for the concentration calculation and target detection. In all subplots horizontal axis is for time and vertical axis is for frequency

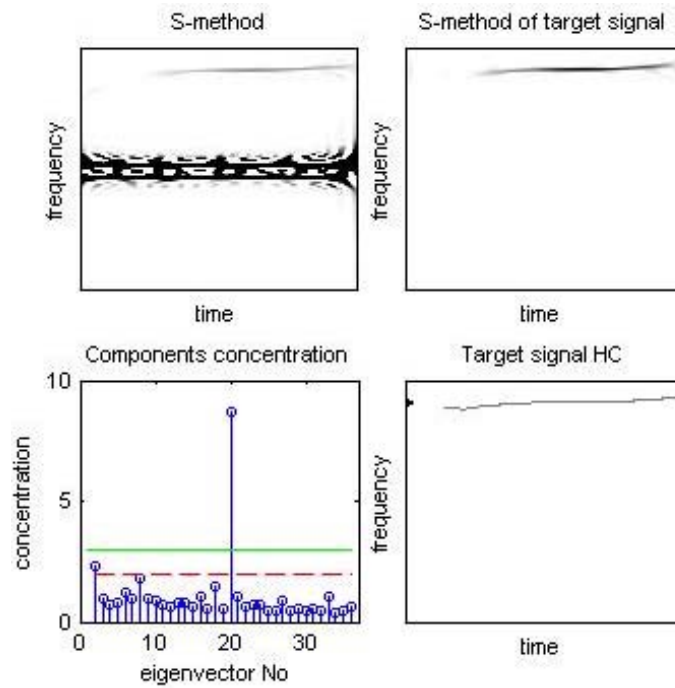


Figure 149: Signal 49 - Concentration of the eigenvectors time-frequency representations (bottom left), Time-frequency representation of the detected target signal (top right), Highly concentrated time-frequency representation of the detected target signal (bottom right)

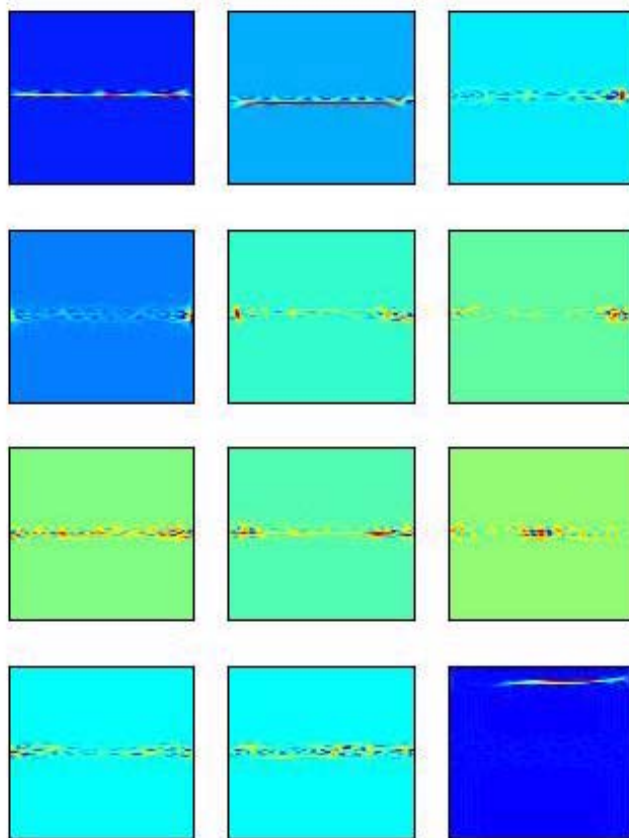


Figure 150: Signal 49 - The frequency representation of the eigenvectors used for the concentration calculation and target detection. In all subplots horizontal axis is for time and vertical axis is for frequency

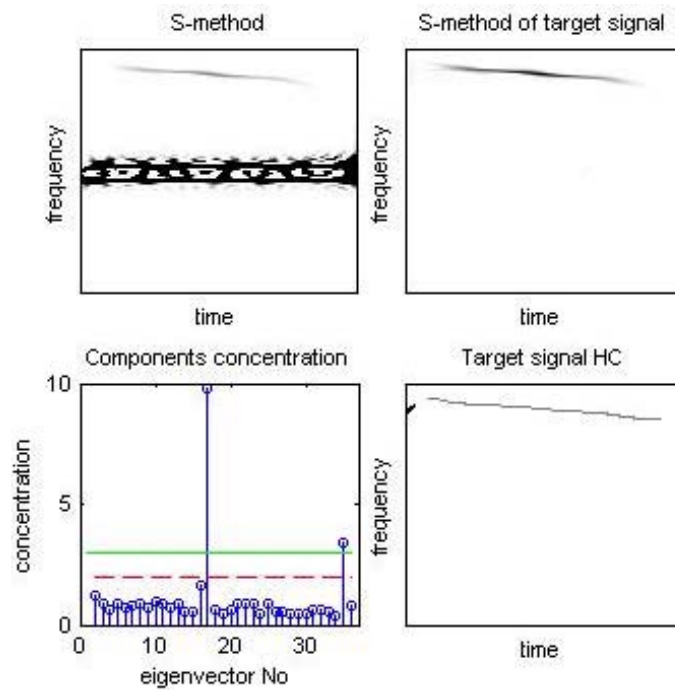


Figure 151: Signal 50 - Concentration of the eigenvectors time-frequency representations (bottom left), Time-frequency representation of the detected target signal (top right), Highly concentrated time-frequency representation of the detected target signal (bottom right)

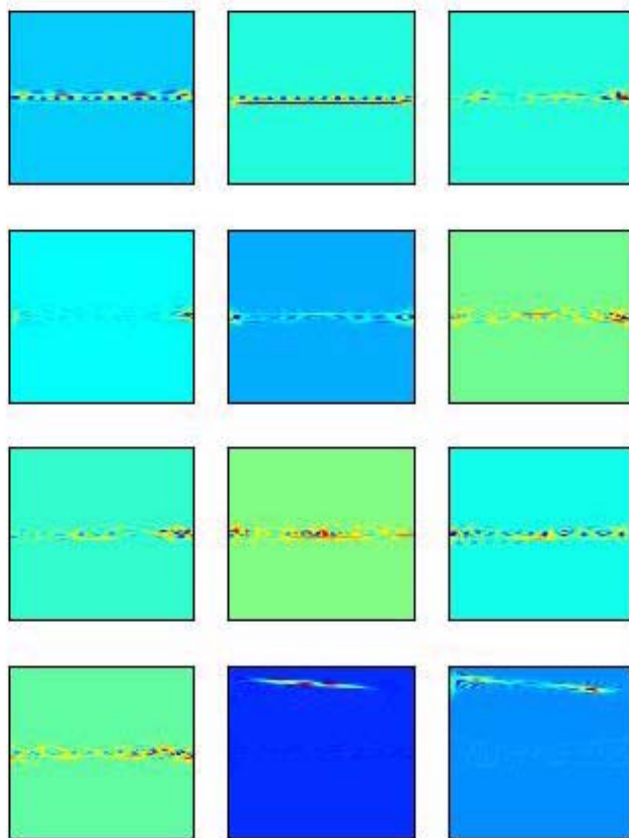


Figure 152: Signal 50 - The frequency representation of the eigenvectors used for the concentration calculation and target detection. In all subplots horizontal axis is for time and vertical axis is for frequency

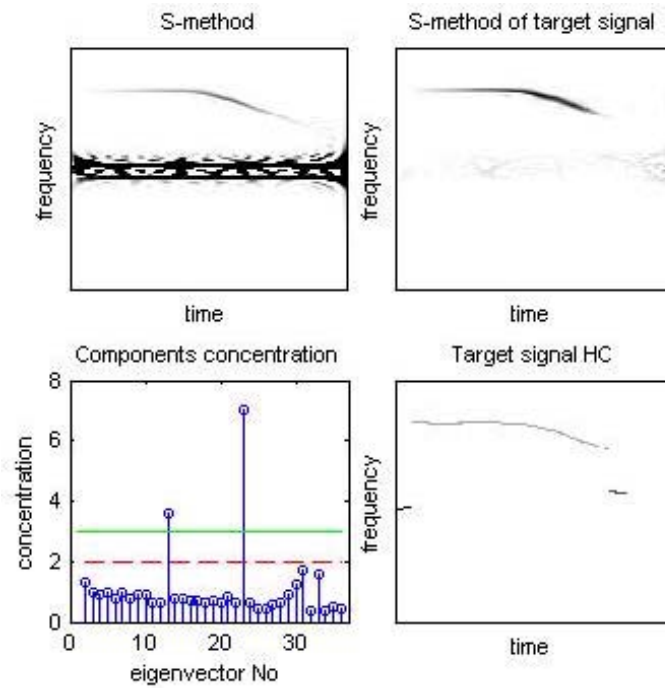


Figure 153: Signal 51 - Concentration of the eigenvectors time-frequency representations (bottom left), Time-frequency representation of the detected target signal (top right), Highly concentrated time-frequency representation of the detected target signal (bottom right)

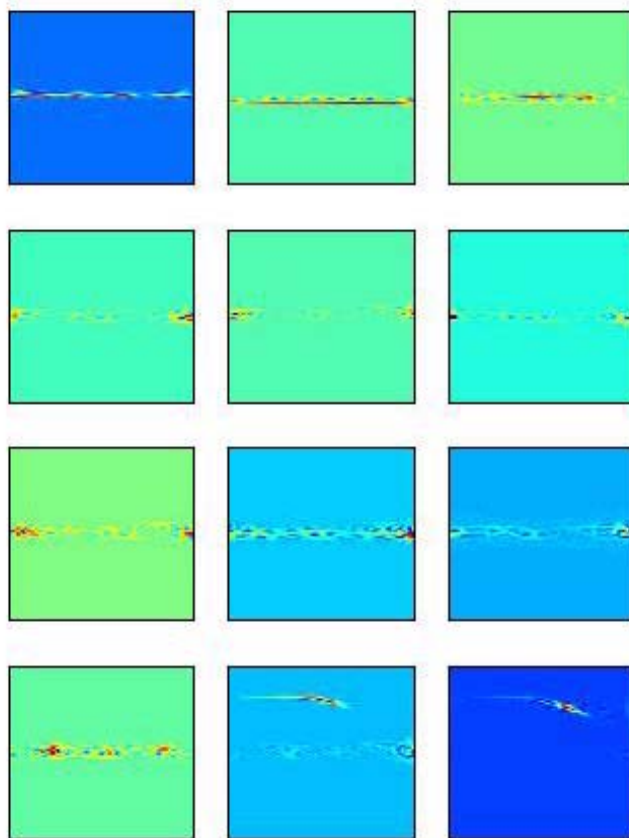


Figure 154: Signal 51 - The frequency representation of the eigenvectors used for the concentration calculation and target detection. In all subplots horizontal axis is for time and vertical axis is for frequency

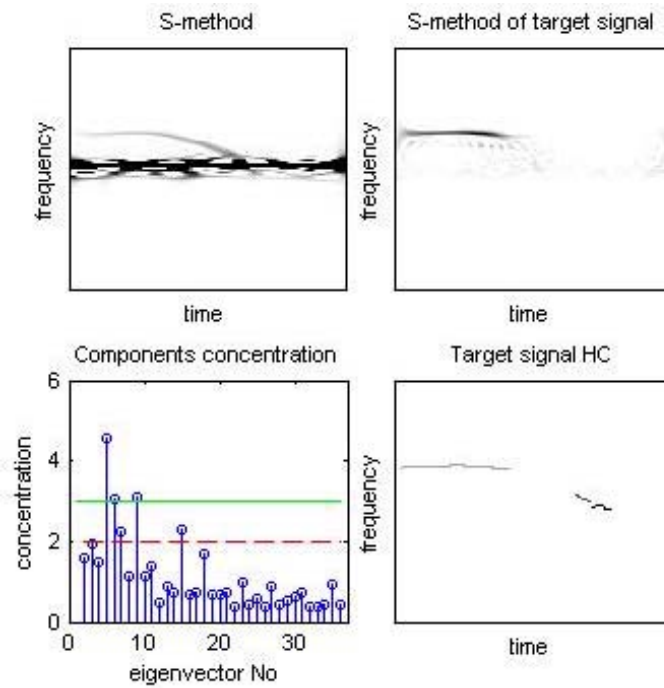


Figure 155: Signal 52 - Concentration of the eigenvectors time-frequency representations (bottom left), Time-frequency representation of the detected target signal (top right), Highly concentrated time-frequency representation of the detected target signal (bottom right)

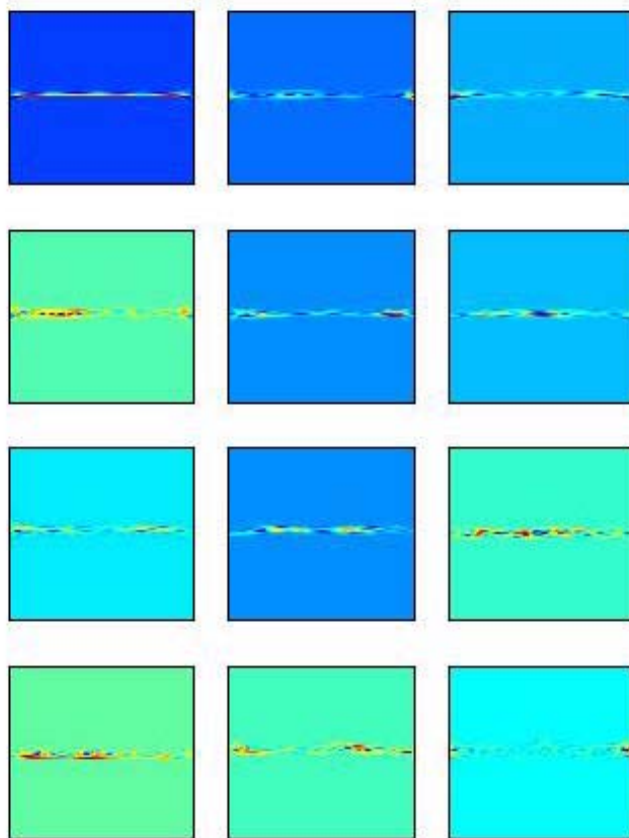


Figure 156: Signal 52 - The frequency representation of the eigenvectors used for the concentration calculation and target detection. In all subplots horizontal axis is for time and vertical axis is for frequency

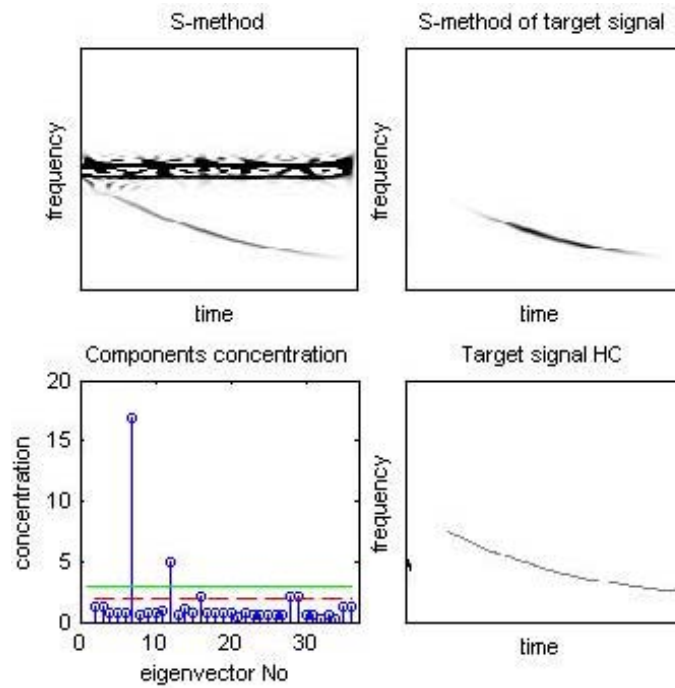


Figure 157: Signal 53 - Concentration of the eigenvectors time-frequency representations (bottom left), Time-frequency representation of the detected target signal (top right), Highly concentrated time-frequency representation of the detected target signal (bottom right)

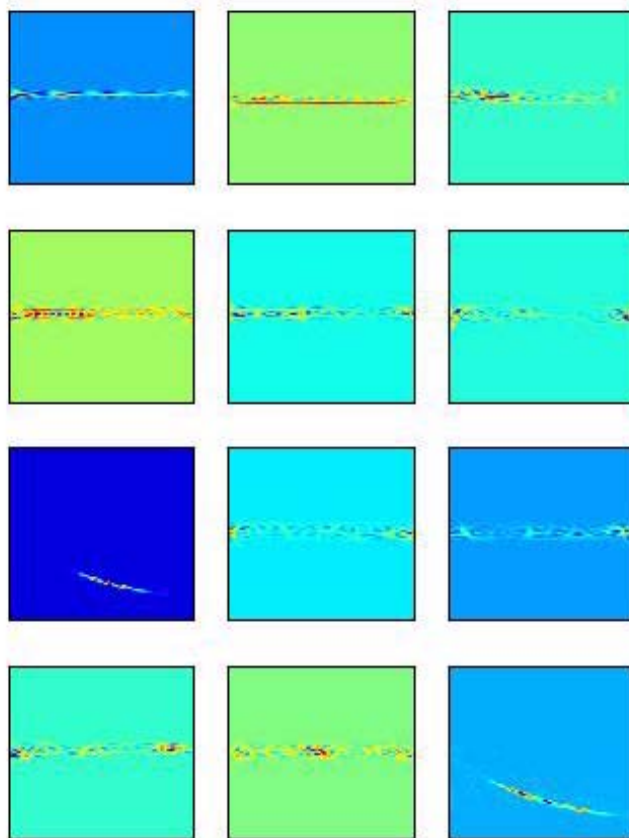


Figure 158: Signal 53 - The frequency representation of the eigenvectors used for the concentration calculation and target detection. In all subplots horizontal axis is for time and vertical axis is for frequency

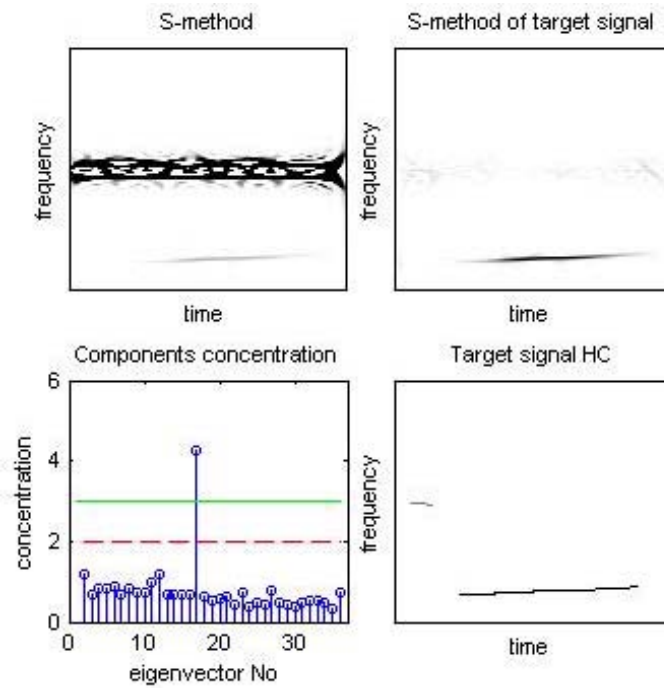


Figure 159: Signal 54 - Concentration of the eigenvectors time-frequency representations (bottom left), Time-frequency representation of the detected target signal (top right), Highly concentrated time-frequency representation of the detected target signal (bottom right)

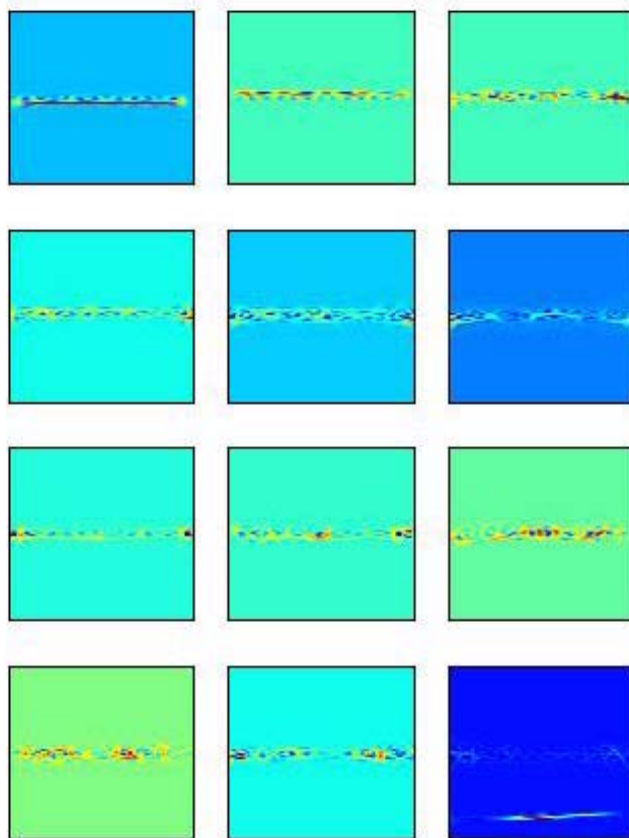


Figure 160: Signal 54 - The frequency representation of the eigenvectors used for the concentration calculation and target detection. In all subplots horizontal axis is for time and vertical axis is for frequency

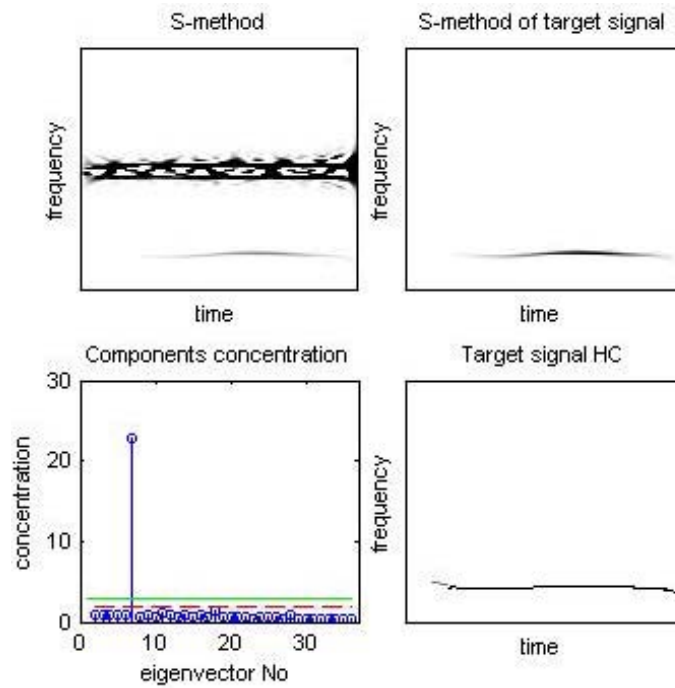


Figure 161: Signal 55 - Concentration of the eigenvectors time-frequency representations (bottom left), Time-frequency representation of the detected target signal (top right), Highly concentrated time-frequency representation of the detected target signal (bottom right)

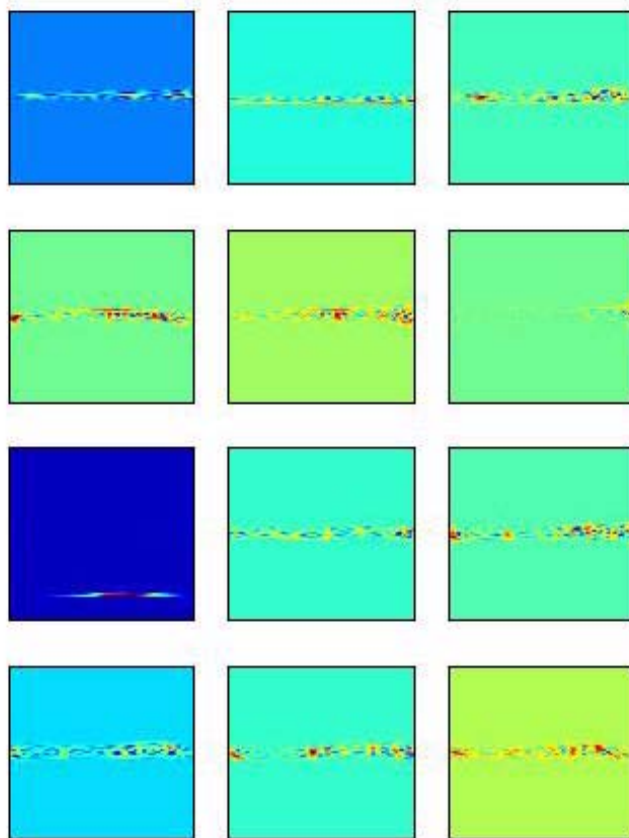


Figure 162: Signal 55 - The frequency representation of the eigenvectors used for the concentration calculation and target detection. In all subplots horizontal axis is for time and vertical axis is for frequency

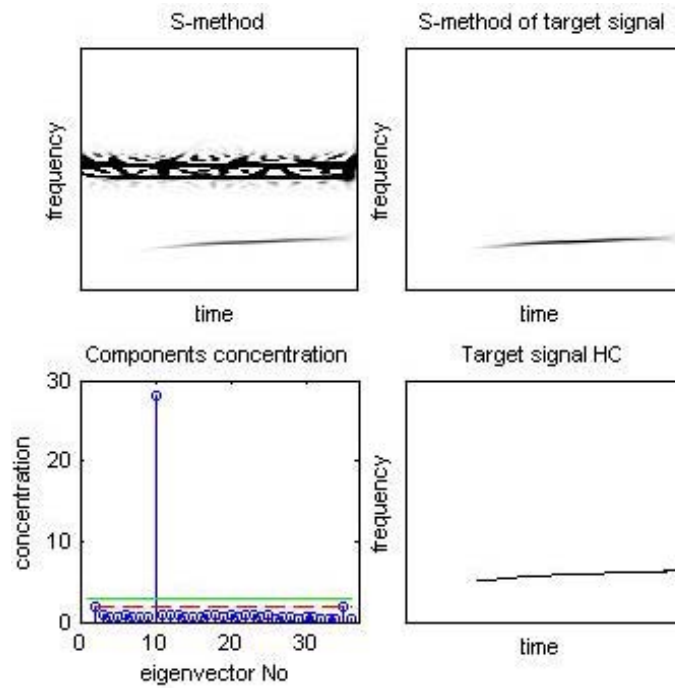


Figure 163: Signal 56 - Concentration of the eigenvectors time-frequency representations (bottom left), Time-frequency representation of the detected target signal (top right), Highly concentrated time-frequency representation of the detected target signal (bottom right)

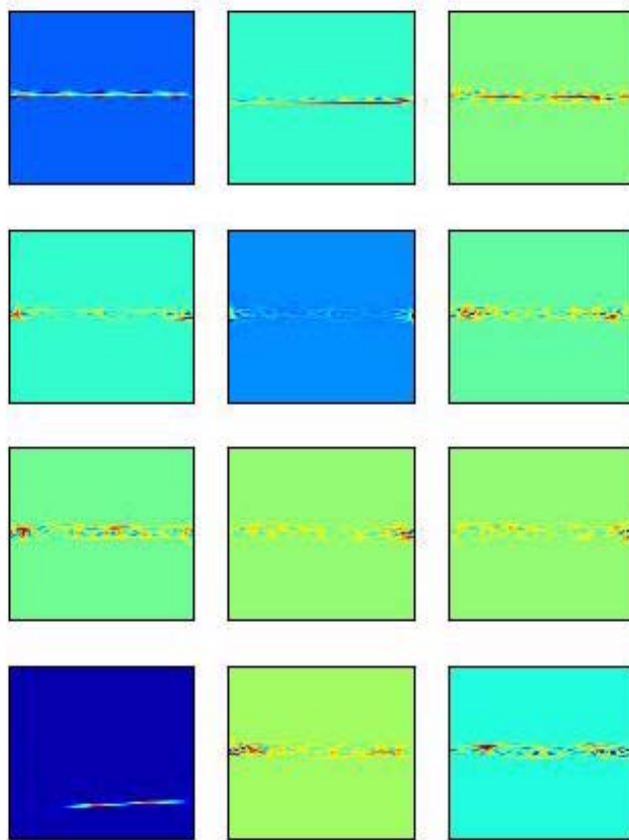


Figure 164: Signal 56 - The frequency representation of the eigenvectors used for the concentration calculation and target detection. In all subplots horizontal axis is for time and vertical axis is for frequency

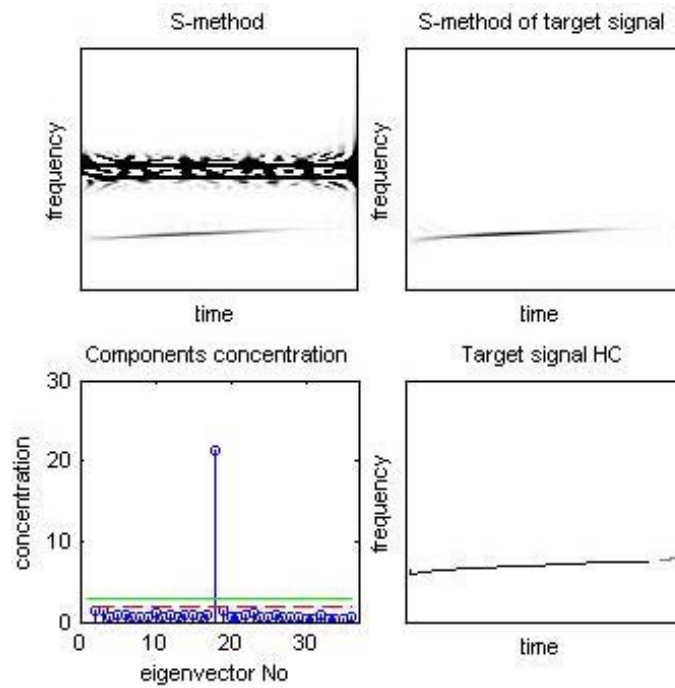


Figure 165: Signal 57 - Concentration of the eigenvectors time-frequency representations (bottom left), Time-frequency representation of the detected target signal (top right), Highly concentrated time-frequency representation of the detected target signal (bottom right)

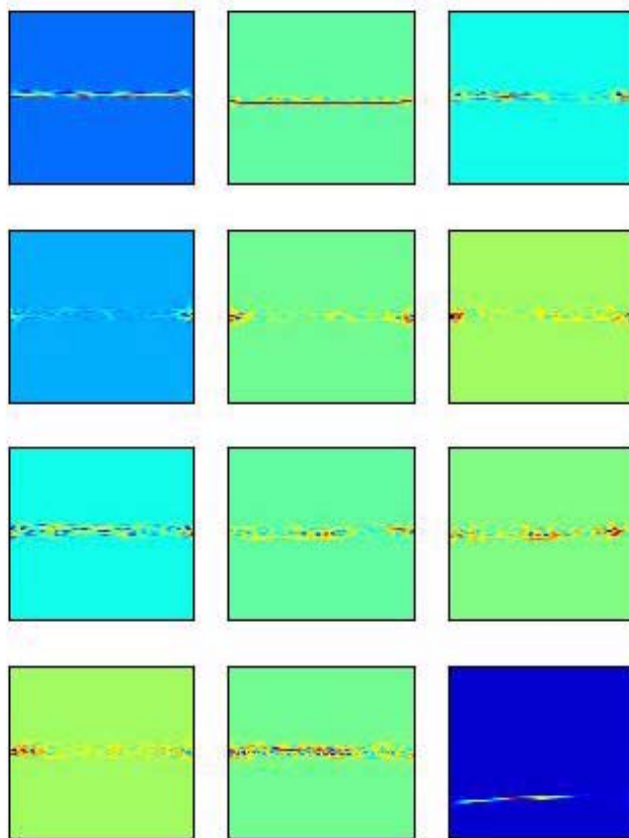


Figure 166: Signal 57 - The frequency representation of the eigenvectors used for the concentration calculation and target detection. In all subplots horizontal axis is for time and vertical axis is for frequency

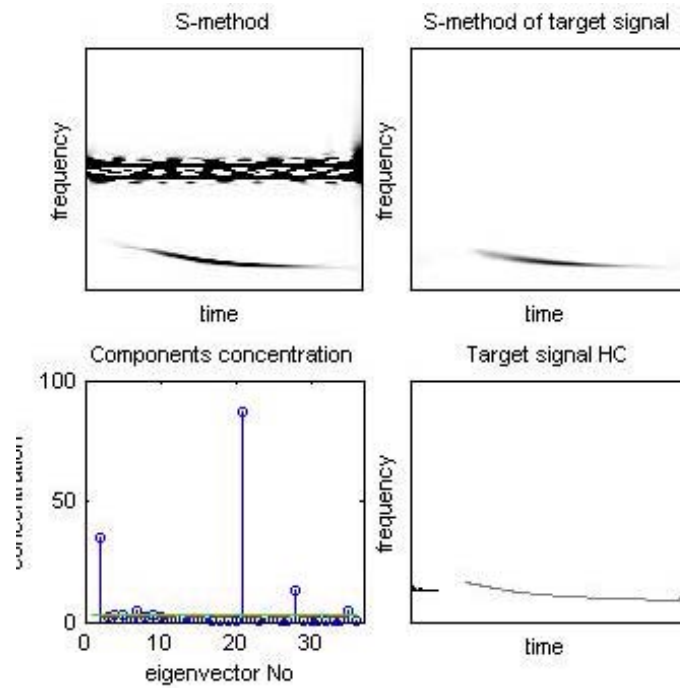


Figure 167: Signal 58 - Concentration of the eigenvectors time-frequency representations (bottom left), Time-frequency representation of the detected target signal (top right), Highly concentrated time-frequency representation of the detected target signal (bottom right)

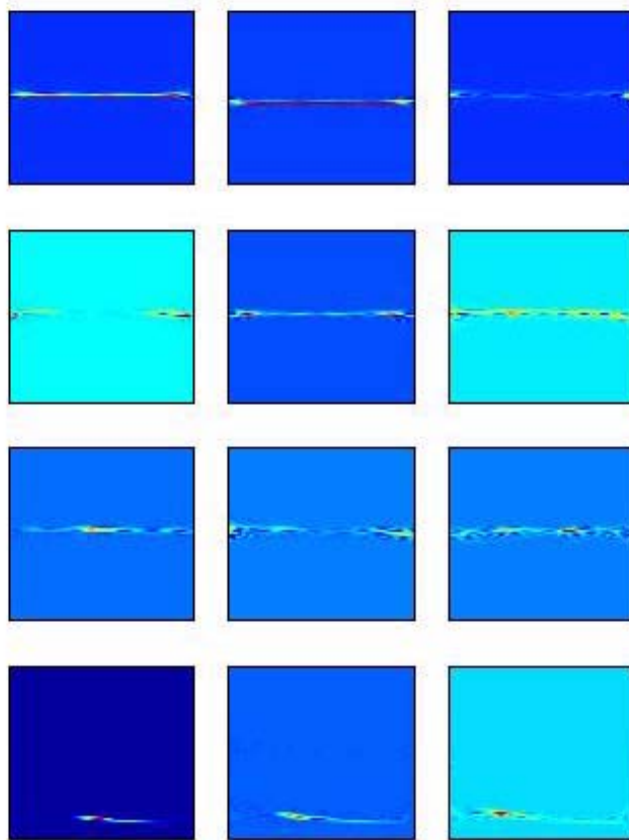


Figure 168: Signal 58 - The frequency representation of the eigenvectors used for the concentration calculation and target detection. In all subplots horizontal axis is for time and vertical axis is for frequency

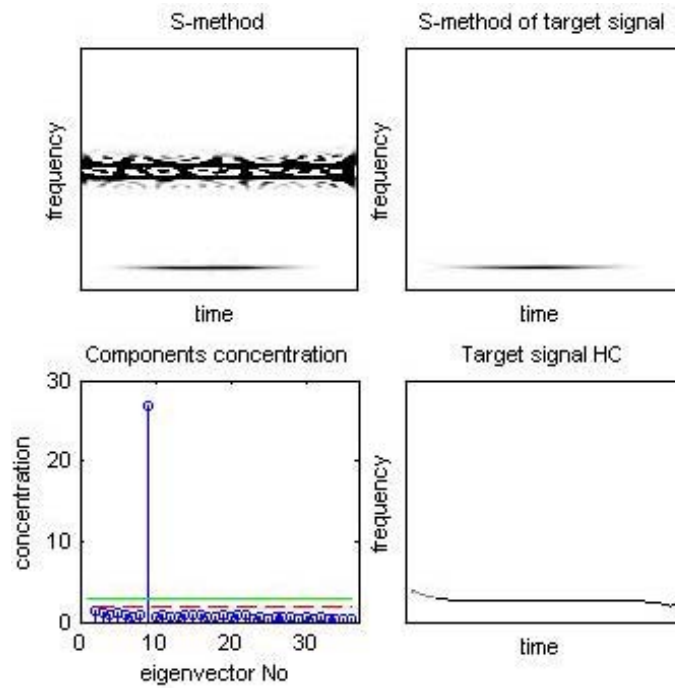


Figure 169: Signal 59 - Concentration of the eigenvectors time-frequency representations (bottom left), Time-frequency representation of the detected target signal (top right), Highly concentrated time-frequency representation of the detected target signal (bottom right)

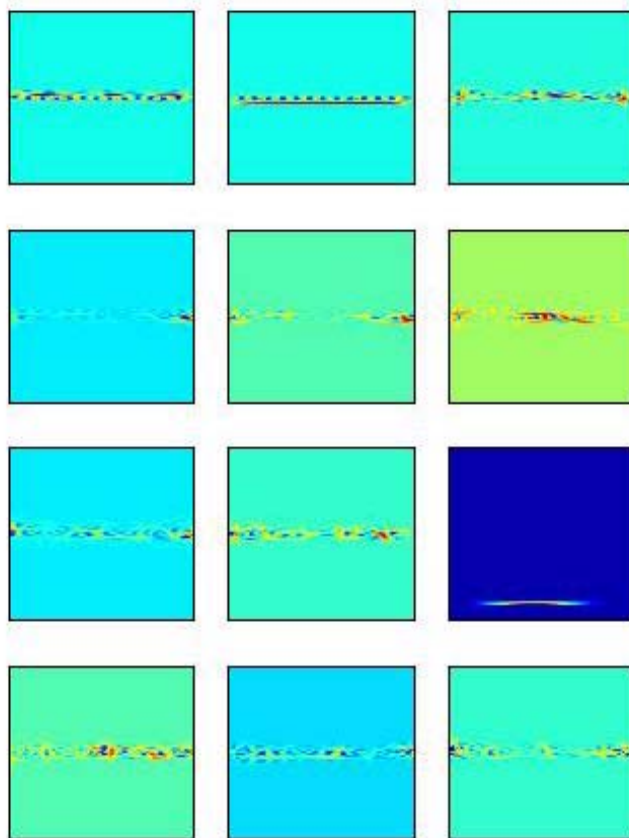


Figure 170: Signal 60 - The frequency representation of the eigenvectors used for the concentration calculation and target detection. In all subplots horizontal axis is for time and vertical axis is for frequency

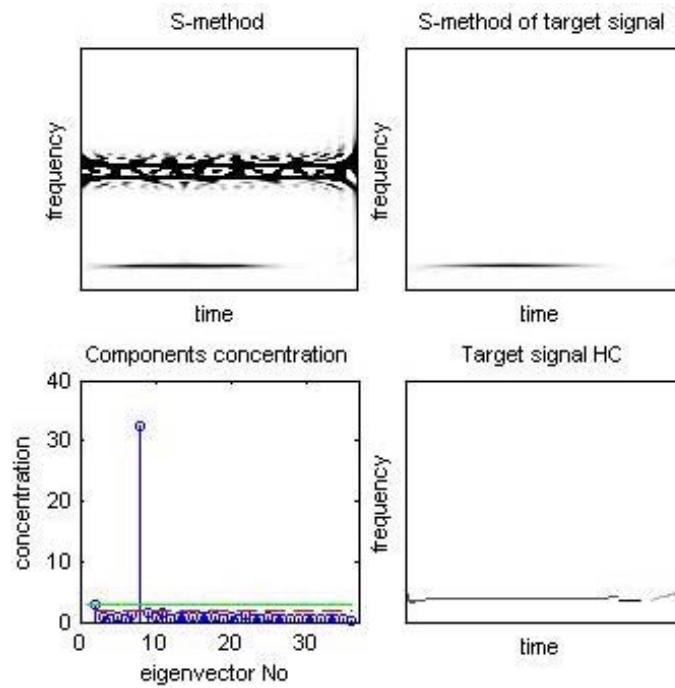


Figure 171: Signal 60 - Concentration of the eigenvectors time-frequency representations (bottom left), Time-frequency representation of the detected target signal (top right), Highly concentrated time-frequency representation of the detected target signal (bottom right)

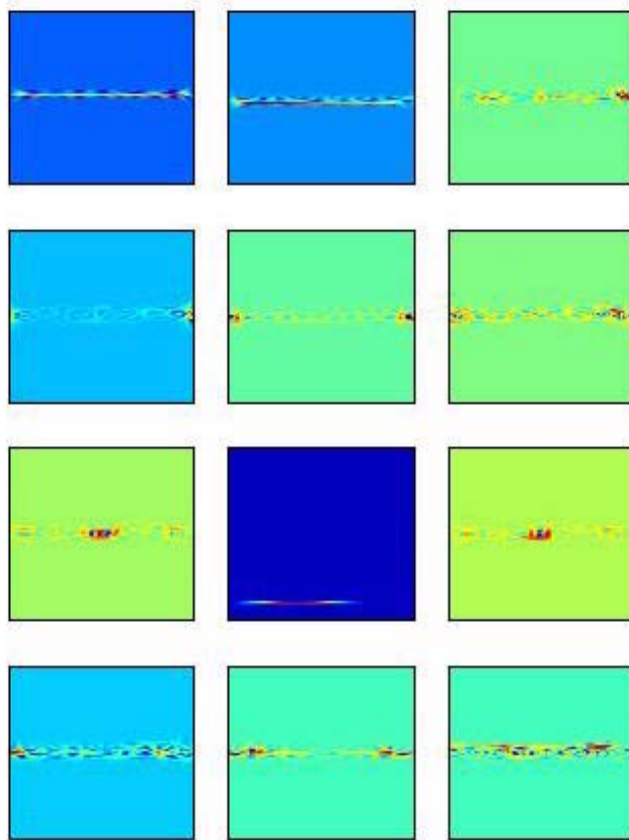


Figure 172: Signal 60 - The frequency representation of the eigenvectors used for the concentration calculation and target detection. In all subplots horizontal axis is for time and vertical axis is for frequency

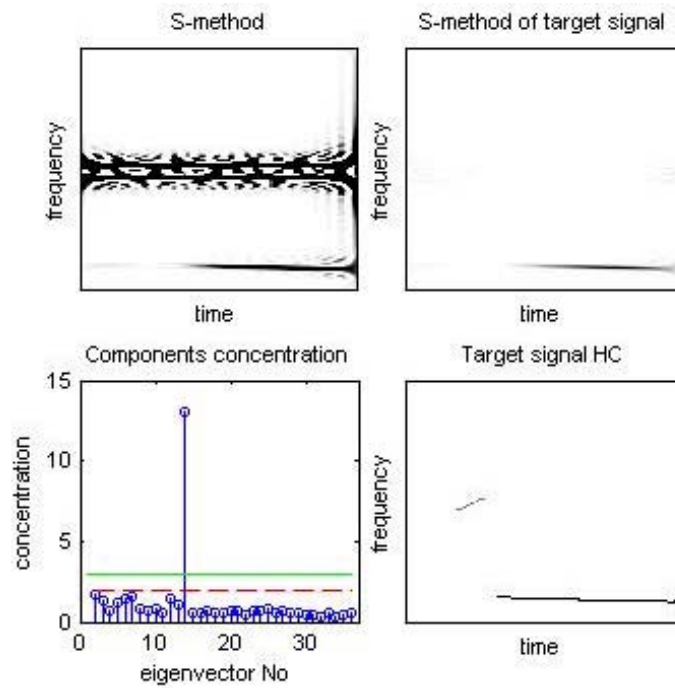


Figure 173: Signal 61 - Concentration of the eigenvectors time-frequency representations (bottom left), Time-frequency representation of the detected target signal (top right), Highly concentrated time-frequency representation of the detected target signal (bottom right)

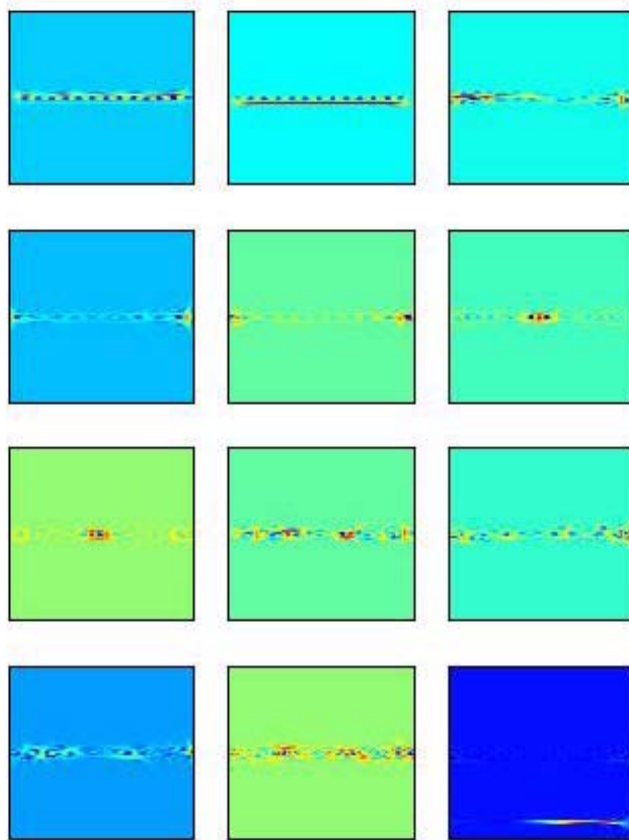


Figure 174: Signal 61 - The frequency representation of the eigenvectors used for the concentration calculation and target detection. In all subplots horizontal axis is for time and vertical axis is for frequency

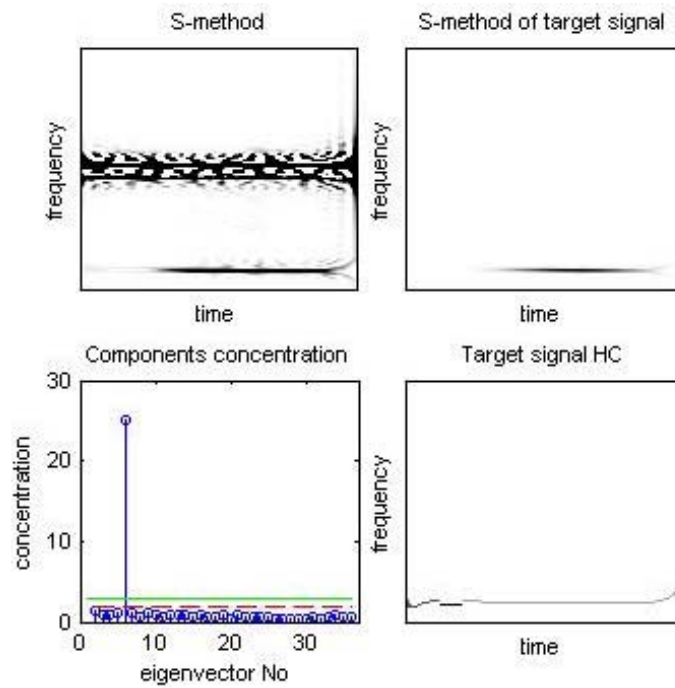


Figure 175: Signal 62 - Concentration of the eigenvectors time-frequency representations (bottom left), Time-frequency representation of the detected target signal (top right), Highly concentrated time-frequency representation of the detected target signal (bottom right)

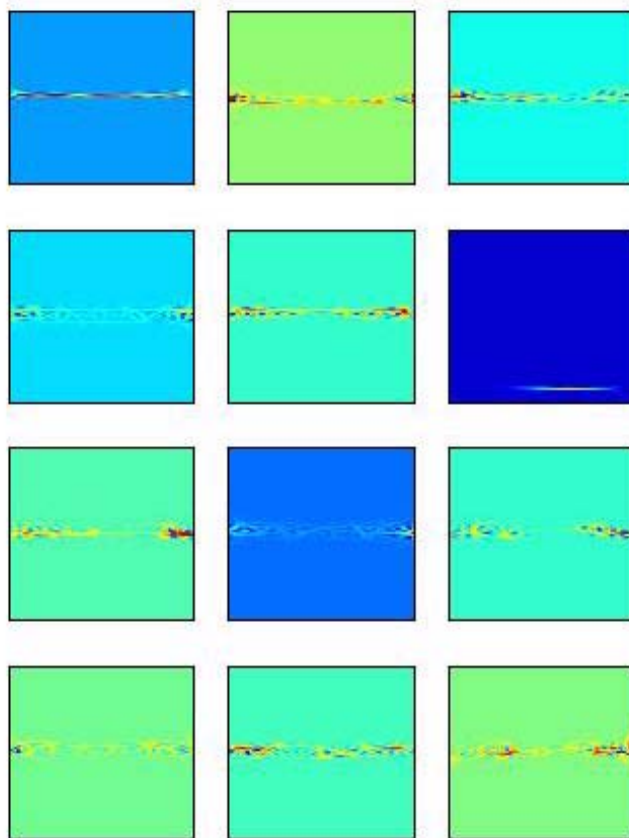


Figure 176: Signal 62 - The frequency representation of the eigenvectors used for the concentration calculation and target detection. In all subplots horizontal axis is for time and vertical axis is for frequency

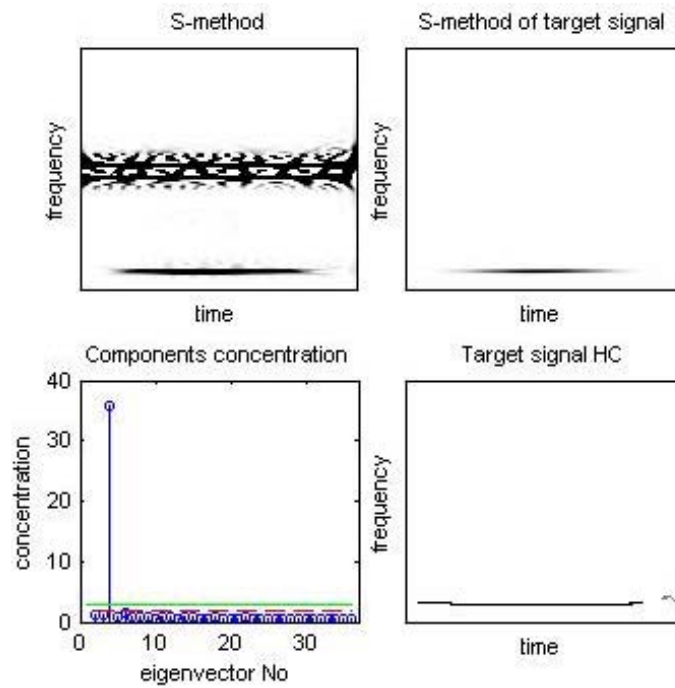


Figure 177: Signal 63 - Concentration of the eigenvectors time-frequency representations (bottom left), Time-frequency representation of the detected target signal (top right), Highly concentrated time-frequency representation of the detected target signal (bottom right)

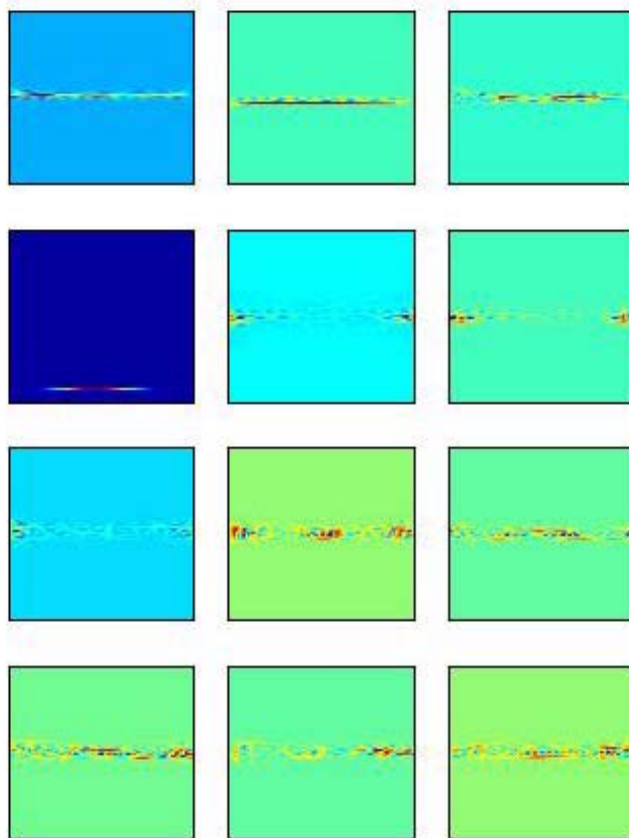


Figure 178: Signal 63 - The frequency representation of the eigenvectors used for the concentration calculation and target detection. In all subplots horizontal axis is for time and vertical axis is for frequency

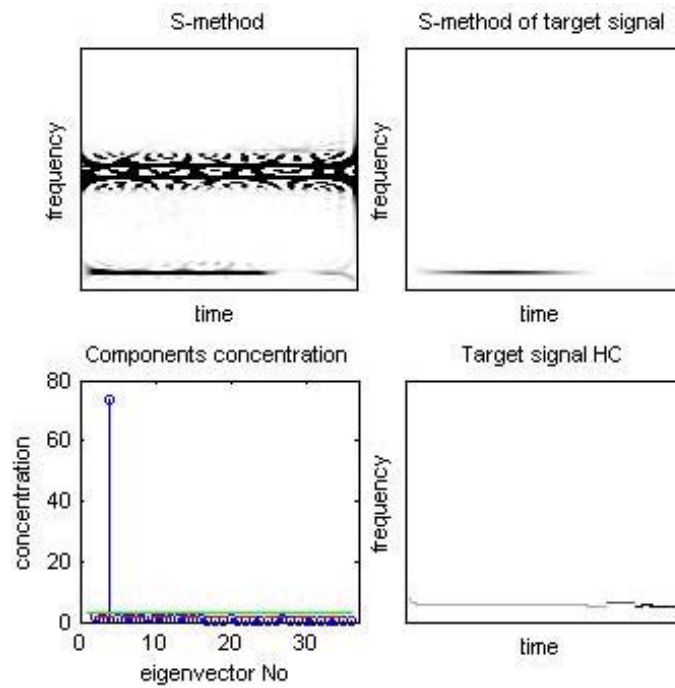


Figure 179: Signal 64 - Concentration of the eigenvectors time-frequency representations (bottom left), Time-frequency representation of the detected target signal (top right), Highly concentrated time-frequency representation of the detected target signal (bottom right)

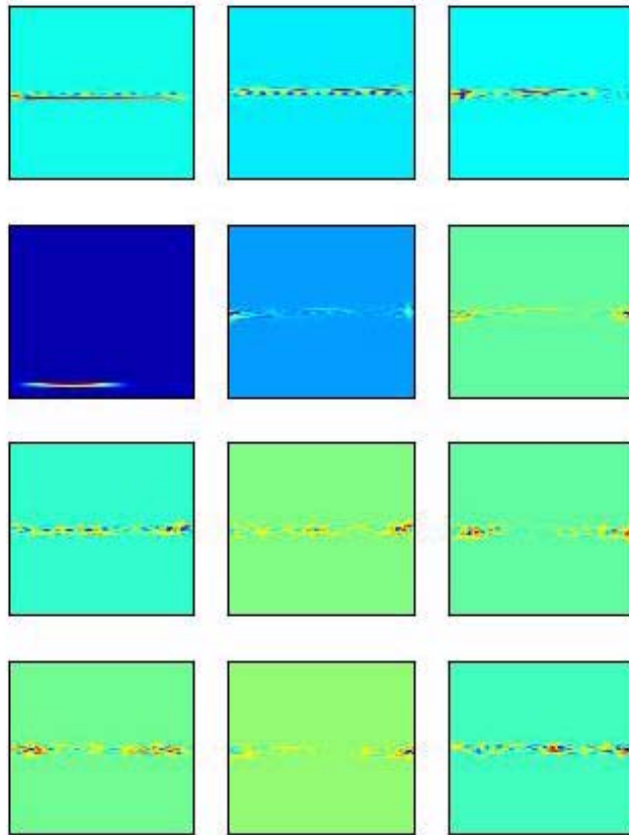


Figure 180: Signal 64 - The frequency representation of the eigenvectors used for the concentration calculation and target detection. In all subplots horizontal axis is for time and vertical axis is for frequency

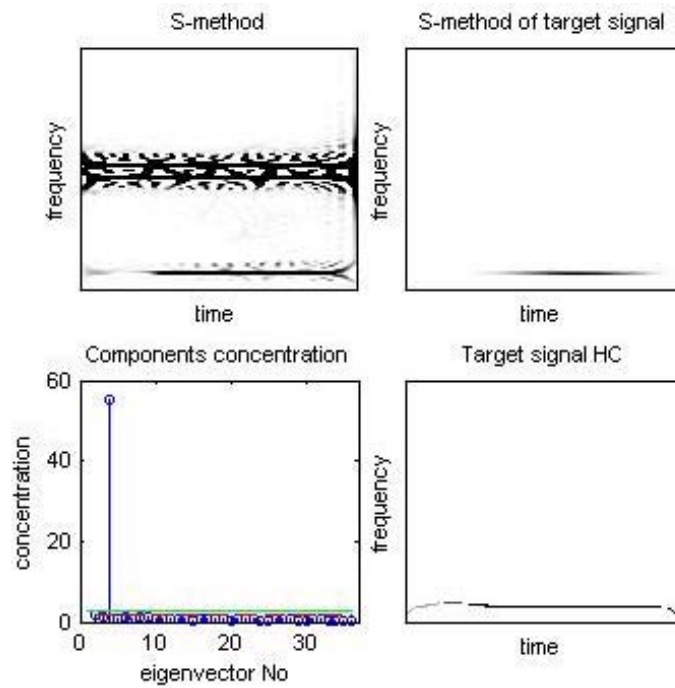


Figure 181: Signal 65 - Concentration of the eigenvectors time-frequency representations (bottom left), Time-frequency representation of the detected target signal (top right), Highly concentrated time-frequency representation of the detected target signal (bottom right)

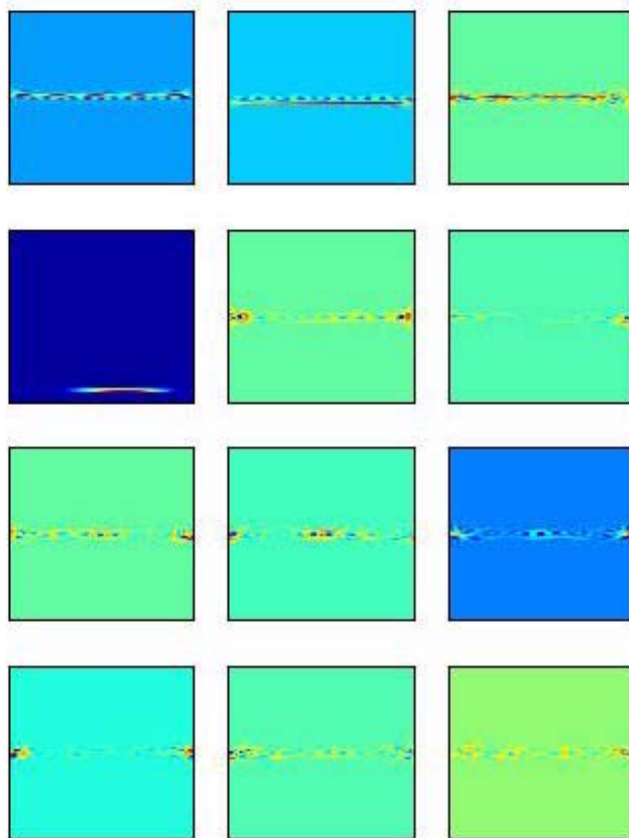


Figure 182: Signal 66 - The frequency representation of the eigenvectors used for the concentration calculation and target detection. In all subplots horizontal axis is for time and vertical axis is for frequency

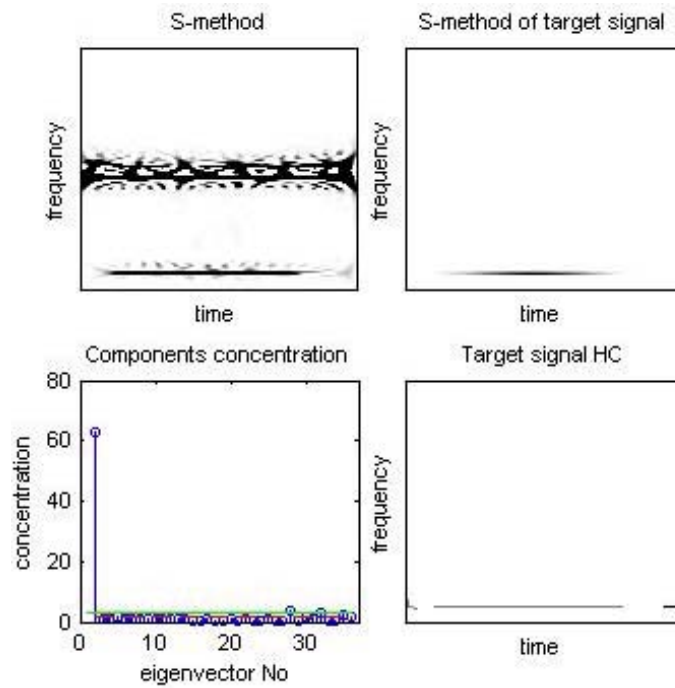


Figure 183: Signal 66 - Concentration of the eigenvectors time-frequency representations (bottom left), Time-frequency representation of the detected target signal (top right), Highly concentrated time-frequency representation of the detected target signal (bottom right)

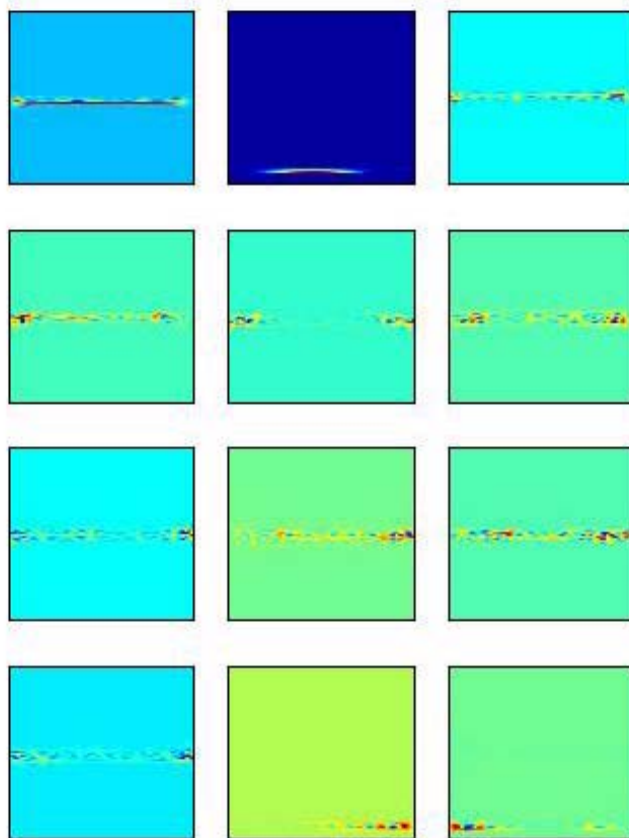


Figure 184: Signal 67 - The frequency representation of the eigenvectors used for the concentration calculation and target detection. In all subplots horizontal axis is for time and vertical axis is for frequency

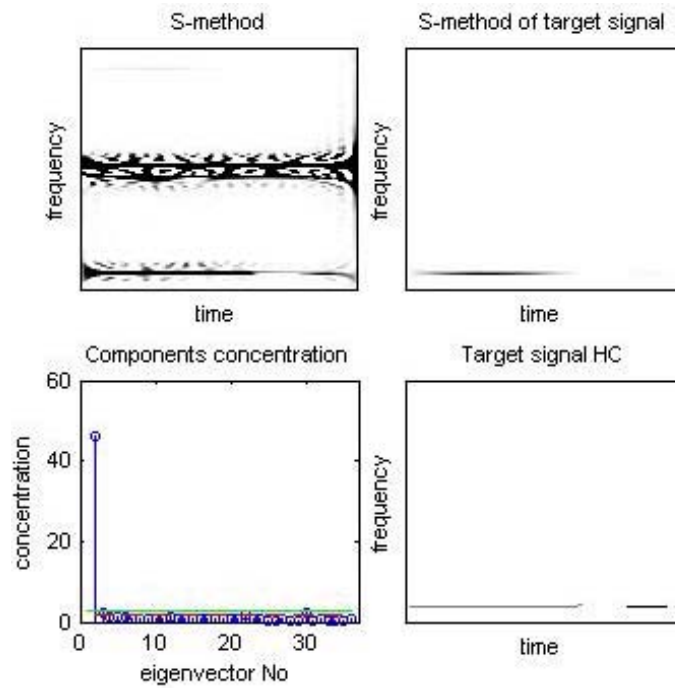


Figure 185: Signal 67 - Concentration of the eigenvectors time-frequency representations (bottom left), Time-frequency representation of the detected target signal (top right), Highly concentrated time-frequency representation of the detected target signal (bottom right)

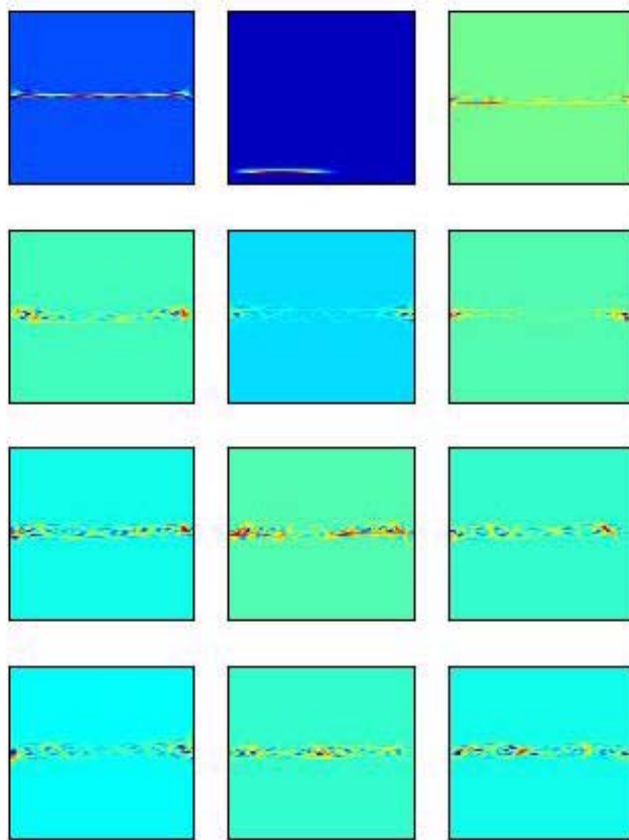


Figure 186: Signal 67 - The frequency representation of the eigenvectors used for the concentration calculation and target detection. In all subplots horizontal axis is for time and vertical axis is for frequency

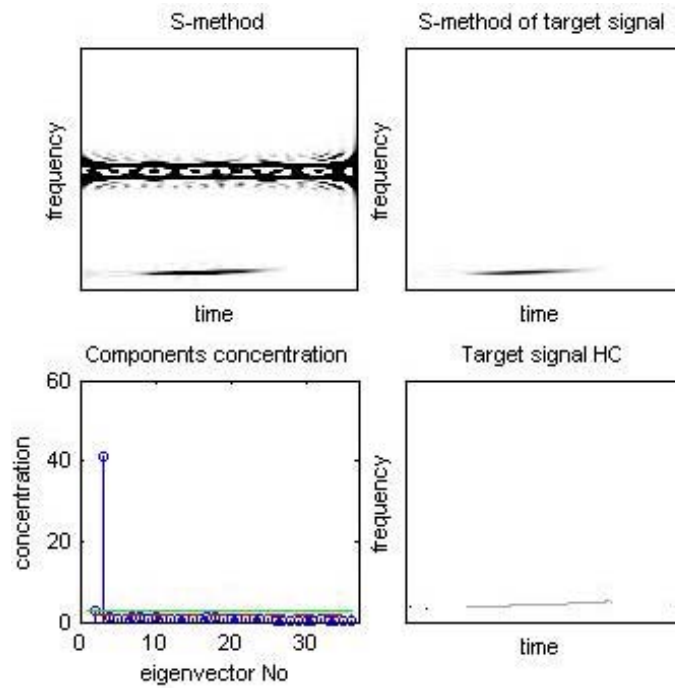


Figure 187: Signal 68 - Concentration of the eigenvectors time-frequency representations (bottom left), Time-frequency representation of the detected target signal (top right), Highly concentrated time-frequency representation of the detected target signal (bottom right)

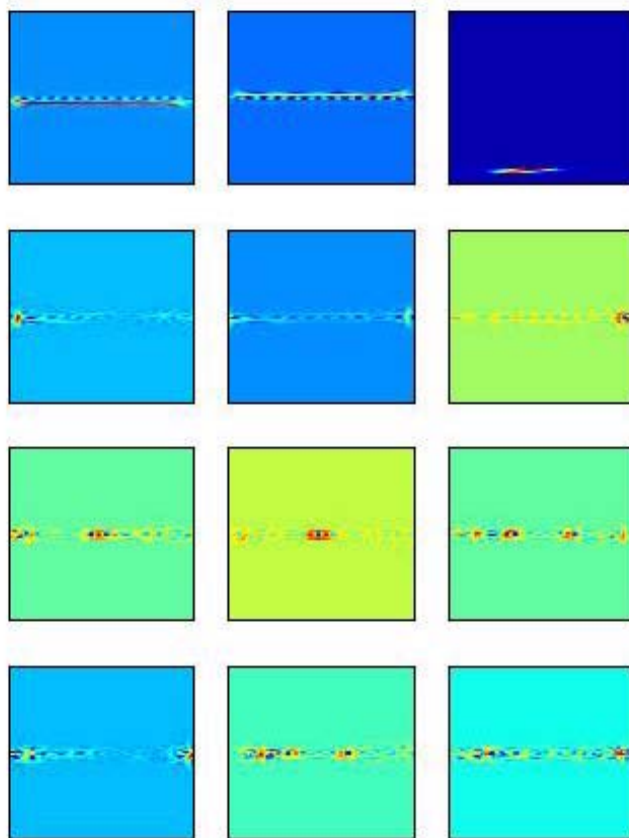


Figure 188: Signal 68 - The frequency representation of the eigenvectors used for the concentration calculation and target detection. In all subplots horizontal axis is for time and vertical axis is for frequency

UNCLASSIFIED

SECURITY CLASSIFICATION OF FORM
(highest classification of Title, Abstract, Keywords)

DOCUMENT CONTROL DATA

(Security classification of title, body of abstract and indexing annotation must be entered when the overall document is classified)

1. ORIGINATOR (the name and address of the organization preparing the document. Organizations for whom the document was prepared, e.g. Establishment sponsoring a contractor's report, or tasking agency, are entered in section 8.) Defence R&D Canada – Ottawa Ottawa, Ontario, Canada K1A 0Z4		2. SECURITY CLASSIFICATION (overall security classification of the document, including special warning terms if applicable) UNCLASSIFIED	
3. TITLE (the complete document title as indicated on the title page. Its classification should be indicated by the appropriate abbreviation (S,C or U) in parentheses after the title.) A novel approach for the detection of maneuvering air targets in sea-clutter using High-Frequency Surface-Wave radar (U)			
4. AUTHORS (Last name, first name, middle initial) Thayaparan, Thayananthan; Stankovic, Ljubisa; Dakovic, Milos			
5. DATE OF PUBLICATION (month and year of publication of document) December 2005		6a. NO. OF PAGES (total containing information. Include Annexes, Appendices, etc.) 214	
		6b. NO. OF REFS (total cited in document) 26	
7. DESCRIPTIVE NOTES (the category of the document, e.g. technical report, technical note or memorandum. If appropriate, enter the type of report, e.g. interim, progress, summary, annual or final. Give the inclusive dates when a specific reporting period is covered.) DRDC Ottawa Technical Report			
8. SPONSORING ACTIVITY (the name of the department project office or laboratory sponsoring the research and development. Include the address.) Defence R&D Canada – Ottawa Ottawa, Ontario, Canada K1A 0Z4			
9a. PROJECT OR GRANT NO. (if appropriate, the applicable research and development project or grant number under which the document was written. Please specify whether project or grant) 15aq10		9b. CONTRACT NO. (if appropriate, the applicable number under which the document was written)	
10a. ORIGINATOR'S DOCUMENT NUMBER (the official document number by which the document is identified by the originating activity. This number must be unique to this document.) DRDC Ottawa TR 2005-251		10b. OTHER DOCUMENT NOS. (Any other numbers which may be assigned this document either by the originator or by the sponsor)	
11. DOCUMENT AVAILABILITY (any limitations on further dissemination of the document, other than those imposed by security classification) <input checked="" type="checkbox"/> (X) Unlimited distribution <input type="checkbox"/> () Distribution limited to defence departments and defence contractors; further distribution only as approved <input type="checkbox"/> () Distribution limited to defence departments and Canadian defence contractors; further distribution only as approved <input type="checkbox"/> () Distribution limited to government departments and agencies; further distribution only as approved <input type="checkbox"/> () Distribution limited to defence departments; further distribution only as approved <input type="checkbox"/> () Other (please specify):			
12. DOCUMENT ANNOUNCEMENT (any limitation to the bibliographic announcement of this document. This will normally correspond to the Document Availability (11). However, where further distribution (beyond the audience specified in 11) is possible, a wider announcement audience may be selected.) Unlimited			

UNCLASSIFIED

SECURITY CLASSIFICATION OF FORM

DCD03 2/06/87

13. ABSTRACT (a brief and factual summary of the document. It may also appear elsewhere in the body of the document itself. It is highly desirable that the abstract of classified documents be unclassified. Each paragraph of the abstract shall begin with an indication of the security classification of the information in the paragraph (unless the document itself is unclassified) represented as (S), (C), or (U). It is not necessary to include here abstracts in both official languages unless the text is bilingual).

(U) A novel time-frequency signal decomposition approach is evaluated for the detection of maneuvering air targets in sea-clutter using High-Frequency Surface-Wave Radar (HFSWR). This approach is based upon time-frequency analysis and its eigenvalue decomposition. Results demonstrate that the new approach provides an effective way for detecting and analyzing maneuvering air targets in heavily cluttered regions. In addition, the proposed approach successfully detects the maneuvering target in all cases of the experiment. In contrast, the traditional Fourier transform method fails to detect air targets when a certain degree of acceleration is present. This is because of the phenomenon known as Doppler smearing. It is statistically shown that the new approach produces satisfactory results even with very low signal-to-noise ratios. The results obtained are robust with respect to the algorithm parameters. The basis of the method, theoretical derivations, and comparisons with traditional procedures are outlined here-in.

14. KEYWORDS, DESCRIPTORS or IDENTIFIERS (technically meaningful terms or short phrases that characterize a document and could be helpful in cataloguing the document. They should be selected so that no security classification is required. Identifiers such as equipment model designation, trade name, military project code name, geographic location may also be included. If possible keywords should be selected from a published thesaurus. e.g. Thesaurus of Engineering and Scientific Terms (TEST) and that thesaurus-identified. If it is not possible to select indexing terms which are Unclassified, the classification of each should be indicated as with the title.)

Sea-Clutter
High-Frequency Surface-Wave Radar
Time-Frequency Analysis
Wigner Distribution
Short Time Fourier Transform
S-method
Fourier Transform
Doppler Processing
Signal Decomposition

Defence R&D Canada

Canada's leader in Defence
and National Security
Science and Technology

R & D pour la défense Canada

Chef de file au Canada en matière
de science et de technologie pour
la défense et la sécurité nationale



www.drdc-rddc.gc.ca